A Heavy Flavor Tracker for STAR

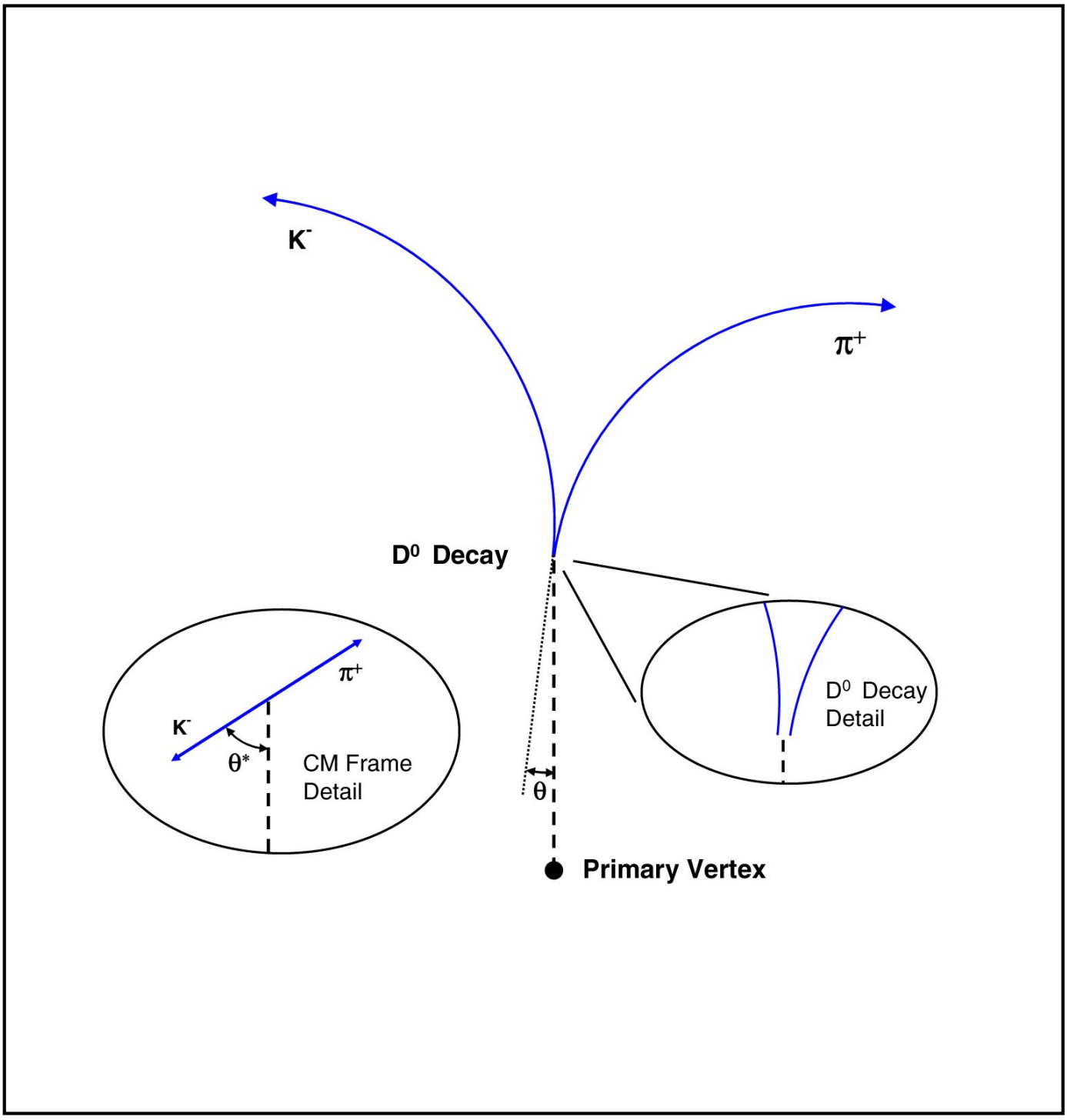

hft_cd_v5_a

This page intentionally left blank

A Heavy Flavor Tracker for STAR

C.Chasman, D.Beavis, R.Debbe, J.H.Lee, F.Videbaek, Z. Xu

Brookhaven National Laboratory, Upton, NY 11973

S. Kleinfelder, S. Li

University of California, Irvine, CA 92697

R. Cendejas, H. Huang, S. Sakai, C. Whitten

University of California, Los Angeles, CA 90095

M. Bystersky, J. Kapitan, V. Kushpil, M. Sumbera

Nuclear Physics Institute AS CR, 250 68 Rez/Prague, Czech Republic

C. Colledani, W. Dulinski, A. Himmi, C. Hu, A. Shabetai, M. Szelezniak, I. Valin, M. Winter

Centre National de la Recherche Scientifique, Strasbourg, France

J. Kelsey, M. Miller, R. Milner, M. Plesko, R. Redwine, F. Simon, B. Surrow, G. Van Nieuwenhuizen

Massachusetts Institute of Technology, Cambridge, MA 02139

X. Dong, L. Greiner, H.S. Matis, H.G. Ritter, A. Rose, E. Sichtermann, X. Sun, J.H. Thomas, V. Tram, H.H. Wieman, N. Xu

Lawrence Berkeley National Laboratory, Berkeley, CA 94720

H. Bichsel

University of Washington, Seattle, WA 98195

This page intentionally left blank

Contents

List of Figures

List of Tables

1 Executive Summary

We propose to construct a Heavy Flavor Tracker (HFT) for the STAR experiment at RHIC. The HFT will greatly extend the physics capabilities of STAR by enabling the topological identification of D-mesons through the measurement of displaced vertices with a precision of about 50 μm in p+p collisions as well as in Au+Au collisions.

The HFT consists of 4 layers of silicon detectors grouped into two sub-systems with different technologies, guaranteeing increasing resolution when tracking from the TPC and the Silicon Strip Detector (SSD) towards the vertex. The Intermediate Silicon Tracker (IST) consisting of two layers of single-sided strips is located inside the SSD. The IST is followed by two layers of Silicon Pixel Detector (PIXEL). The pixel detectors have the resolution necessary for a precision measurement of the displaced vertex.

The PIXEL will use CMOS Active Pixel Sensors (APS), an innovative new technology never used before in a collider experiment. The characterstic that the APS sensors are only 50 μm thick opens up a new realm of possibilities for physics measurements. In particular, a thin detector (0.28% radiation length per layer) in STAR makes it possible to do the direct topological reconstruction of open charm hadrons down to very low p_T by the identification of the charged daughters of the hadronic decay.

1.1 Scientific Motivation

The primary motivation for the HFT is to extend STAR's capability to measure heavy flavor production by the measurement of displaced vertices and to do the direct topological identification of open charm hadrons. These are key measurements for the heavy ion and spin physics programs at RHIC. Heavy quark measurements will facilitate the heavy ion program as it moves from the discovery phase to the systematic study of the dense medium created in heavy ion collisions as well as the detailed measurement of the nucleon spin structure in polarized p + p collisions. The primary physics topics to be addressed by the HFT include heavy flavor energy loss, flow, and a test of partonic thermalization at RHIC.

A precise measurement of the spectra of D meson states will shed light on several open questions in heavy ion collisions. From the spectra and the production ratios of D states, we will be able to extrapolate to the total yield for charm quark production. Furthermore, the open charm production rate is high enough at RHIC that the coalescence process becomes relevant for Charmonium production. Knowledge of the total production cross section for charm quarks is also essential as a baseline for J/ψ measurements. A meaningful answer to the question of whether the J/ψ mesons are suppressed or enhanced at RHIC requires knowledge of the charm production in heavy ion reactions.

The heavy quark can also be used to probe the properties of the medium created in heavy ion collisions. The production of gluons is kinematically suppressed for heavy flavors. As a consequence, heavy flavors should lose less energy in the dense medium.

An important measurement to be made with the HFT is R_{AA}; the ratio of charmed meson production in Au-Au collisions to the binary-scaled production rate in p-p or d-Au collisions. (See section 2.5.1). Current measurements using non-photonic electrons as a measure of the abundance of charm and beauty hadrons, indicate that the rate of energy loss for heavy quarks is unexpectedly high and inconsistent with our current understanding in pQCD models. Based on the non-photonic electron data presented at Quark Matter, the whole theory of heavy quark energy loss is uncertain and may be completely wrong; especially in regards to beauty.

Another important measurement to be made with the HFT is a measurement of the elliptic flow of D mesons down to very low p_T values. (See section 2.4.1). It is generally accepted that elliptic flow is established in the partonic phase. If charm quarks, with a mass much larger than the temperature of the system, undergo elliptic flow then it has to arise from many collisions with the abundant light quarks. Thus, flow of charm quarks can be taken as a probe for frequent re-scatterings of light quarks and is an indication of thermalization that may be reached in the early stages of heavy ion collisions at RHIC. We believe that proof of thermalization constitutes the last step towards the establishment of the QGP at RHIC and this measurement requires a very thin detector to push the measurement down to the lowest momenta where transverse elliptic flow is manifest.

1.2 PIXEL Detector Concept

Both, the IST and the SSD use conventional strip technology. The pixel detector brings extremely high precision tracking capabilities to STAR with a resolution of 10 μm at the first layer of the detector, over a large pseudo-rapidity range, and with complete azimuthal angular coverage. This will enable STAR to perform high precision measurements of heavy-quark production over the broadest range of phase space, colliding system sizes and energies. It will exploit all of STAR's unique features including particle ID and tracking from the lowest to the highest p_T. In these respects, the HFT provides physics measurements that are unique at RHIC.

The PIXEL will surround the interaction vertex. It has two tracking layers composed of monolithic CMOS pixel detectors using 30 μm × 30 μm square pixels. These critical innermost tracking layers lie at radii of 2.5 cm and 5.0 cm, respectively, and these layers are active over 20 cm in z and have ~ 110 million pixels. The silicon chips for the detector will be thinned to 50 μm and will be mounted on low mass carbon fiber structures to minimize pointing errors generated by multiple Coulomb scattering.

Such a thin detector requires a correspondingly thin beam pipe. Therefore, we propose to build a new, 0.5 mm thick beam-pipe for the STAR detector. The construction of such a thin beam-pipe is challenging and it requires a unique design to enable the beampipe to be handled during installation and bakeout.

2 The Physics of the HFT

2.1 Introduction

An important goal of high-energy nuclear physics is to understand Quantum Chromodynamics (QCD) at extreme temperatures and energy densities. Under these extraordinary conditions, we believe that the fundamental symmetries of QCD will reveal themselves: quarks and gluons will be the relevant degrees of freedom, color will be deconfined and chiral symmetry will be restored. Calculations within the framework of regularized lattice QCD predicts a fast crossover from ordinary nuclear matter into a deconfined and locally thermalized state of quarks and gluons called the Quark-Gluon Plasma[1] (QGP).

High-energy nuclear collisions can be characterized by three distinct phases: the initial phase where hard interactions between the partons of the incoming nuclei dominate, an intermediate phase where re-interactions between the constituents in the matter result in collectivity, and a final stage where hadronization, and chemical and thermal freeze-out occur. The matter produced in high-energy nuclear collisions can be investigated by studying the dynamics of the collective expansion of the bulk of the produced particles and by studying the interaction of the medium with penetrating probes such as leading particles and jets. In particular, the measurement of large elliptic flow,[2] and the observation of strong modifications of high p_T particle production. as measured by the ratio $R_{AA,}$[3] and the disappearance of the away side jet[4] have provided evidence for a high density and strongly interacting state of matter at RHIC.[5] The goal of our research program is to elucidate the nature of this matter and to determine if it is dominated by hadronic or partonic degrees of freedom.

Rare processes provide new ways to probe the medium generated in high-energy nuclear collisions. Bjorken[6] proposed that hard scattered partons (quarks and gluons) drawn from the incoming nuclei will interact with the medium in a density-dependent way. Bjorken's initial energy loss mechanism (elastic scattering) did not provide effects large enough to be observed but medium-induced radiation (gluonic bremsstrahlung) can generate significant energy loss effects.[7,8] For example, hard parton scatterings can be experimentally reconstructed in elementary particle collisions ($e^+ + e^-, \bar{p} + p$) because the outgoing parton fragments into a collimated spray of energetic hadrons at large transverse angles with respect to the beam.

The cluster of hadrons, from the parton fragmentation, is known as a jet. Jets can also be identified in high energy nuclear collisions on a statistical basis; the modification of their properties may signal novel flavor dependent energy loss mechanisms in a dense medium by the parton that initiated the jet. Full jet reconstruction in heavy ion collisions is

exceedingly difficult but leading hadrons (i.e. high p_T hadrons, which typically carry a large fraction of the jet energy) and their correlations with other hadrons may provide the essential signals of partonic interactions in the medium.

Collective flow measurements have played a prominent role in understanding the physics of nuclear collisions because the magnitude and pattern of the collective motion is closely related to the equation of state (EOS) of the produced matter.

If local equilibrium is achieved, we will be able to use hydrodynamic models to study the EOS and understand the degrees of freedom relevant for the basic constituents of the matter. Heavy quark (*c, b*) production provides some of the most important observables. Due to their large masses, *c* and *b* quarks are produced dominantly by the interactions of the initial incoming partons whereas lighter quarks are produced throughout the later stages of the evolution of a heavy ion collision. Thus, the total yields of *c* and *b* quark production provide a direct connection to the initial state.

Due to their heavy mass and presumably small hadronic cross sections, charmed quarks are a sensitive probe for the frequency of interaction and therefore the degree of thermalization with constituents before hadronization. At high p_T, heavy quarks may be less suppressed than light quarks due to the "dead cone" effect and so high p_T probes are an additional way to study partonic energy loss. If charmed quarks participate sufficiently in re-scattering processes, they will develop flow (i.e. transverse radial and elliptic flow), which can be observed in charmed hadron momentum distributions. Finally, charmed quarks might achieve thermal equilibrium with the surrounding medium leading to statistical hadronization. In this case, the relative abundances of charmed hadrons are significantly modified.

The study of the structure of nuclei and nucleon is an important frontier in strong interaction physics. Despite considerable experimental and theoretical progress over the past several decades, many open questions remain. Striking examples include the observations by the European Muon Collaboration that partons in nuclei have different momentum distributions than partons in nucleons even when probed at high energy,[9] and that the contribution from quark spins to the proton spin is remarkably small.[10,11] The cross sections for heavy flavor production at RHIC receive large contributions from gluon-gluon scattering. The HFT will allow direct measurement of the total cross sections and their spin and nuclear dependence.

2.2 Initial Heavy Quark Production

Quarks are elementary particles and, depending on the energy scale, there are two mechanisms that generate their masses with different degrees of importance: current quark masses are generated by the electroweak symmetry breaking mechanism (Higgs

mass) and spontaneous chiral symmetry breaking leads to the constituent quark masses in QCD (QCD mass). The QCD interaction strongly affects the light quarks (u, d, s) while the heavy quark masses (c, b, t) are mainly determined by the Higgs mechanism, as shown in Figure 1. In high-energy nuclear collisions at RHIC, heavy quarks are produced through gluon fusion and $q\bar{q}$ annihilation.[12]

Heavy quark production is also sensitive to the parton distribution function. Unlike the light quarks, heavy quark masses are not modified by the surrounding QCD medium[13] (or the excitations of the QCD medium) and the value of their masses is much higher than the initial excitation of the system. It is these differences between light and heavy quarks in a medium that make heavy quarks an ideal probe to study the properties of the hot-dense medium created in high-energy nuclear collisions.

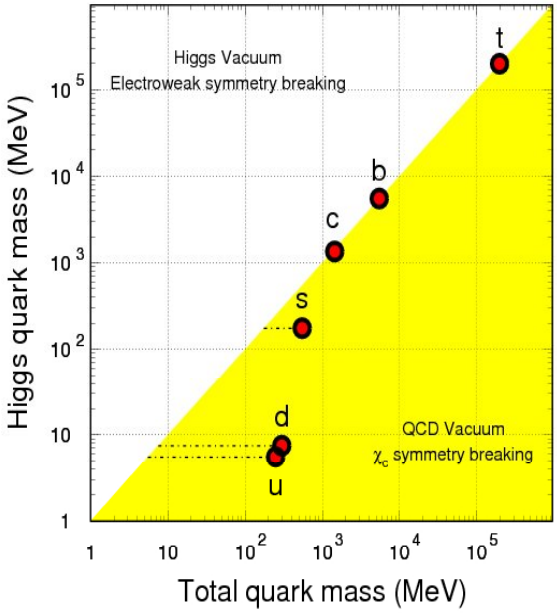

Figure 1: Masses of the six quark flavors. The current and additional QCD masses are shown by blue- and yellow-boxes, respectively. The figure is adapted from Ref. [13].

Understanding the yield of charmed hadrons in hadron-hadron collisions requires a knowledge of the projectile and target parton distribution functions, the cross section for parton-parton interactions which generate charm quarks and the fragmentation functions for $c(b)$ quarks into charmed (bottom) hadrons. The parton distributions within the proton can be extracted from electron-proton collisions while the cross-sections for gluon fusion and $q\bar{q}$ annihilation are calculated in a perturbative QCD framework up to next-to leading-order (NLO).[14] However, the parton and gluon distribution functions within the nucleus, relevant to the charm and bottom quark production at RHIC energies, are poorly understood[15] and thus leave room for precise measurements of charm cross sections in

p + p, d + Au and Au + Au collisions. Perturbative QCD predictions for the cross section $\sigma(c\bar{c})$ and $\sigma(b\bar{b})$ in p + p collisions at $\sqrt{s_{NN}}$ = 200 GeV may be found in the literature[14] and they are in reasonably good agreement with the cross-sections measured at RHIC given that some of the theoretical calculations are uncertain by as much as 50%.

Experiment: $\sigma_{NN}(c\bar{c})$ = 900 - 1400 μb Theory : $\sigma_{NN}(c\bar{c})$ = 289 - 445 μb 20 - 30 $c\bar{c}$ pairs per central Au + Au collision at $\sqrt{s_{NN}}$ = 200 GeV
Theory : $\sigma_{NN}(b\bar{b})$ = 1.64 - 2.16 μb 0.04 - 0.06 $b\bar{b}$ pairs per central Au + Au collision at $\sqrt{s_{NN}}$ = 200 GeV

Table 1: Cross section for the production of charm and beauty.

The uncertainty in the theoretical cross-sections arises from a reasonable variation of quark masses (m_c = 1.2-1.8 GeV, m_b = 4.5-5.0 GeV), factorization and renormalization scales (μ_R and μ_F), and parton distribution functions (MRST, CTEQ, GRV). The number of underlying binary nucleon-nucleon collisions normalizes the cross section values. There are approximately 1000 binary nucleon-nucleon scatterings in each central Au + Au collision.

In heavy ion collisions, final state interactions may also enhance charm production relative to the binary scaling of initial parton collisions and may also lead to additional production of charm via "thermal" processes. An analogous mechanism dominates strangeness production. The heavy quark channels should be greatly suppressed by the thermal factor due to the heavy quark mass ($m_c \approx$ 1.2 to 1.8 GeV, $m_b \approx$ 4.5 to 5.0 GeV),[16] making heavy quark production rates primarily sensitive to the dynamics of the initial collisions. This is especially true for the b quark. Figure 2 shows the calculated contributions to the total charm production at $y = 0$ for $\sqrt{s_{NN}}$ = 200 GeV, with an energy density of 3.2 GeV/fm^3 at the moment of thermal equilibration.

STAR and PHENIX have made measurements of charm production in Au+Au, d+Au, and p+p collisions at RHIC. The PHENIX data for Au + Au collisions suggests that the cross-section for open charm production is consistent with the expectations of pQCD. These results were derived from non-photonic single electron spectra[17] as shown in Figure 3. The STAR results show that the cross-section for open charm production in d+Au and Au+Au is consistent with binary collision scaling but the total yield may be larger than NLO pQCD models. Note, since we only measure the electrons and D^0s to extract the total charm cross-section, several assumptions such as the ratios of the neutral over charged D-mesons have to be used. Both the p_T integrated yield of dN/dy and the value of $\langle p_T \rangle$ of the measured D-meson spectrum are larger than the pQCD model

predictions. The STAR results are obtained from a direct reconstruction of the open charm hadrons[18] as well as through single electron spectra.

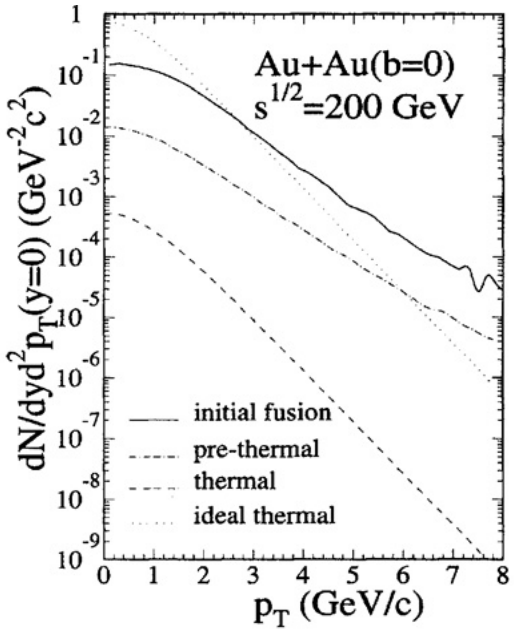

Figure 2: Contributions to charm production at RHIC energies include the initial gluon fusion and $q\bar{q}$ annihilation phase (solid line), a pre-thermal phase characterized by scattering between free-streaming partons, and a thermal phase that assumes parton equilibration. The distributions were calculated with an energy density of 3.2 GeV/fm^3 at the moment of thermal equilibration. As a reference, the faint dotted line is the thermal production of charm due to an initial fully equilibrated QGP. The figure is from Ref. [16].

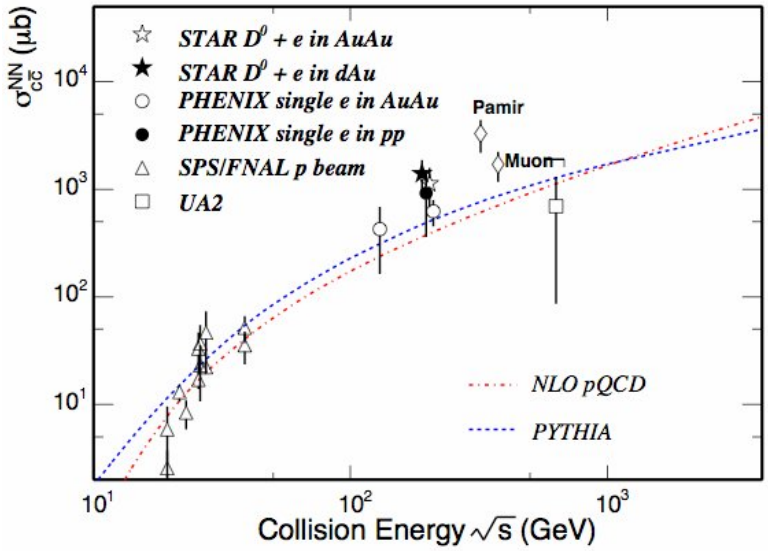

Figure 3: Total cc̄ production cross-sections per nucleon-nucleon collision vs. collision energy. The dashed line depicts a PYTHIA calculation.[19] The dot-dashed line depicts a NLO pQCD calculation with MRST HO, m_c = 1.2 GeV/c^2, $\mu_F = 2m_c$, $\mu_R = 2m_c$.[20] The figure is adapted from Ref. [18, 20].

2.3 The Need for Direct Topological Reconstruction of Open Charm

When direct measurements of heavy flavor hadrons are not possible, non-photonic electrons from heavy flavor decays can be used to study charm production. However, there are serious limitations in such measurements. As shown by Batsouli, Kelly, Gyulassy, and Nagle in Ref. [21], the decayed electron distributions are insensitive to the intrinsic shape of the D-meson transverse momentum distribution. Due to the decay kinematics and the light mass of the electrons and positrons, the dynamical information in the primary spectrum is washed out. This phenomenon is shown in Figure 4. There is a clear difference between the zero mean free path hydrodynamic flow prediction (solid) and the infinite mean free path pQCD Pythia calculations (dashed-line) for D-mesons; but the resulting electron spectra are nearly indistinguishable. In order to extract useful information about heavy flavor production in heavy ion collisions, we have to measure the charm and beauty-hadrons by direct topological reconstruction. Single electron spectra are not sufficient.

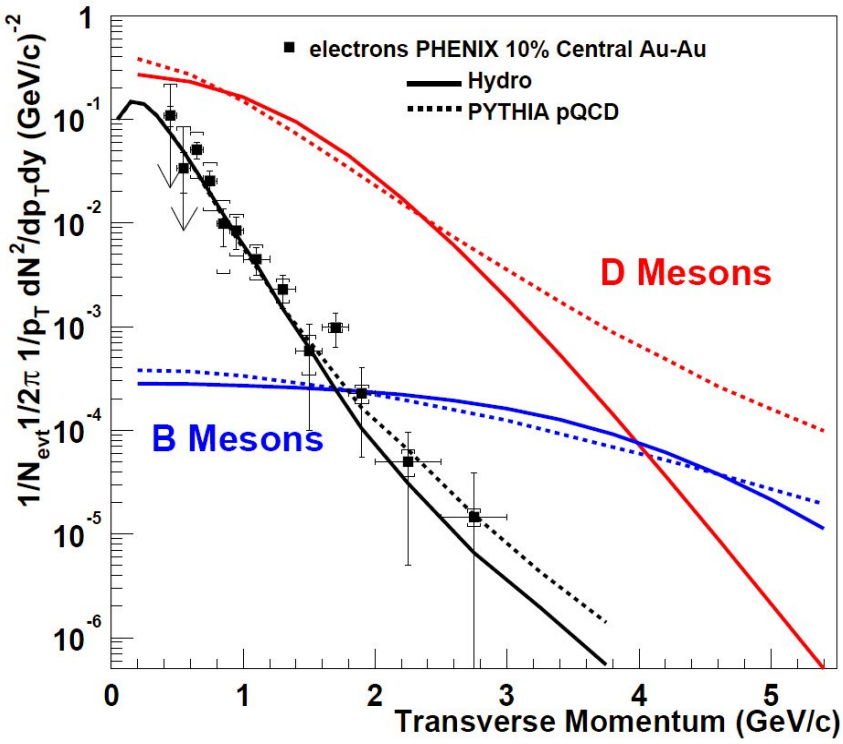

Figure 4: Solid- and dashed-curves represent the charm- (red) and beauty-hadron (blue) spectra from Blast-Wave and Pythia model calculations, respectively. The corresponding heavy flavor decayed electron spectra are shown as black curves. The data are the single electron distributions measured in 10% central Au + Au collisions at 130 GeV by the PHENIX collaboration. The figure is adapted from Ref. [21].

The same conclusion is reached when doing the analysis of R_{AA} for heavy flavor spectra. Recall that R_{AA} is the ratio scaled by the number of binary collisions of the charm yield measured in heavy ion collisions relative to the yield in p-p or d-Au. The nuclear

modification factor, $R_{AA,}$ for D-mesons is shown in Figure 5. Two different models are presented. The figure shows that there are large differences in the two D-meson R_{AA} ratio curves but the corresponding decayed-electron R_{AA} curves are essentially identical for all p_T. These are theoretical curves without error bars. This suggests that it will not be possible to determine the heavy flavor R_{AA} from the decay electron R_{AA}. In addition,, any electron measurement will have large systematic uncertainties at low momentum due to the large background from photonic electron production.[17,18] At higher p_T, electrons from B-meson decays will become more abundant making the electron measurement for charm physics even less realistic. This clearly calls for a direct measurement of heavy flavor hadrons, i.e. D- and B-mesons.

The proposed Heavy Flavor Tracker (HFT) will make these and other measurements by the direct topological reconstruction of the various charmed hadrons, including the D^+, D^-, D^0, D_s^+ and possibly Λ_c^+. Thus the HFT will enable us to dramatically reduce the systematic uncertainties that are inherent in single electron spectra.

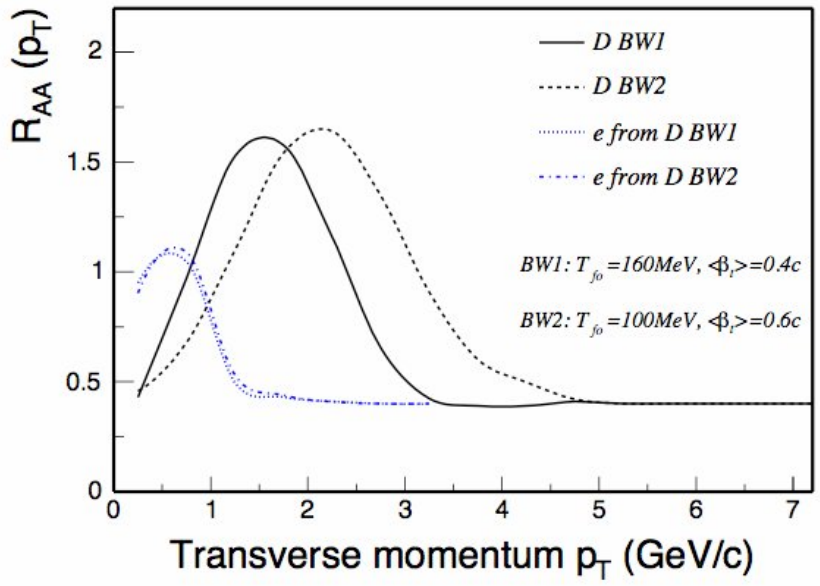

Figure 5: Nuclear modification factor R_{AA} of D-mesons assuming a hydro-dynamically inspired parameterization with a collective flow velocity of $<\beta_r>$ = 0.4*c* and 0.6c for D-mesons. The corresponding electron decay-spectra are shown by the blue dashed (1) and (2) lines.[22]

2.4 Probing Medium Thermalization: Charm Quark Re-interactions

RHIC data on light flavor hadrons strongly suggests that partonic collectivity has been achieved in heavy ion collisions. The successful measurement of partonic collectivity is a necessary step toward the discovery of a QGP. However, this is not sufficient until we also address the issue of thermalization.

Collectivity in heavy ion reactions is addressed by studying flow. Many important measurements of transverse radial and elliptic flow of identified hadrons, containing light quark flavors (q = u, d, s), have been performed at RHIC. The main conclusions from these studies are that the systems created in ultra-relativistic Au + Au collisions exhibit strong collective expansion. Compared to measurements at lower SPS energies, the degree of collectivity is stronger. In addition, measurements of the spectra of multi-strange hadrons (Ξ and Ω) at RHIC suggest that they freeze-out at a higher temperature and lower collective velocity than the lighter hadrons. However, a significant amount of elliptic flow is also observed for multi-strange baryons. The elliptic flow of the multi-strange baryons is comparable to the amount of flow observed for the non-strange baryons and is in good accord with the valence quark scaling hypothesis that describes the non-strange quark bearing mesons and baryons well.[23] These results have been interpreted as an indication that sizeable partonic collectivity develops at RHIC. Details of these studies can be found in the literature.[2,24,25,26,27]

The key question, then, is whether or not charm quarks flow. If the elliptic flow of charm were comparable to the elliptic flow of the lighter quarks, then this would be a clear indication of a thermalized state of matter at RHIC because it takes many interactions with lighter quarks, and gluons, to cause a heavy quark to acquire the collective motion of the bulk matter.

Theoretical calculations indicate that thermalization may be reached at RHIC at temperatures $T_{eq} \approx 0.3\text{-}0.5$ GeV[28] and that the duration of the equilibrium period is on the order of 5-10 fm/c.[29,30] Thermal production of $c\bar{c}$ pairs is suppressed due to their large masses ($m_{c\bar{c}} = 2.2 - 2.3$ GeV/c^2), however, charmed hadrons may still be produced in a thermalized fashion if the c and $\bar{c}$ quarks become embedded in a thermalized bath of light quarks. The relative probability of creating different charmed hadrons will be driven by the properties of the medium which is providing the additional quarks necessary to form the hadrons. The relative yield of various charmed hadrons is thus sensitive to the properties (temperature and chemical potentials) of the light quark medium and these hadron yields must be measured in order to achieve a full understanding of the medium.

The transverse momentum distributions of these hadrons are particularly important. The p_T distributions reflect the dynamical evolution of the system and yield indirect information about different stages of the collision. After hadronization is complete and inelastic collisions cease, the particle abundances are fixed. This is commonly referred to as chemical freeze-out. Later when elastic interactions cease, the particle momentum spectra become fixed; this is referred to as kinetic freeze-out. The evolution of the system is recorded in the p_T spectra because, for most particle species, transverse *radial* flow is accumulated throughout the whole collision history while transverse *elliptic* flow is believed to saturate at early times in the collision sequence.

Thus charmed hadron flow is an indicator of thermalization due to the heavy quark interactions with light quarks and gluons. If thermalization takes place, it is reached during the partonic stage of the collision. In order to test the question of thermalization experimentally, we propose to measure the charmed hadron transverse radial and elliptic flow. The combination of the open charm spectra and v_2 will allow us to determine the collective properties of the charm quarks and the probable degree of thermalization of the light quarks.

2.4.1 Elliptic Flow

In non-central heavy ion collisions, the overlap of the colliding nuclei is spatially deformed and has an ellipsoidal shape. Through many re-scatterings, the pressure gradients will be built up in non-head on high energy collisions. In this way the initial state spatial anisotropy can be transformed into a final state momentum space anisotropy. Notice that re-scattering is a sufficient condition for the development of these anisotropies and thermalization is not required. Theoretically, the largest momentum anisotropies are obtained in the hydrodynamic limit[31] where there is a zero mean free path. This leads to instantaneous local thermal equilibrium.

Momentum space anisotropies lead to an azimuthal variation of the transverse-momentum distribution relative to the reaction plane. The anisotropy can be quantified by the coefficients of a Fourier decomposition of the distribution in azimuth. The largest contribution comes from the second Fourier coefficient $v_2(p_T, y)$, the *elliptic flow coefficient*. In the evolution of elliptic flow, the strong and early spatial deformation decreases because the matter begins to expand more rapidly in the direction of the shorter axis of the ellipsoid.[32] As the spatial deformation disappears, the build-up of flow due to pressure gradients ceases. Elliptic flow is thought to be a signal that develops in the early stages of a collision. RHIC data[2,33,34] show that in semi-central Au + Au collisions, elliptic flow reaches the hydrodynamic limit for transverse momenta up to 2 GeV/c and this suggests early thermalization[31] at a time of $\tau = 0.6$ fm/c. Thus, information about the equation of state[35] can be determined from a measurement of elliptic flow. If all hadron species experience the same anisotropic flow, their v_2 coefficients should obey simple hydrodynamic relations[35] and exhibit a characteristic mass dependence. As an example, Figure 6 (top) shows the measured elliptic flow of strange hadrons up to, and including, the multiply strange Ξ baryon. At low momentum, all particles exhibit a linear rise in v_2 and a clear mass ordering appears from the lower mass kaon to the heavier Ξ. The bottom plot in Figure 6 shows the measured elliptic flow versus transverse momentum, where both axes are scaled with the number of valence quarks. Quark coalescence models predict a universal scaling of v_2/n versus p_T/n at intermediate momentum where quark recombination is (supposedly) the dominant hadron production mechanism. In these models, collectivity – the elliptic flow of constituent quarks – is intrinsically built in

and supports the idea of partonic collectivity. These analyses demonstrate that collectivity is established at the partonic level.

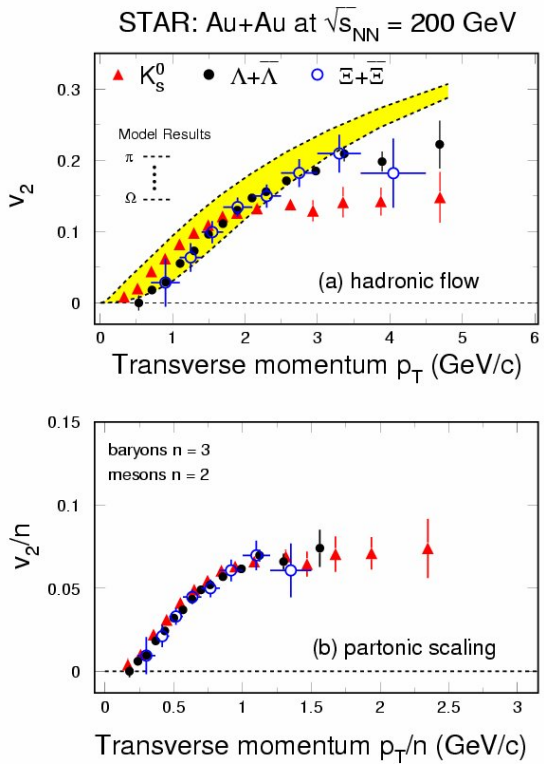

Figure 6: Elliptic flow of strange hadrons at RHIC as measured by the STAR detector. The top panel demonstrates typical hydro-dynamical mass ordering up to a momentum p_T < 2GeV/c and saturation at larger momentum. The bottom panel shows the scaling of elliptic flow with the number n of valence quarks in the saturation region (baryons, n=3; mesons, n= 2).

At RHIC energies, charm quarks are abundantly produced. Due to their high mass and small interaction cross section, the strength of elliptic flow of heavy flavor hadrons may be a good indicator of thermalization occurring at the partonic level. If all quarks in heavy flavor hadrons flow with the same pattern as the quarks in the light flavor hadrons, this indicates frequent interactions between all quarks. Hence, thermalization of light quarks is likely to have been reached through partonic re-scattering.

Figure 7 shows a first indication of charm particle elliptic flow at RHIC measured in the inclusive electron channel.[36] The predictions assume elliptic flow for the light quarks as determined by fits to experimental data. Presently, the data support the idea that the heavy charm quarks flow. As shown in the figure, the uncertainties are rather large especially at low transverse momentum where hydrodynamic behavior should occur. A precise measurement of directly reconstructed open charm hadrons to low momentum is essential to confirm and further quantify elliptic flow of the charm quarks.

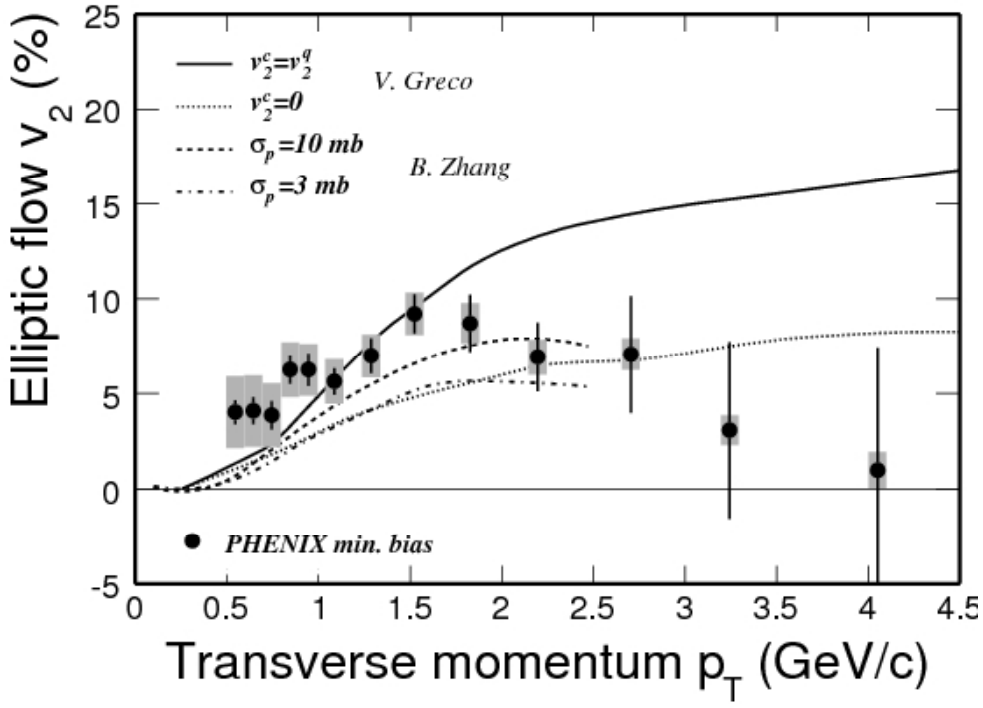

Figure 7: Non-photonic electron elliptic flow at RHIC. Open and closed symbols are data of non-photonic electron v_2 from PHENIX[36] Statistical errors are shown as solid lines and the open boxes indicate the size of the systematic errors. The solid-line represents the results from Greco[37] et al. where, in this coalescence calculation, similar v_2 distributions for c- and u-quarks are assumed.

2.4.2 Charm Hadro-Chemistry

Hadronic yields and their ratios have been measured from AGS to RHIC energies and have been successfully described by statistical models.[38,39] The relevant parameters are the chemical freeze-out temperature T_{ch}, and the chemical potentials μ_i for conserved quantum numbers, i.e. net strangeness, charge, and baryon number conservation.[40] The extracted chemical freeze-out temperature T_{ch} is higher than the kinetic freeze-out temperature T_{fo} extracted from momentum spectra.[41] Chemical freeze-out occurs before kinetic freeze-out.

Charm quarks are dominantly produced in initial parton-parton scatterings[20] and the thermal production of charm quarks is suppressed due to their large mass. In the case of sufficient re-scatterings, initially produced charm quarks might thermally (but not chemically) equilibrate with the surrounding medium. This means their momentum distribution can be described by a temperature parameter consistent with the spectra of light quarks, while the total abundance of charm quarks is determined by the initial parton collision dynamics.

Some models predict statistical hadronization of charm quarks.[42,43] Statistical coalescence scenarios predict large changes in open (regarding relative abundances, e.g.

the D^0 / D_s^+ ratio) and hidden charm production with a strong centrality dependence.[44] Statistical coalescence implies that charm quarks travel over significant distances, e.g. in a QGP. Therefore, a consistent description of precision data by these models would be an indication of deconfinement.[44]

Measuring the total charm and bottom yields requires measuring the yields of several different hadrons. Indeed, charm quarks may fragment into a variety of hadrons as shown in the first column of Table 2. These fragmentation ratios have recently been compiled[45,46] using *e-p* and e^+-e^- collision data. The ratios are found to be independent of the collision energy and the collision system (e-p or e^+-e^-). They are likely to be the same in p-p collisions at mid-rapidity where the HFT can be used to detect charmed particles at RHIC. Note that the ratios calculated using PYTHIA,[47] shown in the third column of Table 2, differ significantly from the measured ratios. To avoid any uncertainties in the charge yield measurement, these ratios will have to be measured in $p + p$ collisions at RHIC energies.

	e-p and e^+-e^- average	Pythia	Statistical coalescence
$f(c \rightarrow D^+)$	0.232	0.162	0.21
$f(c \rightarrow D^0)$	0.549	0.639	0.483
$f(c \rightarrow D_s^+)$	0.101	0.125	0.182
$f(c \rightarrow \Lambda_c^+)$	0.076	0.066	0.080
$f(c \rightarrow J/\psi)$		0.006	0.057

Table 2: Charm quark fragmentation functions. The left column is from Ref. [45,46]. The right column is from Ref. [44]. The D^+ and D^0 yields include feed-down from D^{*+} and D^{*0} decays.

The effect of statistical coalescence is shown in the last column of Table 2 (see Ref. 44). The calculation assumes that charm quarks statistically coalesce with the lighter quarks, (i.e. according to the temperature and chemical potential of the light-quark system). The temperature and chemical potential are set so that the light hadron yields measured at RHIC are reproduced. In addition, the number of charm quarks present in the system is set by pQCD calculations and this is reflected by a charm-chemical potential in the statistical coalescence model. The results of the model show that statistical coalescence increases the yield of the D_s^+ meson by 80% and the J/ψ yield by a factor of 10 compared to PYTHIA while the yield of D^0 and D^+ decrease slightly. Thus, the ratios D_s^+/ D^0, D_s^+/D^+ and J/ψ / D^0 are very sensitive probes of thermal charm hadron production.

Experimentally, we will be able to precisely measure the ratio of D_s^+ to D^+ yields because most of the systematic errors in the individual spectra cancel out when they are reconstructed in very similar decay channels: $D^+ \rightarrow K^- \pi^+ \pi^+$ and $D_s^+ \rightarrow K^- \pi^+ K^+$.

A precise measurement of the total charm production (mostly carried by open charm mesons) will also serve as a baseline for J/ψ enhancement/suppression measurements, which have been suggested as a possible signature for QGP formation.[48]

2.5 Probing the Density of the Medium: Heavy Quark Energy Loss

In order to develop collective flow in heavy ion collisions, there must be frequent interactions between the constituents of the medium. These interactions will cause energy loss for the energetic partons that are traversing the medium. The amount of energy loss will depend on the distance traveled in the medium.

Results on the nuclear modification factor R_{AA} indicate that the rate of energy loss for heavy-quarks in central Au + Au collisions is surprisingly similar to that for the light-quarks (u, d, s).[49] This experimental observation contradicts our early understanding of the pQCD interactions of energetic partons in a hot and dense medium where much less energy loss was expected for heavy-quarks compared to the light ones.[50,51,52] Since there have been no directly reconstructed heavy-quark hadron distributions from RHIC experiments so far, non-photonic electrons in the transverse momentum range $4 < p_T < 10$ GeV/c were used for these heavy-quark studies. The analysis of non-photonic electron p_T distributions is complicated by an unknown mixture of charm and beauty contributions. A possible way to disentangle these effects is a direct topological reconstruction of charmed-hadron distributions and a measurement of charmed hadron angular correlations.

2.5.1 R_{AA} and Energy Loss

The discovery of a factor of 5 suppression of high p_T hadrons ($5 < p_T < 10$ GeV/c) produced in Au + Au collisions at RHIC and the disappearance of the away-side jet has been interpreted as evidence for jet quenching.[3,53,54,55] This effect was predicted to occur due to radiative energy loss of high energy partons that propagated through a dense and strongly interacting medium[56]. The energy loss of heavy quarks is predicted to be significantly less compared to light quarks because of a suppression of gluon radiation at angles $\Theta < M_Q/E$; where M_Q is the heavy quark mass and E is the heavy quark energy.[57] This kinematic effect is known as the "dead cone" effect. The suppression of small angle radiation has the advantage that the heavy quark fragmentation function and the spectrum of light particles produced in association with the heavy quarks can be calculated perturbatively.

Figure 8 shows the result for the ratio of charm (H) to light (L) quark suppression from QCD calculations assuming a size of about 5 fm for the static medium traversed by the fast quark. For transverse momenta $p_T > 7.5$ GeV/c this ratio is predicted to be about 2.0 due to the smaller energy loss of the heavy quark. In the case where heavy quarks suffer

the same amount of energy loss as light quarks, this ratio would be 1.0. This ratio is exponentially sensitive to the density of color charges in the medium, and so the measurement of nuclear modification factors of open charm mesons at large p_T is a promising tool for the study and further characterization of QCD matter at RHIC.

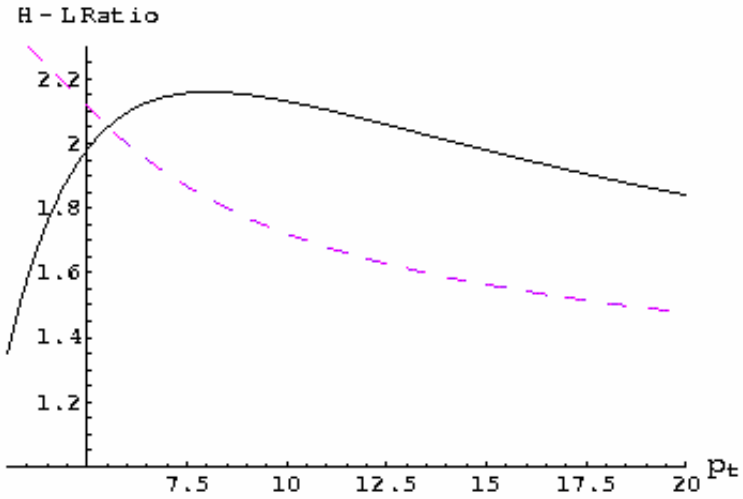

Figure 8: The ratio of suppression factors in hot matter for charm (H) and light (L) quarks. The solid line represents results from calculations with unrestricted gluon radiation, while the dashed line is based on calculations with a cut on gluon energies ω > 0.5 GeV. The size of the static medium traversed by the fast quark is assumed to be 5 fm. The figure is from Ref. [51].

Figure 9 shows the R_{AA} for non-photonic electrons[58,59,60] from STAR and PHENIX. The data extend up to $p_T \sim 10$ GeV/c. The suppression factor for single electron spectra is in the range of 0.2-0.3 which is almost exactly the same as the suppression factor observed for charged hadrons and pions[61,62] (i.e. light quarks). Using an unrealistically large initial gluon density of $dN_g/dy = 3500$, Djordjevic, Gyulassy, Vogt, and Wicks have done a pQCD calculation.[63] including gluon radiative energy-loss, which can barely reproduce the electron R_{AA} (see the blue-line in Figure 9). The model ignores the contributions from beauty-hadrons, and when beauty is added to the model, the resulting prediction for R_{AA} cannot describe the data at all (see the yellow band in Figure 9). The model with beauty over-predicts the data by a factor of 2-3. Note that for light-quark hadrons, like pions, a gluon density of ~1000 has been used to reproduce the observed R_{AA}. These results raise a serious challenge to our understanding of both the mechanism for heavy-quark production and the mechanism for energy-loss in a hot and dense medium. In order to resolve these important issues, we have to do direct topological reconstruction of open charm. It is experimentally and theoretically too difficult to make definite conclusions from the single-electron measurements due to the complications from the mixing of the electrons from D-meson decay and electrons from bottom hadron decay as well as the smearing of the decay kinematics.

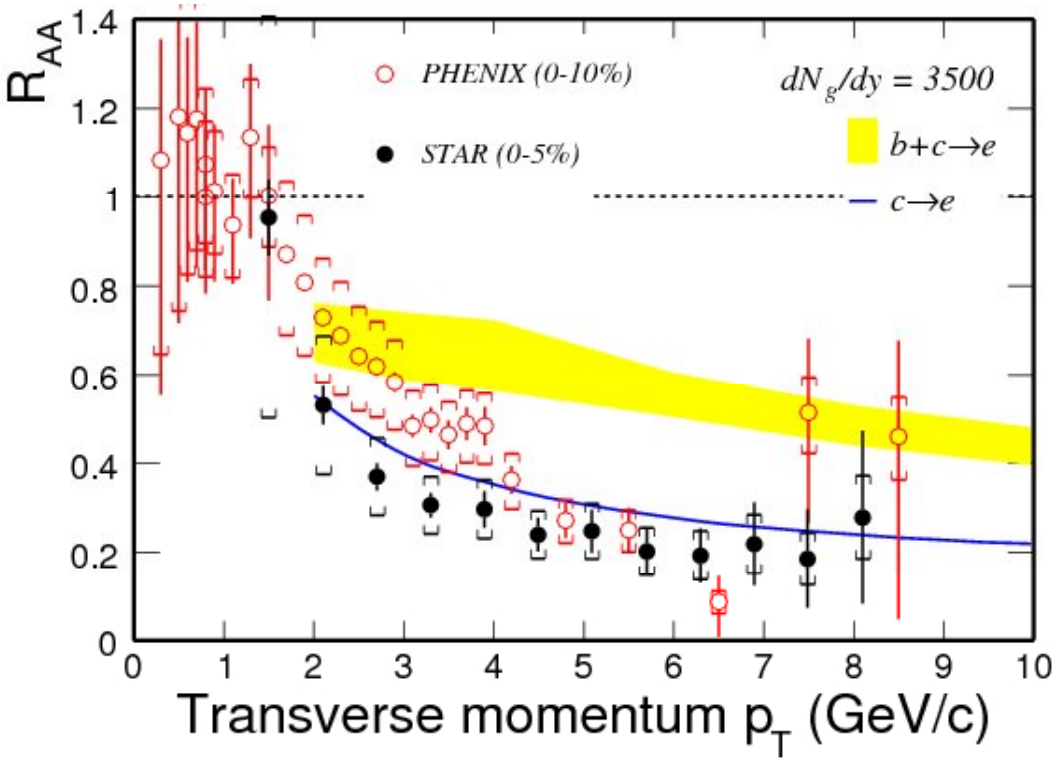

Figure 9: Non-photonic electron R_{AA} in central Au + Au collisions from STAR (open-symbols, top 5%) and PHENIX (filled-symbols, top 10%) from Refs. [58,59,60]. Theoretical predictions for charmed-hadron and charm and beauty-hadron decayed electrons are shown as blue- and yellow-bands, respectively. In these calculations, the initial gluon density was assumed to be unrealistically large: ~3500, see Ref [63] .

2.5.2 Charm Angular Correlations

Correlations between charmed hadrons are another way to separate charm and beauty physics at RHIC. Let the correlation between D mesons be defined as the normalized pair distribution $C(\Delta\phi) = N(p_1,p_2)/N_0$ where p_1 and p_2 are the momenta of the charmed hadrons, and N_0 is the total number of pairs.

Similar to jet production, heavy-quark production requires a large momentum transfer and so we expect a distinct back-to-back topology for the quarks (and mesons) as shown by the open-circles in Figure 10. In this calculation, the Pythia (v6.2) event generator was used with the default sets of parameters. As one can see in the figure, there is a clear back-to-back correlation for the D-mesons. We propose to utilize this distinct correlation to study the charm-quark energy loss in high-energy nuclear collisions.

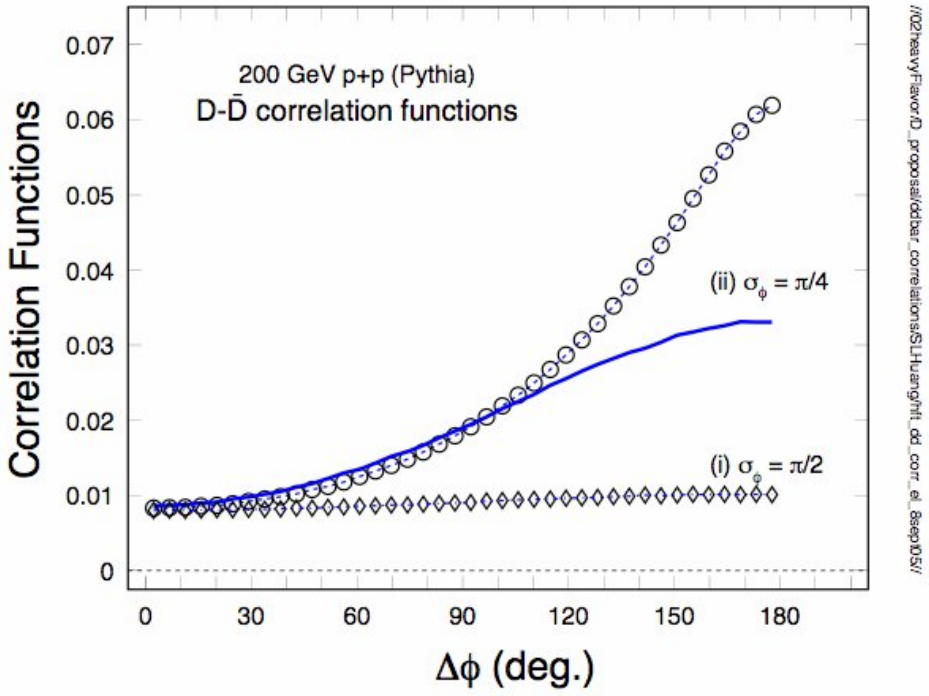

Figure 10: D-meson correlation functions for 200 GeV p + p collisions. Default parameters in the Pythia model were used in these calculations. A clear back-to-back correlation in the angular distribution of charmed mesons is observed (shown by the open circles). The Solid-line and the diamonds represent the results with angular smearing for $\sigma_\phi = \pi/4$ and $\pi/2$, respectively.

Now lets consider a few potential observables. For example, when a charm-quark interacts with the medium, it will lose energy and the original angular correlation pattern, as shown in the figure, will be modified. We have tried angular smearing of $\langle\sigma_\phi\rangle = \pi/4$ and $\pi/2$. In addition, the changes in the angular correlation depends on the nature of the interaction. Most of the (semi)elastic scatterings are directed in a narrow cone in the forward direction[64] while the inelastic scatterings, such as the gluon radiative energy loss[50] will lead to a much wider smearing in the final correlation. In the inelastic scattering scenario,[50,52] the energy-loss occurs deep inside the plasma and the final correlation function reflects the hot/dense properties of the medium. On the other hand, the resonant scattering happens near T_c.[64] Although both scenarios lead to sizable energy-loss, the angular correlations may allow us to distinguish these two different mechanisms in high-energy nuclear collisions. In order to perform the measurement, a large acceptance for the reconstructed charmed hadrons is required. The proposed HFT, plus STAR TPC and TOF, will be necessary for this study.

Recently, the measurements on charm production by the Belle Collaboration[65] show a surprisingly large cross-section for J/ψ production in $\sqrt{s}$ = 10.6 GeV $e^+ + e^-$ collisions. Even more surprising is the fact that more than half of the observed J/ψ's are accompanied by $c\bar{c}$ pairs. This result contradicts our current understanding for J/ψ

production in the pQCD framework, such as those discussed in Refs. [19,66,67,68], and implies a different production mechanism for heavy-quarks in elementary collisions.[69] As proposed in Ref. [69], gluon fragmentation is increasingly important for collisions at higher bombarding energies and so RHIC energies are very interesting. In elementary collisions, the main difference between the new and conventional processes lies in the angular correlation of the produced charmed hadrons. With the proposed HFT and STAR EMC (Electro-Magnetic Calorimeter), we will be able to study the correlation of D mesons to further understand pQCD in p + p collisions. We will also study the correlation of D mesons in high-energy nucleus-nucleus collisions, were the gluon density is high[70,71], and this might enhance the effects observed in elementary p + p collisions. These studies will certainly shed light on the production mechanisms for charm and charmonium at RHIC.

As mentioned earlier, heavy-quark production leads to a back to back correlation between particle and anti-particles. This correlation is also reflected in their decay products, such as the electron pairs. In this case, it causes the background in the intermediate mass region[72] $1 < m_{ee} < 3$ GeV/c^2 to have a correlation, too. (Here m_{ee} is the invariant mass of the electron pair.) This creates a significant background for a low mass vector meson analysis. Using the HFT to measure the correlated electron pairs will greatly reduce the background for vector meson and charm measurements via non-photonic electron spectra.

2.5.3 Baryon – Meson Ratios

In the intermediate p_T region $2 < p_T < 6$ GeV/c, light-quark baryon yields are known to be enhanced compared to meson yields in Au + Au collisions. The enhancement is found to be proportional to the collision centrality. These observations have been confirmed by both R_{AA} and v_2 measurements. The results are usually explained by a hadronization mechanism involving collective multi-parton coalescence rather than by independent vacuum fragmentation. The success of the coalescence approach implies deconfinement and possibly thermalization of the light quarks prior to hadronization. Since Λ_c is the lightest charmed-baryon and its mass is not far from the other D-mesons, it will be very interesting to measure the R_{AA} of Λ_c and compare it with the R_{AA} of the other charmed mesons in order to see if there is a meson-baryon difference. Theories about heavy quark deconfinement and collectivity can be tested with these comparisons. In addition, due to the different branching ratios for the semi-leptonic decays, the measurement of Λ_c spectra will help us understand the surprising suppression observed in the non-photonic electrons. In this case, even if charmed quark production scales with the number of binary collisions, an increase in the ratio Λ_c/D-mesons similar to that seen for the Λ/Kaon ratio will lead to a ~20% suppression in non-photonic electrons ($1 < p_T < 5$ GeV/c) for central Au + Au collisions.[73]

2.6 Probing the Symmetry of the Medium: Vector Mesons

Manifestations of chiral symmetry restoration in relativistic heavy ion collisions would provide clear evidence for fundamental modifications to the QCD vacuum. In this context, dilepton measurements of vector mesons have attracted great interest. Dileptons are not affected by final state interactions and are thus ideally suited to study the properties of the matter created in relativistic heavy ion collisions. The invariant mass region below 1 GeV is of particular interest, because possible modifications of the vector meson masses may be observable.

The measurement of chiral symmetry restoration has numerous and severe challenges. Not only are processes, which produce leptons rare, they are overwhelmed by leptonic decays of hadrons as well as by photonic decays followed by conversions. In addition the observed leptons are the integrated yield of radiation over the full evolution of the colliding system. Despite the experimental difficulties, the low and intermediate mass dileptons have been measured at the CERN-SPS and an excess of radiation above the hadron cocktail has been observed in the invariant mass region of $0.2 < M_{ee} < 0.6$ GeV/c^2 in semi-central Pb + Au collisions.[74,75] Also, the exciting results from RHIC runs indicate that jets have lost a large fraction of their energy in dense matter and the hadronic phase is relatively short. We believe that these observations at RHIC favor experimental measurements of photons and dileptons due to thermal radiation and will result in a clearer signature than from lower energy heavy ion collisions.

At STAR, clean electron identification is made possible by the combination of two techniques: a measurement of the energy lost by charged particles due to ionization in the TPC gas (dE/dx), and a measurement of charged particle velocity with the time-of-flight system. The observed electrons are, to a large extent, background. They originate from photons converting into electron-positron pairs $\gamma \rightarrow e^+ e^-$ in the detector material, from π and η Dalitz decays, and from semi-leptonic decay of heavy quark hadrons. The large acceptance of the STAR TPC makes it possible to reduce π^0 and η Dalitz decay background by a factor of 3 (single track) by measuring both electrons of the pair. The pixel detector of the HFT makes it possible to reject background of electrons and positrons from γ conversions outside the inner pixel detector b.y requiring hits in the pixel detector of the HFT. In addition, the HFT makes it possible to reject background from semi-leptonic decays of heavy quark hadrons. Correlated semi-leptonic decay of open charm forms the dominant source at intermediate mass.[76,77] This background originates from a secondary vertex that is displaced by ~ 100 μm that can be measured with the high resolution provided by the HFT.

Figure 11 shows the di-electron invariant mass distribution for various signals plus the background. The signals for vector mesons and thermal radiation are shown as the black curve[76] and have been calculated using the full acceptance of the STAR detector. The red

curve, at the top, is the total di-electron invariant mass yield using the STAR configuration in 2004. This is obtained from single inclusive electron spectrum measurements in 200 Au + Au collisions with the assumption of electron PID from Full TOF coverage. The gray curve is the e^+e^- pair invariant mass distribution for charm after a cut on the HFT DCA < 80 μm. The dot dashed line show the Dalitz decays from π^0 and η after rejection from the TPC. The standard method of dealing with the residual background is by a mixed-event method. This method has been used in CERES and NA52/NA60 at the SPS, and will be used in both PHENIX and STAR.

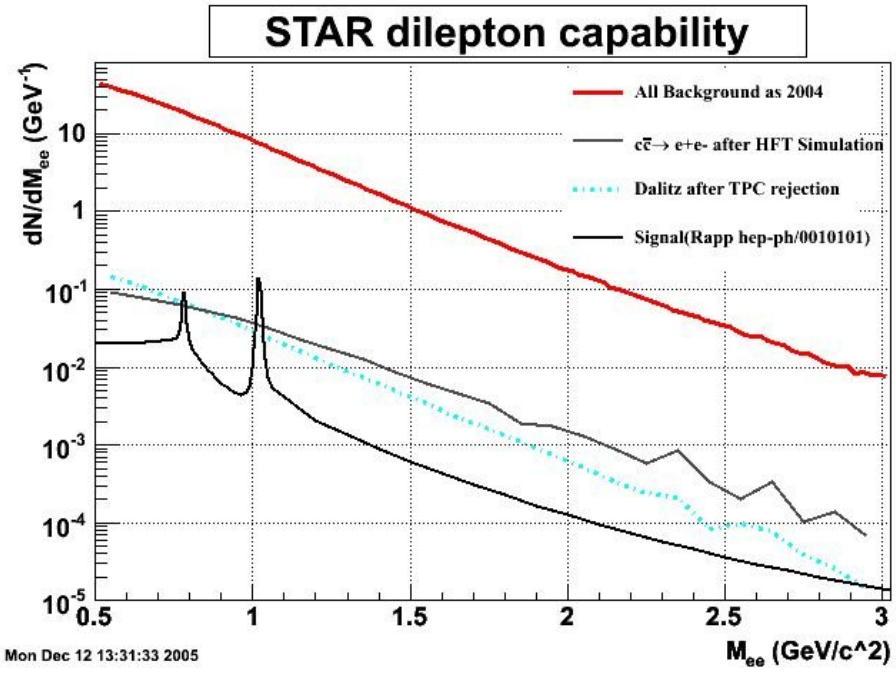

Figure 11: Di-electron invariant mass spectrum. The solid black curve is a prediction from R. Ralf Ref. [76] using the full STAR acceptance. The red curve at the top is the total di-electron invariant mass spectrum seen with the 2004 configuration of STAR but assuming electron PID from Full TOF coverage. The gray curve is the charm e^+e^- pair invariant mass distribution after a cut on the HFT DCA < 80 μm. The dot dashed line is the Dalitz decays from π^0 and η after rejection from TPC.

Our simulations show that we can extract a 3σ vector meson signal from the data with only 800 K events in the underlying spectrum. If we had to do this without the HFT, then the same 3σ signal would require 8 M events in the underlying spectrum. We estimate that we will be able to accumulate 22K ω-mesons in the pear and 6k ϕ-mesons in the peak in one RHIC year.

For these simulations we assumed a 50% efficiency for matching tracks between the TPC and the HFT, and we assumed a 50% efficiency for TOF + TPC tracking and PID. An

online trigger was not employed. The results are comparable to the NA60 In + In run data.

2.7 Probing Cold Nuclear Matter

The measurement of charm production in d+Au collisions yields essential baseline data for the Relativistic Heavy Ion Collision program at RHIC.

In relativistic heavy-ion collisions heavy flavor is expected to be produced via initial gluon fusion[78]. In the absence of nuclear effects the observations in relativistic heavy ion collisions would thus scale with the number of binary collisions. Deviations from this scaling result from the partonic structure in the nucleus and from the high energy density following the collision. Detailed measurements in p+p collisions establish the underlying cross sections and kinematic distributions for hadrons containing heavy flavor for the free nucleon. Collisions of d+Au nuclei allow the study of nuclear modification and intrinsic k_T distributions.

The comparison of d+Au and p+p cross sections for heavy flavor production is of interest by itself, in particular since the production is dominated by gluon-gluon scattering contributions. Partons in bound nucleons show noticeably different momentum distributions compared to those in free nucleons, and heavy flavor measurements separate gluon from quark distributions. Precise insight in the nuclear parton distributions should lead to deeper understanding of the mechanisms associated to nuclear binding and applications in neutrino experiments, in addition to the aforementioned heavy ion measurements.

Mid-rapidity STAR measurements of charm production are sensitive to the transition region between anti-shadowing and shadowing as illustrated in Figure 12, whereas measurements of bottom probe anti-shadowing. They are complementary to fixed target measurements and to future measurements at the LHC.

2.8 Probing the Nucleon

The measurement of charm and bottom production in p+p collisions yields essential baseline data for the Relativistic Heavy Ion Collision program at RHIC as outlined in the previous section.

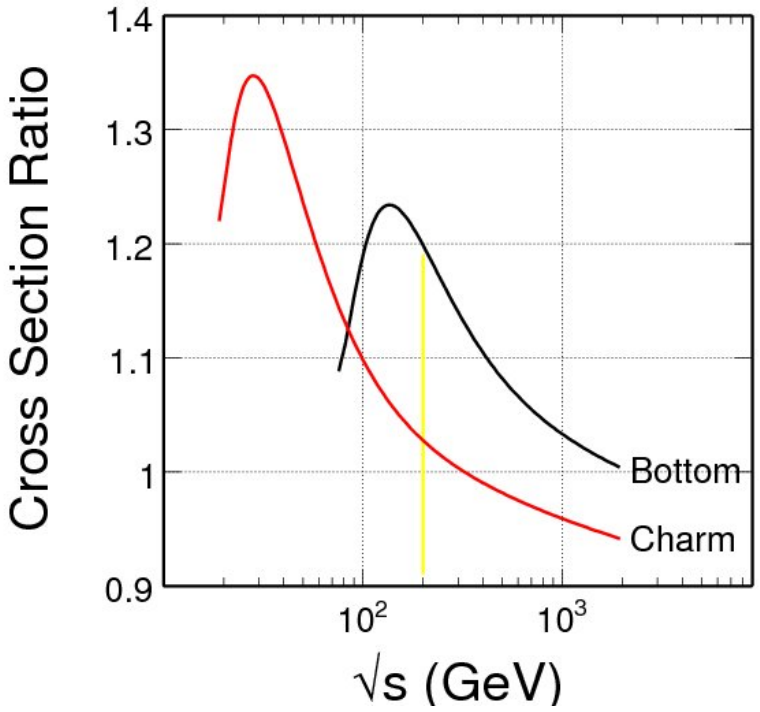

Figure 12: The ratio of mid-rapidy production cross sections in d+Au to p+p cross sections for the production of charm (red curve) and bottom (black curve) versus center of mass energy. The vertical line indicates nominal center of mass energy at RHIC.

At RHIC p+p luminosity is considerably higher than the Au+Au luminosity. Reference data can thus be obtained with reasonable beam time allocations. The collision rate is higher, but the number of tracks originating from a proton-proton collision is typically much lower than from a heavy-ion collision.

Heavy flavor production has received considerable attention since many measurements suggested discrepancies with next-to-leading order (NLO) Quantum Chromodynamics (QCD) evaluations. New evaluations and better measurements have reduced the discrepancies to a level where, in several cases, they are no longer significant[79]. For example, the evaluations for the inclusive hadro-production of D^0, D^+, D^{*+}, and D_s^+ have been reconciled with CDF measurements at 1.96 TeV center of mass energy[80]. HERA-B has recently presented preliminary results their open charm measurements at 42 GeV center of mass energy[81].

Data in the intermediate center of mass energy region remain scarce. Pioneering open charm measurements have been made, without detection of the displaced vertex, by STAR and PHENIX using p+p, d+Au, and Au+Au collisions at 130 and 200 GeV center of mass energy. Theory, in the form of NLO[82] and First-Order-Next-to-Leading-Log (FONLL) QCD calculations[83], undershoots the results, particularly at large transverse momenta p_T [84]. In contrast, inclusive jet, hadron, and photon production are well

described at RHIC energies[85] by NLO calculations and suitable choices of parton distribution and fragmentation functions.

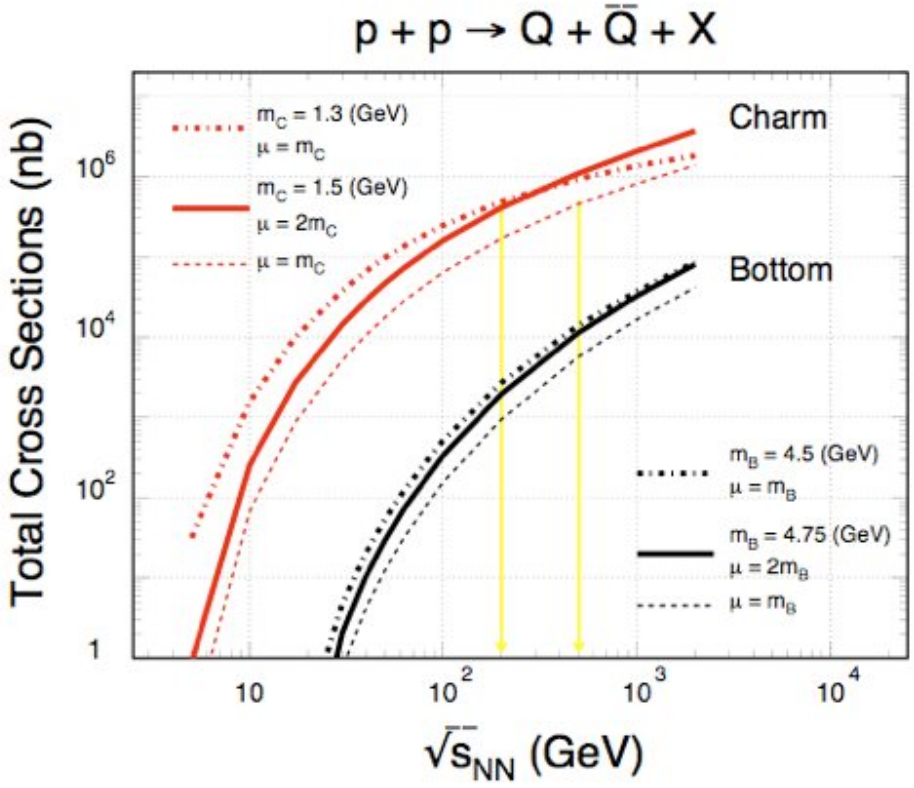

Figure 13: NLO pQCD predictions of charm (red lines) and bottom (black lines) for the total p+p hadroproduction cross sections versus center of mass energy. The vertical lines indicate the 200 GeV and 500 GeV center of mass energies for polarized p+p collisions at RHIC.

Figure 13 shows the NLO pQCD predictions of charm (red lines) and bottom (black lines) total cross-sections, as a function of center of mass energy, in hadronic p+p collisions. In the calculations, renormalization scale and factorization scale were chosen to be equal[82]. Large uncertainties exist in the factorization scales in current pQCD calculations for heavy flavor production, thus emphasizing the need for reference measurements. Future measurement of mid-rapidity cross-sections of charm- and bottom-hadrons by the combination of topologically reconstructed charm-hadrons and decay-electrons in 200 and 500 GeV p+p collisions at RHIC, as well as at the LHC injection energy 900 GeV, should provide stringent benchmarks within the 100 – 1000 GeV for improved theoretical evaluations. In addition, these results are crucial reference data for Quarkonium measurements in heavy ion collisions at both RHIC and the LHC.

In future, as part of the Spin Physics program, RHIC will collide polarized protons also at a higher center of mass energy of 500 GeV. Large integrated luminosities are projected for both 200 and 500 GeV polarized proton beam operation. Direct reconstruction of

open charm using displaced vertexing techniques will thus allow detailed measurement of the cross sections for open charm and open bottom production at two center of mass energies, as well as their spin dependences, with a single experiment.

The spin dependence is illustrated in Figure 14, showing a leading-order (LO) evaluation of the charm and bottom total cross section asymmetry for proton collisions with equal and opposite helicity configurations[86]. In LO it involves the polarized gluon luminosity and the partonic scattering asymmetry. Different gluon polarization parametrizations produce a large spread in the calculated cross section asymmetry. The partonic scattering asymmetry is calculable and has the unique property that it changes sign with increasing transverse momentum[87]. At RHIC energies, the relatively small size of the cross section asymmetry thus involves a partial cancellation and more sizable *negative* asymmetries are expected in LO for e.g. the longitudinal double spin asymmetry A_{LL} for electrons from heavy flavor decay. The evaluation of NLO contributions has recently been completed[88]. Detailed study of the differential spin cross section asymmetry constitutes a test of the spin structure of the QCD matrix elements, unless gluon polarization in the polarized nucleon is found to be exceedingly small.

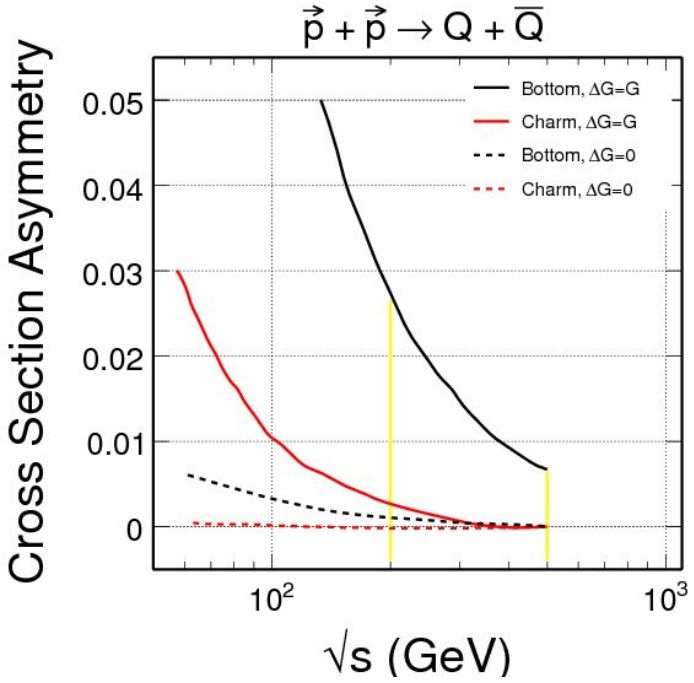

Figure 14: LO evaluation of the total cross section asymmetry for equal and opposite proton beam helicities for charm (red lines) and bottom (black lines) for two gluon polarization scenarios. The vertical lines indicate the 200 GeV and 500 GeV center of mass energies for polarized p+p collisions at RHIC.

Other possibilities with spin, heavy flavor, and future very high integrated luminosities at RHIC-II may include the measurement of the transverse double spin asymmetry A_{TT}, which is sensitive to the transversity structure in the proton[89], and at 500 GeV center of

mass energy the measurement of the parity violating spin asymmetry A_L in charm-associated W production, which is sensitive to strange quark polarization in the nucleon[90].

3 HFT Overview and Simulation

3.1 STAR and the HFT detector system

STAR[91] was designed to make measurements of hadron production over a large solid angle, and it features detector systems for high precision tracking, momentum analysis and particle identification (see Figure 15). It is the only experiment at RHIC which measures the full azimuth in ϕ out to ± 1.5 units in rapidity, and tracks particles from 100 MeV/*c* to 20 GeV/*c*, so it is well suited for event-by-event characterizations of heavy ion collisions and for the detection of hadron jets.

By adding a Heavy Flavor Tracker (HFT) to STAR, we will be able to measure neutral and charged particles with displaced vertices that decay 100 microns, or less, from the primary vertex. The high spatial resolution of the tracker will allow us to study parent particles with a very short lifetime, such as the D^0 meson. The addition of the HFT will extend STAR's unique capabilities even further by providing direct topological identification of hadrons containing charm and beauty and for non-photonic electrons decaying from charm and beauty hadrons. Thus, the HFT is the enabling technology for making direct and indirect charm and beauty measurements at STAR.

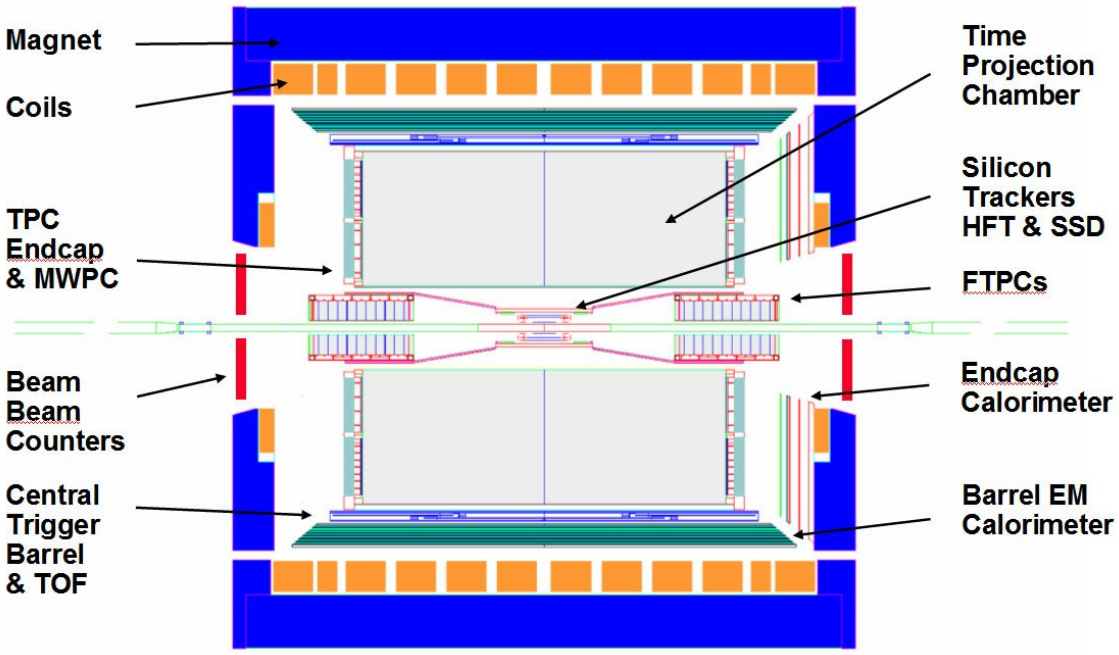

Figure 15: The STAR detector at RHIC. The primary detector systems at mid-rapidity are shown in this schematic view of the detector. The TPC is 4.2 meters long and 4 meters in diameter. Heavy Ion beams enter from the left and right while collisions take place in the center of the detector.

At the present time, the STAR detector has modest capabilities to measure secondary decay vertices that are displaced from the primary vertex. To make thee measurements, we use the TPC and the SSD to determine the position of the primary vertex to a precision of approximately 100 μm in a central collision (but less in a peripheral collision). Then, by identifying decay vertices that are displaced from the primary vertex, we can identify secondary decays of neutral and charged particles.

For example, it is possible to use this technique to identify the K_S^0 because a K_S^0 decays into two pions with a mean lifetime of 0.896×10^{-10} seconds and it has a characteristic decay distance of 2.68 cm. Since its decay distance is so much greater than the STAR vertex resolution, this particle can be easily identified. Similarly, strange particle decays such as the Ω baryon can also be identified.

The addition of the HFT to STAR will improve the single track pointing accuracy of the suite of detectors by a factor of 15, and thus the HFT allows us to measure very short-lived particles by increasing the resolution for finding secondary decays near the vertex.

STAR has several mid-rapidity tracking detectors that are essential for the best performance of the HFT. For example, the Time Projection Chamber[92] (TPC) and the Silicon Strip Detector[102] (SSD) are existing detectors and are shown in Figure 15. At the time of HFT installation, a complete Time of Flight detector will be available and it will cover 2π in azimuth. The TOF detector will replace the Central Trigger Barrel (CTB), which is currently a simple array of scintillators without TOF information. The new TOF detector will surround the outer field cage of the TPC and will extend the PID region where kaons, pions, and protons can be separated from below 1 GeV/c to well above 1 GeV/c. Also by the time the HFT is installed in STAR, the existing Silicon Vertex Tracker (SVT) will be decommissioned and will be removed from STAR in order to make room for the HFT.

The design of the HFT tracking system is dependent on the performance of the existing detectors in STAR; for example, consider an outside-in tracking algorithm. The TPC measures a total of 45 points along the track of a particle between a radius of 190 cm and 60 cm. These measurements define a path with a narrow angular constraint along the track of the particle as it is projected forward to the vertex. The projected path of the particle outside of the TPC is slightly less than 1 mm^2, in the transverse dimension, but it diverges by only ~2 mrad along its path to the vertex due to the constraints provided by the multiple measurements in the TPC. Thus, the TPC defines a nearly parallel-beam path.

The SSD is located at a radius of 23 cm and is an intermediate space point between the vertex and the TPC with a resolution of 30 μm in the r-ϕ direction and 800 μm in the Z direction. The SSD is an ideal companion to the TPC tracking system because it provides a pinhole through which the TPC tracks must pass and thereby reduces the transverse

dimensions of the projected path of the particle without changing the angular divergence of the path very much. In fact, the angular divergence of the projected path after passing through the SSD is limited only by the MCS in the Si strips and so it is a good thing that the SSD is very thin (1% radiation length).

In the remainder of this chapter, we will simulate the performance of the HFT and show how it can be used to improve the performance of the TPC plus SSD tracking system.

3.2 The Design Parameters for the HFT

The Heavy Flavor Tracker consists of two sub-detectors: a silicon pixel detector (PIXEL) and an intermediate silicon tracker (IST). Both detectors lie inside the SSD. The primary purpose of the SSD-IST-PIXEL detector is to provide graded resolution from the TPC in to the interaction point and to provide excellent pointing resolution at the interaction point for resolving secondary particles and non-vertex decays. For example, the TPC points at the SSD with a resolution of about 1 mm, the SSD will point at the IST with a resolution of ~300 μm, the IST will points at the PIXEL with a resolution of ~200 μm, and the pixel detector will point at the vertex with less than 50 μm resolution. See Figure 16.

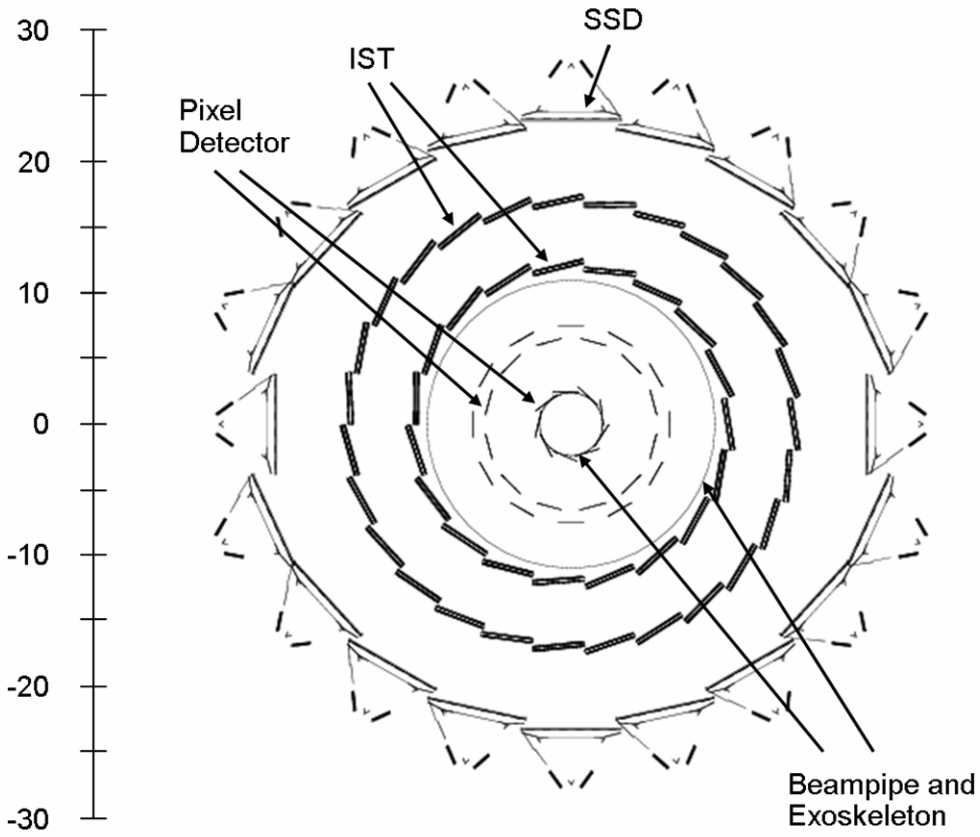

Figure 16: A schematic view of the Si detectors that will surround the beampipe. The SSD is an existing detector and it is the outmost detector shown in the diagram. It lies at a radius of 23 cm. The IST will lie inside the SSD and the PIXEL will lie inside the IST and closest to the beampipe. The beampipe and its exoskeleton are also shown in the figure.

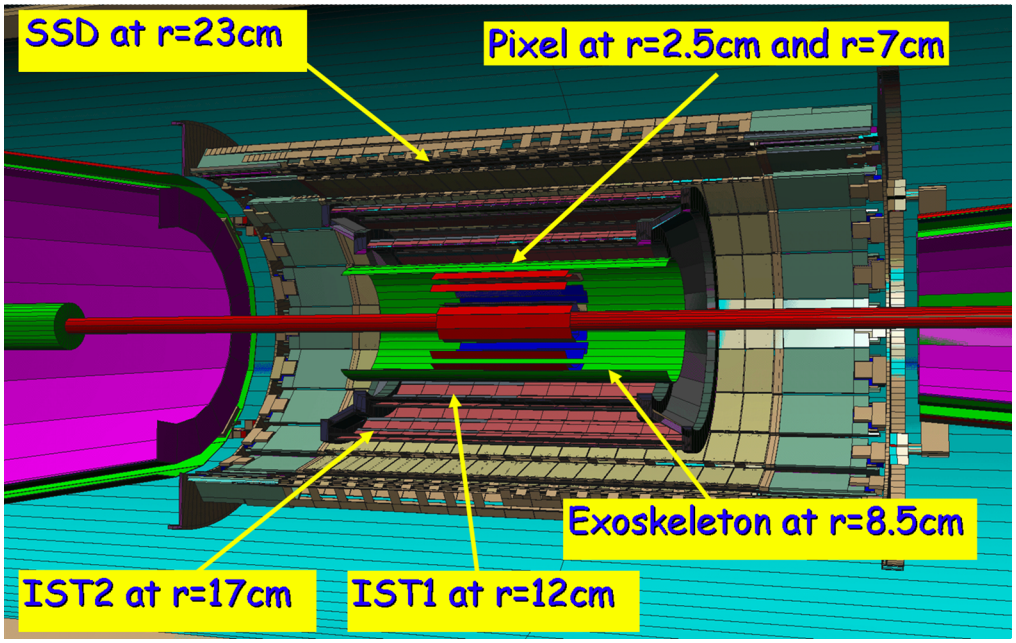

Figure 17: An oblique view of the proposed geometry for the STAR mid-rapidity tracking upgrade. From the outer to the inner radius, the detectors are the SSD (black), the two IST layers (pink), the exoskeleton to strengthen the beam pipe (green), the two Pixel layers (red), and the beam pipe (red).

The Silicon Strip Detector (SSD) is an existing detector and, as mentioned, it lies at a radius of 23 cm. It is built using 20 ladders of 67 cm length with double-sided wafers having 95 μm × 4.2 cm strips crossed at an angle of 35 mrad. The strips are oriented so as to improve the R-ϕ resolution. For tracks at mid-rapidity, the SSD detector material amounts to ~1% radiation length. Although the SSD is not discussed further in the main body of this write-up, it's projected performance has been included and used in the simulations described below (See Appendix I for further information)

The IST lies inside the SSD. The IST is designed to match the high resolution of the PIXEL with the courser resolution of the TPC and the SSD. In order to provide the required graded resolution between the SSD and the pixel layers, two additional high rate conventional silicon barrel layers will be installed at radii of 12 cm and 17 cm. The IST layers provide space-points with high accuracy in the r-ϕ and the z direction, respectively, thereby reducing the number of possible candidate tracks that can be connected with hits on the outer layer of the pixel detectors. This is particularly crucial to enable accurate measurements in high multiplicity environments.

Each of the IST layers will be assembled from ladders. The proposed outer layer lies at a radius of 17 cm, and consists of 27 ladders of 52 cm length. The proposed inner layer, at a radius of 12 cm, consists of 19 ladders of 40 cm length. See Table 3. The ladders are envisioned to carry commercially available 300 μm thick, 4 cm long, single-sided silicon strip sensors mounted on high thermal conductivity carbon foam as a core and 100 μm

kapton hybrids. For the proposed IST, the detector material budget is ~0.75% radiation length for each layer, including hybrids, ladder material, and the support structure.

The strip geometry that has been simulated uses 60 μm × 4.0 cm strips. The resolution of each strip is $1/\sqrt{12}$ times the width of the strip, or about 17 μm. The strips on the outer layer of the IST are oriented to give good resolution in the Z direction and the strips on the inner layer are oriented to give the best resolution in the R-ϕ direction in order to best complement the orientation and performance of the SSD. We are also studying the option to add another layer of strip detectors at 17 cm radius. The need for this layer is still to be determined, but it would utilize strips rotated in the other direction so that it provides additional resolution in the R-ϕ direction. This optional layer provides tracking information that is redundant with the SSD, but it would become the only R-ϕ information available between the TPC (60 cm) and the inner layer of the IST (12 cm) if part of the SSD should be temporarily out of service. The optional layer is not included in Table 3.

Total number of strips/channels	346,240
Number of barrels	2
Number of ladders	46
Outer barrel (27 ladders)	r = 17 cm
Inner barrel (19 ladders)	r = 12 cm
Detector Module active area	4 cm × 4 cm
Thickness: Si on Ladder (w/APV25)	0.75 % X_0
Strip dimension (outer)	60 μm × 4 cm
Orientation of Strips (outer)	best resolution in Z
Strip dimension (inner)	60 μm × 2 cm
Orientation of Strips (inner)	best resolution in R-ϕ
Resolution of one strip	17 μm
Rapidity Coverage	± 1.2 units

Table 3: Selected parameters for the IST. These parameters were used in the simulation of the physics performance of the system.

The PIXEL is a low mass detector that will be located very close to the beam pipe. It will be built with two layers of silicon pixel detectors; one layer at 2.5 cm average radius and the other at 7.0 cm average radius. The outer layer will have 24 ladders and the inner layer will have 9 ladders; for a total of 33. Each ladder contains a row of 10 monolithic CMOS detector chips and each ladder has an active area of 19.2 cm × 1.92 cm. The CMOS chips contains a 640 × 640 array of 30 μm square pixels and will be thinned down to a thickness of 50 μm to minimize multiple coulomb scattering (MCS) in the detector. The effective thickness of each ladder is 0.28% of a radiation length. See Table 4.

Number of pixels	135,168,000
Pixel dimension	30 μm × 30 μm
Resolution of one pixel	9 μm
Detector Chip active area	19.2 mm × 19.2 mm
Detector Chip pixel array	640 × 640
Number of ladders	33
Ladder active area	192 mm × 19.2 mm
Number of barrels	2
Outer barrel (24 ladders)	r = 7.0 cm
Inner barrel (9 ladders)	r = 2.5 cm
Frame read time	0.2 μsec
Rapidity Coverage	± 1.2 units
Thickness: Si on Ladder (w/Al cable)	0.28 % X_0
Beam Pipe Thickness	0.5 mm or 0.14 % X_0

Table 4: Selected parameters for the pixel detector. These parameters were used in the simulation of the physics performance of the system.

The PIXEL will achieve maximum vertex resolution by lying as close as possible to the interaction point without residing inside the RHIC beam pipe. To bring the detector to a 2.5 cm radius will require a new, smaller, beam pipe. This new design also presents us the opportunity to make the beam pipe thinner (0.5 mm). The new beam pipe, which will reduce the MCS scattering in front of the HFT, is an essential part of the proposal and its design will be discussed in section 6.2.

3.3 A Simple Estimate of Detector Performance

A great deal can be learned about the detector by using a pocket-formula because the goal is to design a very high resolution tracking detector that is limited only by the multiple coulomb scattering (MCS) in the various detector layers. Assuming an outside-in tracking algorithm, the vertex pointing resolution of the HFT is determined by the layers of the Pixel detector and does not depend on the IST, SSD, or TPC. These other detectors are needed to associate the Pixel detector hits with a projected track, and do it with high efficiency, but otherwise these detectors do not play a large role in determining the pointing accuracy of the HFT. In fact, in an MCS limited system, the pointing resolution at any point can be estimated by the resolution and MCS from the previous two layers of tracking detectors.

The single track pointing resolution for a two layer detector telescope has three terms which are shown in Equation 1. The first two terms represent the pointing accuracy associated with detector position resolution. The third term represents the error due to the MCS in the layer closest to the target. Thus:

(1) $$\sigma^2 = \frac{\sigma_1^2 r_2^2 + \sigma_2^2 r_1^2}{(r_2 - r_1)^2} + \frac{\theta_{mcs}^2 r_1^2}{\sin^2(\theta)}$$

where r_1 and r_2 are the radii of the two detectors, σ_1 and σ_2 are the resolution of the detectors, θ is the tilt angle of the track with respect to the detector, and θ_{mcs} is the width of the multiple coulomb scattering angular distribution in the first layer of the tracker (corresponding to r_1).

θ_{mcs} is momentum dependent and is given approximately by:

(2) $$\theta_{mcs} = \frac{13.6\,(MeV/c)}{\beta\ p}\sqrt{\frac{x}{X_0}}$$

where the thickness of the detector is measured in radiation lengths, p is the particle momentum, and $\beta = p/E$. So for example, the multiple scattering width at 750 MeV for a kaon passing through a 0.28% thick Si detector is ~1.2 milli-radians. This is a useful number because it represents the MCS for a kaon at mean p_T from a $D^0 \rightarrow K + \pi$ decay. It is precisely these kaons that must be tracked with high precision in the pixel detector.

Using these formulae and the parameters in Table 4, we can estimate the pointing accuracy of the PIXEL. Not including multiple coulomb scattering in the beam pipe, the predicted resolution of the detector will be approximately 30 μm for 750 MeV/c tracks. A more complete prediction is shown in Figure 18. The calculations shown in the figure are for 'straight up tracks', meaning that the tilt angle of the track is perpendicular to the surface of the detector. It is worth noting that the resolution of each pixel is so high (9 μm) that the predicted pointing resolution of the detector is dominated by the MCS in the silicon. Thus, the pointing resolution of the full detector is not sensitive to modest changes in the radial location of the Si layers or the resolution of each pixel. The detector is MCS limited as planned, and expected.

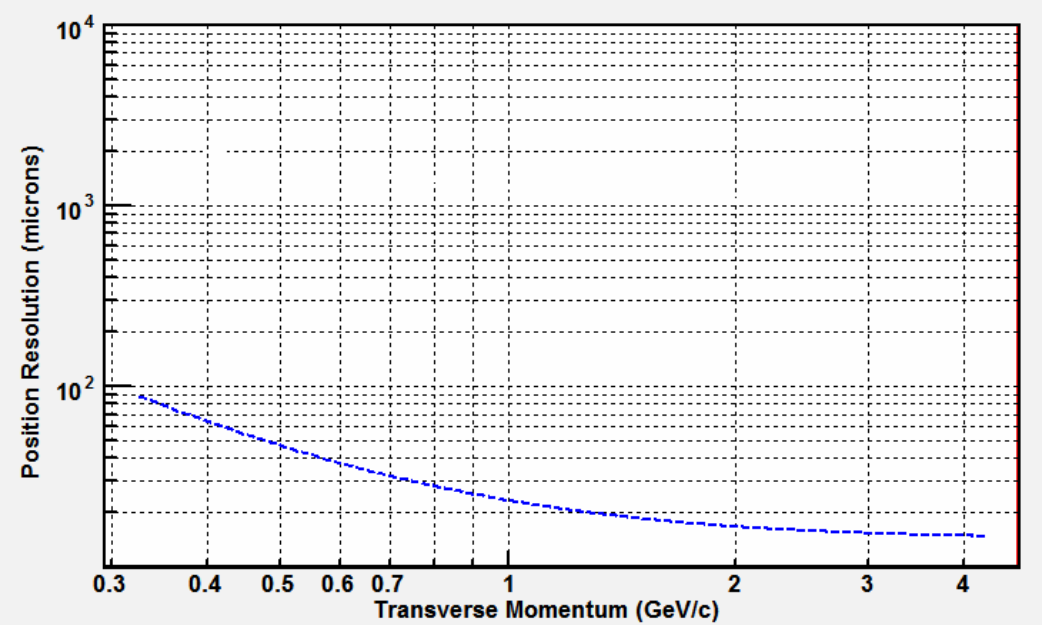

Figure 18: The predicted resolution of the pixel detector as a function of p_T based on equations (1) and (2). The beampipe is not included in these calculations and the tracks are assumed to travel perpendicularly to the detector layers.

It is possible to simulate the performance of the full TPC+SSD+HFT system by iterative application of equations 1.) and 2.) … but it is tedious. A better technique was developed by Billoir[93]. The essential ingredients of Billoir's method are shown schematically in Figure 19. Consider a series of detector elements with finite resolution and a finite thickness for MCS in each element. He introduces a 5x5 information matrix that represents MCS in a layer of the detector, and another for a measurement with resolution σ at the layer, and finally a matrix to represent the propagation of a particle over the distance D between two consecutive layers.

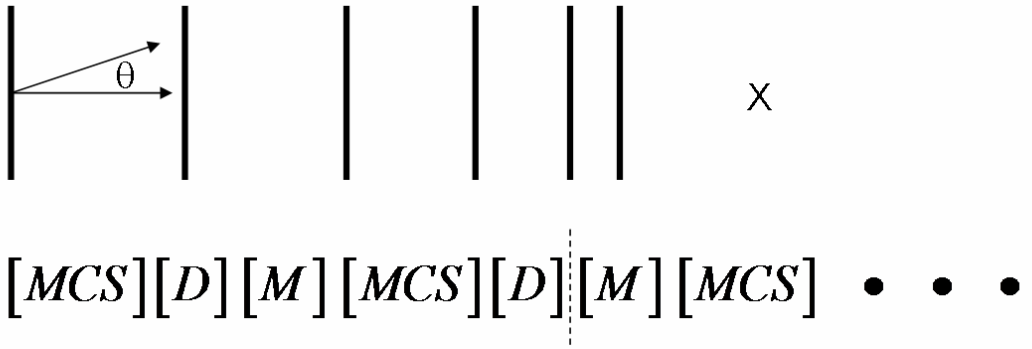

Figure 19 Billoir's method of matrices involves multiplying information matrices; three for each active layer in a detector system. The 'x' marks the vertex position under a hypothetical collider detector and we assume outside-in tracking (left to right). The matrix multiplications follow the track of a particle from the outside of the detector – in to the vertex. [MCS] represents the matrix for multiple coulomb scattering, [D] represents the matrix for propagation between two layers, and [M] represents the matrix for the measurement at a layer with resolution σ.

The performance of a particular detector system is calculated by multiplying the three matrices for each layer, in order, and repeating the multiplication for all layers. Finally, the resulting matrix is applied to a basis vector describing a particle traveling through space with finite momentum. The procedure looks like beam transport dynamics, but of course, is different.

The only significant approximation that is made in the development of the matrix elements is that Billoir assumes that the magnetic field is constant between two layers. This is not a limitation because in STAR's case, the magnetic field is constant everywhere; and in the more general case, the method can still be used by introducing pseudo-layers frequently enough to accommodate a changing magnetic field.

An interesting comment on the procedure revolves around the fact that matrix multiplication is not commutative. It is neccesary to stop the matrix multiplication at the appropriate point because the procedure does not work when going backwards. So for example, to know the pointing resolution at a particular detector element, then one should multiply the appropriate matrices but stop after applying the D matrix that represents transport to the target layer. If one applies the measurement matrix (M) at the target layer, then one will only learn about the measurement resolution of the target layer rather than the pointing resolution to it.

Using these tools we can simulate the HFT as it is embedded in STAR detector. See Figure 20. The solid blue line is the predicted pointing resolution for the full system.

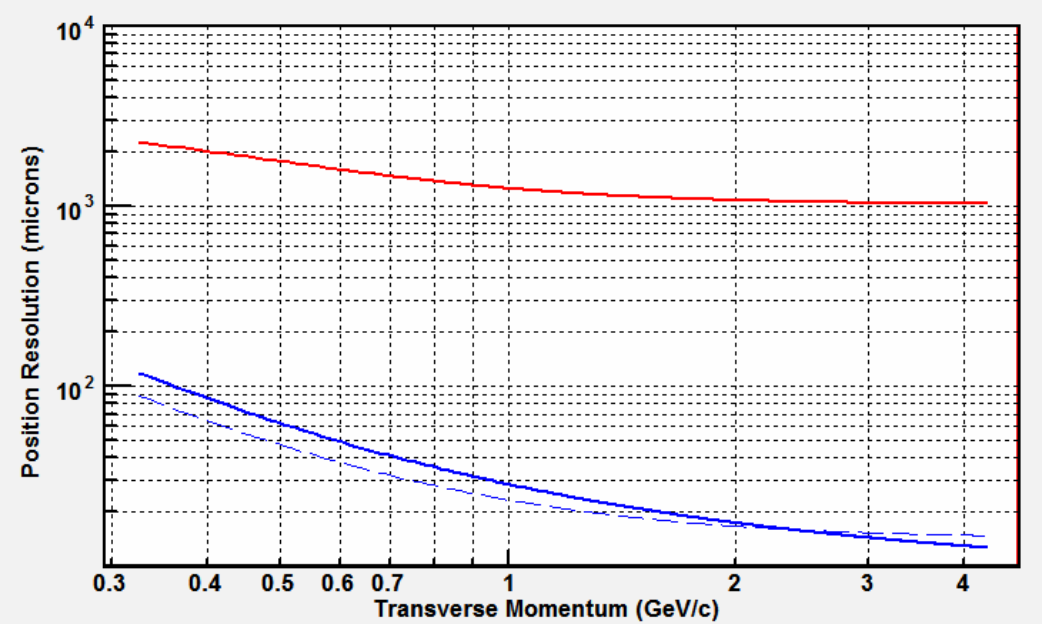

Figure 20: Billor's method of matrices is used to estimate the pointing resolution at the vertex by the TPC+SSD+IST+Pixel detector (solid Blue line). The pointing resolution of the TPC, acting alone, is shown for comparison (Red). The dashed line is the same line shown in the previous figure.

The calculations underlying Figure 20 include the 45 rows of the TPC, its inner field cage (a source of MCS), the SSD, the IST, the Pixel detector layers and the beam-pipe. The solid blue line represents the resolution of the full system pointing at the vertex. The dashed line is the same line shown in Figure 18 and it represents the theoretical limit of the pointing resolution for a two layer pixel detector without other elements such as the beam pipe. We can clearly see the effect of the beampipe below 2 GeV/c. Above 2 GeV/c, an interesting thing happens: the TPC track is so long that it provides a very tight angular constraint that ultimately exceeds the angular constraints imposed by the pixel detector at high p_T even though the pixel detector has 30 μm elements. This is only visible at high p_T when MCS is small and no longer dominates the resolution calculations.

The red line in Figure 20 represents the pointing resolution of the TPC acting alone. Obviously, the pointing resolution of the TPC acting alone is not sufficient to find hits on a detector close to the vertex that is segmented into 30 μm pixels. Intermediate tracking layers with graded resolution between the TPC and the pixel detector are required in order to enable the association of tracks found in the TPC with hits on the pixel detector. That is precisely why we must use the SSD and why we propose to add additional layers of tracking with the IST detector. Table 5 shows the pointing resolution of the TPC+SSD+IST+Pixel detectors at intermediate points along the path of a particle as it is tracked from the outside going in. These calculations were done using Billoir's method and the quoted resolutions are for $\sqrt{[(\text{R-}\phi \text{ resolution})^2 + (\text{Z resolution})^2]}$ when the R-ϕ and Z resolutions differ … which they do at several points in the system.

Graded Resolution from the Outside - In		
TPC pointing at the SSD	(23 cm radius)	~ 1 mm
SSD pointing at IST-2	(17 cm radius)	~ 330 μm
IST-2 pointing at IST-1	(12 cm radius)	~ 250 μm
IST-1 pointing at Pixel-2	(7 cm radius)	~ 250 μm
Pixel-2 pointing at Pixel-1	(2.5 cm radius)	~ 80 μm
Pixel-1 pointing at the vertex		~ 40 μm

Table 5: The calculated pointing resolution of the TPC+SSD+IST+PIXEL detector at intermediate points along the path of a particle as it is tracked from the outside – in. The intermediate pointing resolution is critical to being able resolve ambiguous hits on the next layer of the tracking system.

Extending the TPC tracks in towards the vertex will turn out to be a difficult problem because the pixel detectors are so close to the interaction vertex that they suffer a significant density of hits in central Au-Au collisions and a TPC track can easily point at several hits on the pixel layers that lie within the pointing accuracy of the TPC (acting alone). Before considering this problem further, lets explore the hit density on the front surface of the pixel detectors.

3.4 Hit Density at the Front Surface of the Pixel Detector

There are several issues that may affect the performance of the proposed HFT detector. The PIXEL is not triggered and is continually active, recording all particles that pass through it. This means that in tracking the events of interest there will be extraneous hits and pileup in the detector due to other collisions at an earlier or later time, tracks from beam gas showers, and other background sources. The areal density of extraneous hits that can be tolerated depends on the tracking precision projected onto the PIXEL surfaces and on details of the particle reconstruction algorithms; while the extraneous hit density depends on the PIXEL frame readout speed, beam luminosity, interaction cross sections and background rates from additional sources. Reasonable limits on these processes have been included in the simulations. The focus of this section is to discuss and quantify these and other background issues that go into the simulations.

To set the scale of the problem, consider the extraneous hit density from normal interactions. The parameters used in the calculation are shown in , Table 6 and an estimate of the hit density is shown in Table 7.

Au + Au Luminosity	8×10^{27} cm^{-2}s^{-1}
dN/dη (min bias)	170
dN/dη (central)	700
Min bias cross section	10 barns
Interaction diamond size, σ	15 cm

, Table 6: Luminosity and other parameters that determine the particle flux on the HFT.

	PIXEL Outer Layer	PIXEL Inner Layer
Radius	5.0 cm	2.5 cm
Hit Flux	5,600 Hz/cm^2	28,750 Hz/cm^2
Hit Density 4 ms Integration	22.5/cm^2	115/cm^2
Projected Tracking Window Area	0.6 mm^2	0.15 mm^2
PIXEL Hit Resolving Area	0.001 mm^2	0.001 mm^2
Probability of PIXEL Pileup	0.3%	1%

Table 7: Integrated hit loading on the PIXEL and associated pileup.

As shown in Table 7, the accumulated hit density from the integrated Au + Au collisions is 22.5/cm^2 in the outer layer and 115/cm^2 in the inner layer of the PIXEL[94]. This produces a pileup probability in the track search window of 14% and 17% at the inner and outer PIXEL barrels, respectively. The area of the track search window in this case is based on the projection resolution for 1 GeV/c pions as determined from GEANT simulations. For comparison, the unresolved hit pileup intrinsic to the PIXEL detector is much less, 0.28%, and 1%, for the outer and inner barrel respectively.

The luminosity applied in this case is the maximum instantaneous luminosity that was recorded during the Au + Au run in 2004 (8×10^{27} cm^{-2}s^{-1}). This is 5 times the nominal "design luminosity". Design luminosity is defined to be 2×10^{26} cm^{-2}s^{-1} averaged over a 10 hour fill. The STAR Experiment measures interaction rates through the zero-degree calorimeter detector, and a RHIC instantaneous luminosity of 2×10^{26} cm^{-2}s^{-1} is equivalent to an instantaneous ZDC coincidence rate of 2000 Hz. It should be noted that the RHIC beam luminosity starts high and drops with time over the course of a fill. During the RHIC II era, the most important improvements in RHIC luminosity will be longer decay times during the fill. However, we do expect an increase in peak luminosity by about a factor of 4, which will have the largest impact on our program. This is important, and so under RHIC II conditions we will have to improve the readout time of the PIXEL in order to limit pileup in the tracking search window to about 10%.

Table 8 gives the same loading information resulting from a single central Au + Au collision. The numbers for a single collision is a factor of 10 less then the integrated load, which demonstrates that an isolated collision is easily tracked by the PIXEL.

	PIXEL Outer Layer	PIXEL Inner Layer
Radius	5.0 cm	2.5 cm
Hit Density Au + Au Central Collision	1.8/cm^2	7.4/cm^2
Projected Tracking Window Area	0.6 mm^2	0.15 mm^2
PIXEL Hit Resolving Area	0.001 mm^2	0.001 mm^2
Probability of PIXEL Pileup	0.02%	0.09%

Table 8: Hit loading on the PIXEL from Au + Au central collisions and associated pileup.

3.4.1 Measured Hit Density at 6 cm Radius in STAR

We have used the STAR SVT to actually measure the hit density that will contribute to pileup in the HFT. The SVT is the innermost detector currently available in STAR and it gives the best-hit density information closest to the interaction point. This is of interest because it can identify potential background contributions including very low momentum tracks. As it turned out the measured hit density at the SVT inner layer for central collision triggers is 1 hit/cm^2. This is consistent with the expected track density for central Au + Au collisions with $dN/d\eta = 700$, so we see no evidence of additional background beyond the pileup of normal Au + Au events[95]. This measurement was done at B = 0.25 T, half the normal STAR magnet field, to open the acceptance to lower momentum particles. It would be desirable to use SVT events with a zero bias trigger to have a measure of other background sources such as beam gas showers, but so far, our noise suppression filters for the SVT are not sufficient for this task.

Although we do not have a direct measure of beam showering, we do know from studies of space charge distortions in the STAR TPC that at larger radii, 65 cm to 200 cm, the ionization density due to normal Au + Au interactions is larger than the contributions from other sources such as beam gas[96] interactions.

3.5 Analytic Calculations for Efficiency and Ghost Rates

To verify our detailed STAR software simulation, we have made several cross checks. One method is to do a simple analytic calculation of efficiency and ghosting versus the transverse momentum.

The probability to pick up the correct hit can then be described by the following equation:

$$\int_0^a \frac{r}{\sigma^2} e^{-r^2\left(\pi\rho+\frac{1}{2\sigma^2}\right)} dr$$

The probability to pick up the wrong hit is described by the equation:

$$\int_0^a \frac{r}{\sigma^2} e^{-\frac{r^2}{2\sigma^2}} \left(1 - e^{-\pi r^2 \rho}\right) dr$$

where σ is the uncertainty in the track extrapolation from the outer detectors to the target detector, ρ is the background hits density, and 'a' (the upper limit of the integral) is the search cone radius. The analytic calculation of the quantity σ, includes contributions from multiple Coulomb scattering[97], the detector resolution, and the uncertainty in the position of the track due to the quality of the fit given by the tracking software.[98]. The quantity ρ includes contributions from the pile-up, other tracks in the current event, and ultra-peripheral collision (UPC) electrons.

We discovered that track fitting errors in the standard STAR software are the dominant term in the calculation of σ while the detector resolution drops out due to the extremely high resolution of the detectors. So in the discussion presented here, we have set σ equal to the search radius used by the tracking software at each detector layer. This suggests that the tracking software can be improved and future simulations may someday be better than what we present here.

Figure 23 shows the efficiency and ghost rate results using these equations. The vertex, HFT, SSD, and TPC search radii are assumed to be 300 μm, 60 μm, 90 um, and 1.5 mm, respectively. There is excellent agreement in sub-panels (a), (b), (c) and (d) between efficiency and ghost rate; the analytic calculations match the characteristics and shape of the distributions found with the full Monte Carlo simulations. The larger the efficiency, the smaller the ghost rate. The analytic calculations can reproduce the shape of the distribution as a function of p_T. At high p_T, the efficiency is limited by the detector resolution. The efficiency decreases quickly below 1 GeV/c due to multiple Coulomb scattering, which causes a large rise in the track projection errors at low p_T. The efficiency decreases consistently with an increase of the luminosity.

3.6 Monte Carlo Simulations

The STAR experiment makes use of an extensive simulation framework to accurately predict the performance of the physical detector. This framework involves many software packages working in tandem to produce the final results. We will give a general overview of the simulation chain in order to place the results and predictions contained in this document in a broader context.

The philosophy of the simulation is to use as much standard STAR software as possible. For instance, we use the standard GSTAR simulation package with modifications for the new beam pipe design and the introduction of the HFT. For tracking, we use the new STAR tracking software package ITTF. During the process of writing this proposal, we needed a stable platform, so we froze the ITTF software on February 5, 2005. To that

package, we added tracking in the HFT layers. Since ITTF was never optimized for the high precision requirements of the HFT, we have tuned it for this new configuration and added new support software, as required. We will indicate where this new software is used.

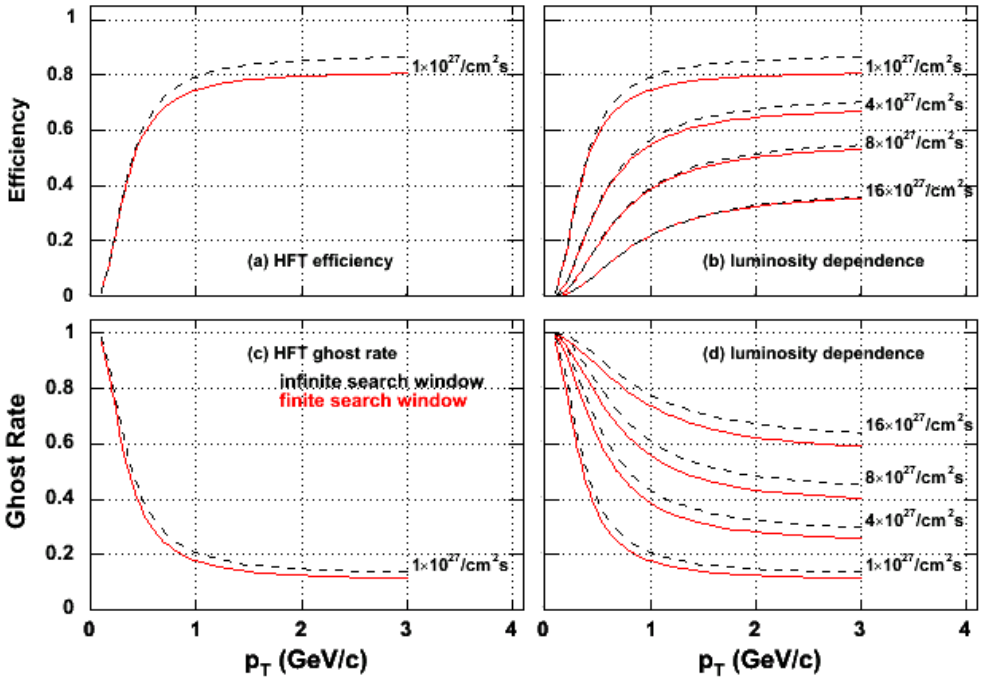

Figure 21: Efficiency (a) and ghost rate (b) of the PIXEL, using an analytic calculations. The luminosity dependence is given in (c) and (d) for 1-4 times the current peak luminosity. Finite and infinite search windows are represented by solid- and dashed- line, respectively. The efficiency and ghost rate for each layer of the PIXEL are calculated separately and combined into that for full PIXEL. The vertex, SSD, PIXEL, and TPC search radii are assumed to be 300 µm, 60 µm, 90 µm, and 1.5 mm, respectively. At nominal RHIC luminosity $1\times10^{27}/cm^2s$, the density of background hits (hits/cm^2) are summarized in Table 8. It will be necessary to upgrade the sensors for the full RHICII luminosities.

The simulation framework has three stages:

1. The simulation of the physics under study: for example a Au-Au interaction at $\sqrt{s} = 200$ GeV.
2. The simulation of produced particles as they interact with the detector and physical structures of the experiment; and finally
3. The simulation and digitization of signals in the detector.

The goal of the simulation software package is to use the same analysis methods on both the simulated and real data, to predict performance and optimize analysis methods.

3.6.1 Physics Simulation

The simulations presented in this chapter separate the charmed mesons and baryons from the rest of the event. This has the benefit of greatly increased speed for the analysis of events and for the development of algorithms. This method has been used previously by the ALICE collaboration[99]. For charm production, events with one 'signal' particle were simulated independently from the background. The background for these studies were simulated as a cocktail of pion, kaon, and protons at the maximum multiplicity expected for central collisions, and produced with the MEVSIM package developed for use in STAR[100]. The 'signal' and 'background' events are analyzed using the same reconstruction and analysis code, with the same cuts and with the same tracking parameters. (For further details see Section 3.4, , Table 6 and Table 7.)

The physical interaction between daughter particles and the material of the detector, as well as signal digitization, are simulated using the STAR implementation of the GEANT simulation package[101] This package is used in STAR and is a standard analysis tool which includes a detailed understanding of the TPC response function; including dead areas and realistic detector resolutions and responses.

For both the SSD and pixel detectors, the exact crossing point of the particle through the detector is reported by GEANT to the track reconstruction package. Realistic detector resolutions are used to smear the perfect position information, and the resulting simulated hits are used in tracking. For the SSD, the hits were smeared by 20 μm in ϕ and 750 μm in z, in agreement with the SSD specifications[102]. For the PIXEL, the hits were smeared by 6 μm in both ϕ and z. We ignore the effects of cluster overlap because we expect these effects to be minimal in the case of the PIXEL as the occupancy, even in a central Au + Au event, is relatively low.

For these simulations, the event reconstruction algorithms traditionally used in STAR were modified to optimize the PIXEL hit finding accuracy and vertex reconstruction performance. These modifications and performance improvements are detailed in the next section.

3.6.2 Reconstruction

Reconstruction of the simulated events is handled by the usual framework implemented in STAR to unite the various tracking detectors. We use this package, along with a detailed GEANT simulation, to provide an estimate of the expected performance of the HFT in the full suite of STAR detectors.

As mentioned in the introduction to this chapter, we use a vertex constraint in conjunction with the TPC and SSD detectors to provide efficient reconstruction and track

matching purity. In this algorithm, the STAR vertex finder package uses tracks defined with only the TPC and SSD to determine a primary vertex. If no vertex is found for an event, the event is lost. Since the 'signal' events contain one signal particle per event, the Monte Carlo vertex is used, but smeared with a resolution typical for events of these centralities (100μm).

With the current STAR algorithm, the tracker follows a series of hits in the TPC and SSD, refitting after every new hit is added. These tracks (called "global" tracks) are then passed to the vertex finder, which reconstructs the event vertex. The global tracks are extended to the resulting reconstructed vertex, and, if the fit is successful, the new track is stored and labeled a primary track.

The new algorithm simply takes these primary tracks and refits the track, this time with the PIXEL hits available. PIXEL hits that meet the tracking selection criteria are added. The Kalman fitter updates the track fit as the new PIXEL hits are added. The tracks with added PIXEL hits are then stored See Figure 22 for a block diagram of this algorithm. The success of the algorithm depends on the precision of finding the primary vertex, which is centrality dependent.

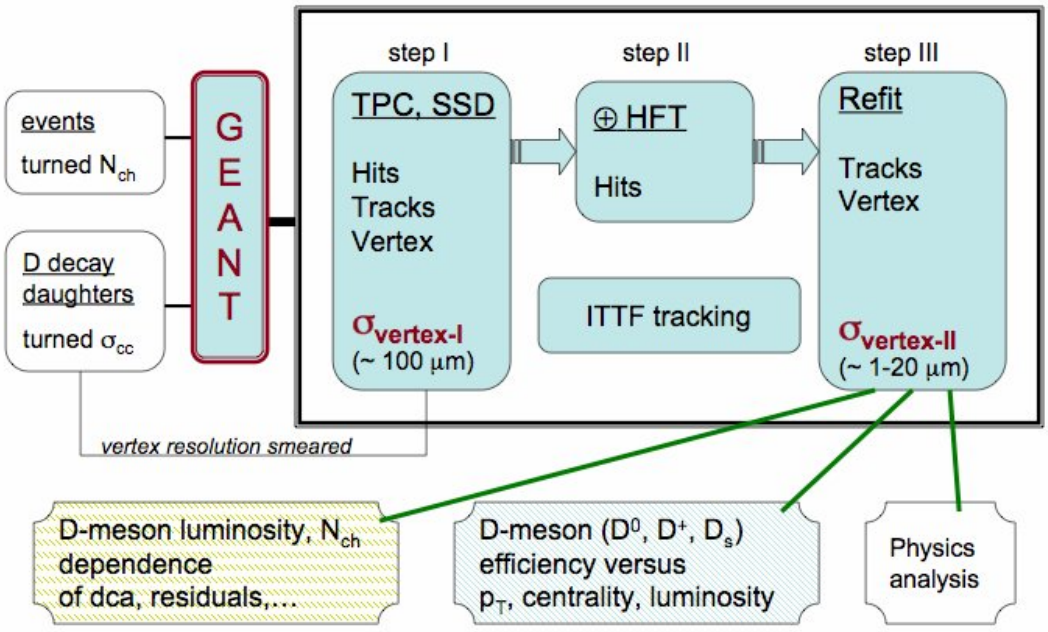

Figure 22: Simulation block flow diagram. Only small modifications were needed to optimize the STAR reconstruction software for use with the PIXEL.

The dramatic improvement of the track fit at this stage allows a more accurate primary vertex fit. A simplified vertex algorithm was adopted for this refit. The distribution of the distance of closest approach for each PIXEL track to the TPC + SSD primary vertex shows a distinct offset from zero, as well as a non-gaussian shape (see Figure 23). The

offset (calculated in three dimensions) is used as a correction to the primary vertex position. We found that iterating on this procedure produced the best resolution (see Figure 24). A final vertex position resolution of 8 μm was achieved for the highest multiplicity events, while in the most general case the vertex resolution follows the functional form:

$$\sigma = \frac{380\mu m}{\sqrt{N_{ch}}}$$

where N_{ch} is the multiplicity of charged particles in the detector acceptance. The vertex resolution functional form follows Poisson statistics, as expected. This functional form is drawn as a line to guide the eye in Figure 25. The highlighted region in Figure 25 demarcates the centrality region of TPC + SSD vertex resolution that is useful and allows the tracking code to achieve the necessary hit purity in the PIXEL. The highlighted region corresponds to 0%-60% centrality in Au-Au collisions or, equivalently, to a multiplicity of $N_{ch} > 90$.

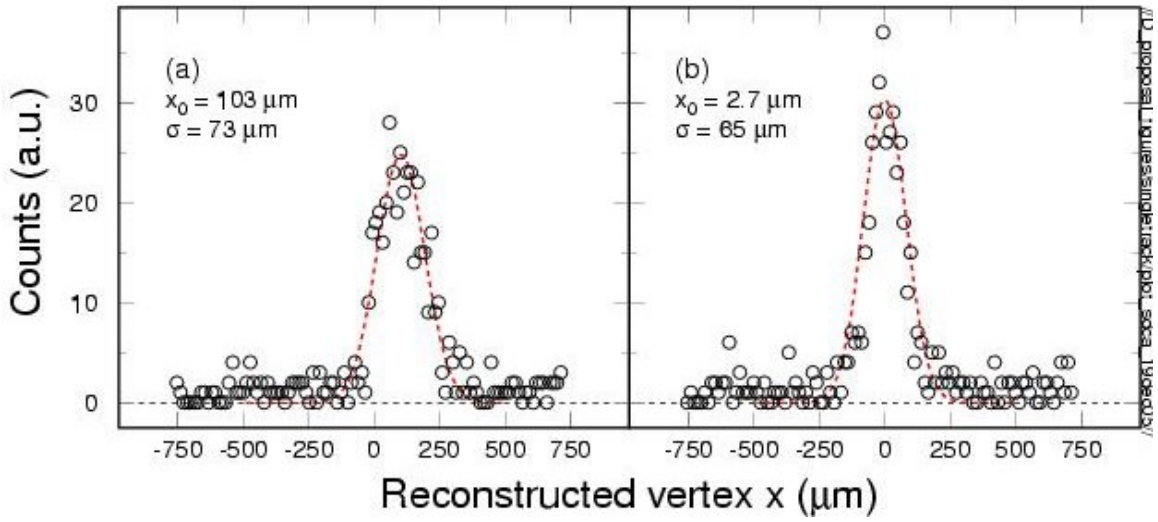

Figure 23: DCA of tracks to the Primary vertex. The geometric signed distance of closest approach between all tracks (p_T > 200MeV/c) and the vertex is shown for two cases: a) DCA to the vertex defined by TPC+SSD tracks. The non-zero mean of this distribution is used to correct the vertex coordinate. b) DCA distribution after iterative correction using TPC+SSD+HFT tracks, with a significant improvement in the mean and shape of the distribution.

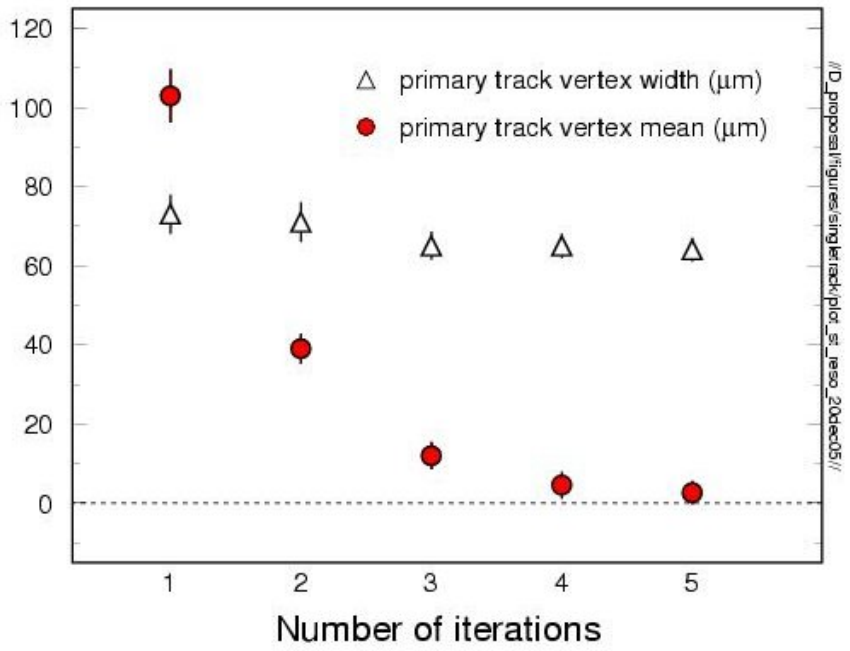

Figure 24: Mean and sigma of the geometric – signed DCA distribution as a function of the number of iterations used to correct the vertex. With each iteration, the previously defined vertex is corrected with the mean of the distribution of the track dca's. The first iteration uses the TPC+SSD defined vertex as a vertex seed.

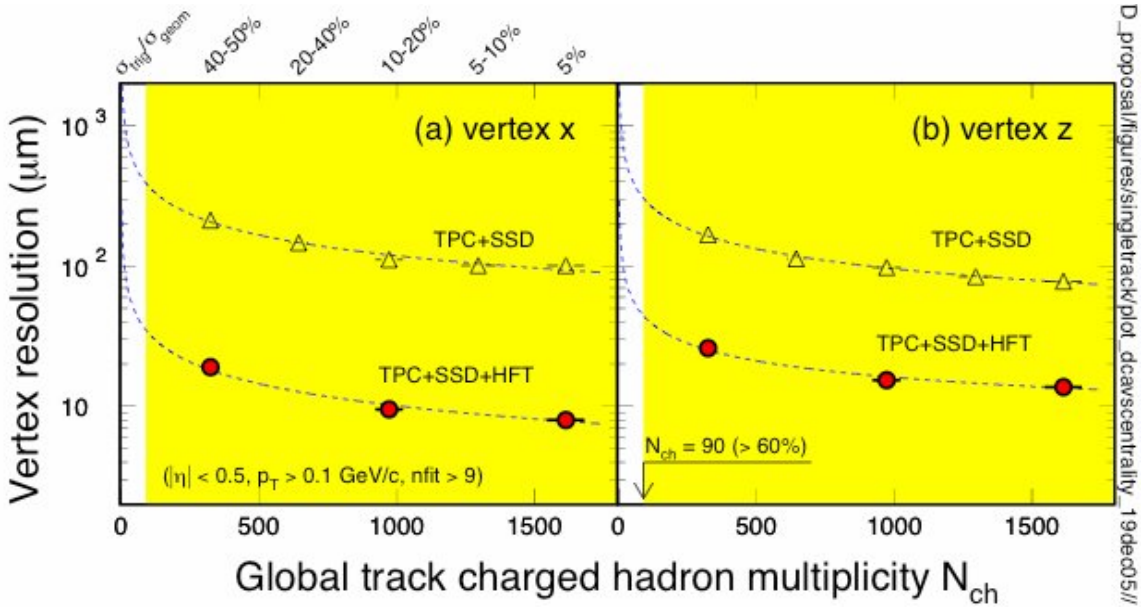

Figure 25: Vertex resolution σ(MC Vertex Position – Reconstructed Vertex position) as a function of collision centrality. The PIXEL refit vertex shows an order of magnitude improvement over the previously reconstructed primary vertex. a) Vertex resolution in X vs. N_{ch} . b) Vertex resolution along the beam direction. Problems in the vertex fit in the z direction drive the distribution wider than in the transverse direction. The highlighted area demarcates the centrality region with minimum (or better) acceptable TPC+SSD vertex resolution. This corresponds to 0%-60% most central events.

Application of a vertex constraint before adding detector hits is a new tool for the STAR software chain, and this technique requires minor modifications of the STAR reconstruction code. The performance of this algorithm has been studied in terms of the efficiency and the expected rate of false hit associations.

The efficiency of the reconstruction package to find and correctly associate HFT hits is defined as:

$$\varepsilon = \frac{N_{reconstructred}}{N_{MC,\,Accepted}}$$

where the reconstructed tracks are matched to their corresponding Monte Carlo track at the hit level. Tracks that do not match, or which only partially match, to a Monte Carlo track , do not contribute to the efficiency. Hit matching requirements are set to 33% in the TPC (15 hits), 100% in the SSD (1 hit) and 100% in the HFT (2 hits). Tracks with one or more non-matched HFT hit are designated as 'ghost' tracks. The measured efficiency as a function of p_T is ~50% for p_T > 1 GeV/c (see Figure 26) and the level of ghosting is 14% over the same range.

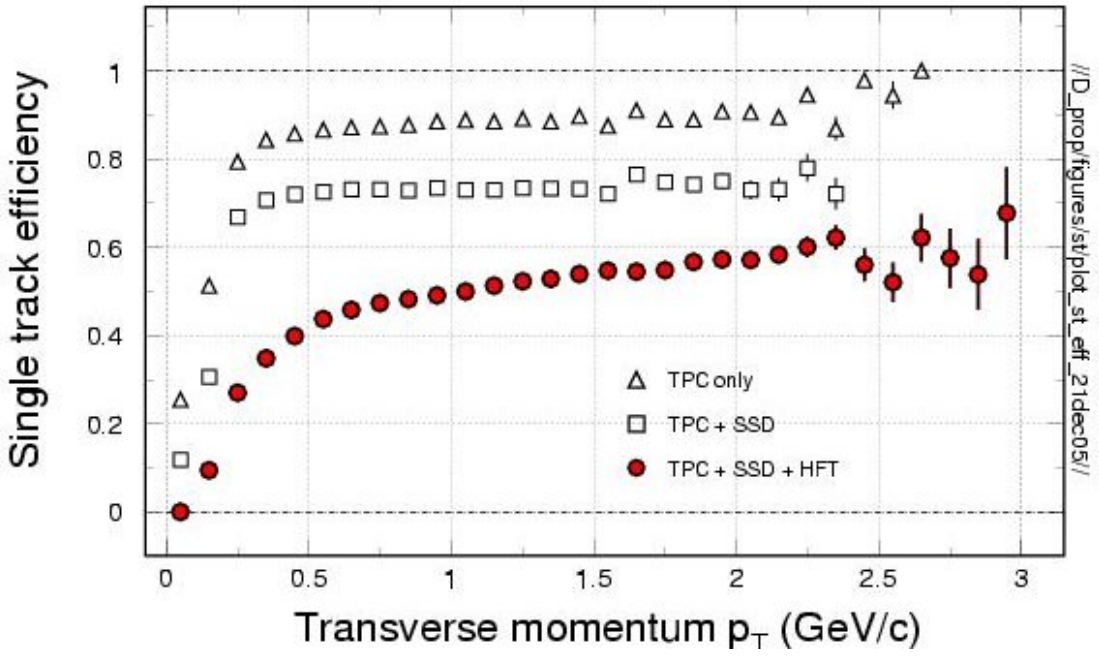

Figure 26: The efficiency for finding tracks in central Au + Au collisions in the STAR TPC, SSD, and the HFT. Accepted tracks have 15 TPC hits (or more), 1 SSD hit, and 2 HFT hits that match to a single Monte Carlo track. The quoted efficiency is for pions in the detectors acceptance; $|\eta| < 0.5$

3.6.3 Primary Track Reconstruction Performance

The performance of the HFT was simulated using tracks from central Au + Au collisions at $\sqrt{s_{NN}}$ = 200 GeV which were generated by the "MEVSIM" code and simulated using

single particle tracks. The simulated tracks and events were processed through GEANT and, finally, a detailed response function for the Time Projection chamber (TPC) and a response function for the Silicon Drift Detector (SSD) were applied to the data. These response functions take into account physical effects in the detector and the subsequent electronics. For the HFT, we smeared the Monte Carlo hits by a Gaussian function with a width of σ=6 μm in the x-y-plane and in the z-direction. The 4 ms read-out speed of the 1st generation HFT will lead to pile-up of 120 Au + Au collisions in the HFT at four times the RHIC design luminosity. We account for this by randomly uploading hits on top of the Monte Carlo generated hits in the HFT. The topic of pile-up is discussed in detail in Section 3.4

Tracks with at least 15 hits in the TPC, 1 hit in the SSD and 2 hits in the HFT detector were reconstructed with the STAR inner-tracker code. Figure 26 shows the efficiency for tracking pions with $|y| < 0.5$ in various detector configurations. The TPC results are designated by the open triangles, TPC + SSD by squares, and the TPC + SSD + HFT detector by filled dots (red). Note that the TPC tracking efficiency limits the efficiency of the SSD at low transverse momentum and, in addition, the efficiency of the HFT at low momentum is affected by ghost tracks and event pileup. But at high momentum, the acceptance of the detectors is quite uniform. Of the TPC and SSD tracks above 700 MeV/c traced to the HFT detector volume, about 70% have correctly matched HFT hits. The absolute efficiency for STAR tracking with the HFT (using the TPC, SSD and HFT) is 50% or above at a transverse momentum larger than 700 MeV/c. Simulations using mono-energetic pions show that the efficiency stays approximately constant up to 20 GeV/c.

In the high multiplicity environment of a central Au + Au collision, there can be ambiguities in finding the next hit on a track while following a track along its path. A ghost track is defined to be a reconstructed track with at least one hit from a different Monte Carlo track. With the present tracking algorithm, the number of ghost tracks in the TPC is less than 1% compared to all reconstructed tracks. The HFT is more restrictive, however, because it is continuously read out; events will pile up between successive reads of the Si chip, which occur every 4 ms.

Figure 27 shows the number of ghost tracks observed in the full HFT tracking system. At low momentum, ghost tracks dominate due to multiple Coulomb scattering. The bulk of the ghost tracks appear below 0.5 GeV/*c* and the effect of these miss-identified tracks can be seen in Figure 26 because the tracking efficiency for the HFT drops steeply below 0.5 GeV/*c*. The ratio of ghost tracks to good tracks is 20% at 0.5 GeV/*c* and saturates at 14% above 0.7 GeV/*c* (see the right hand panel of Figure 27).

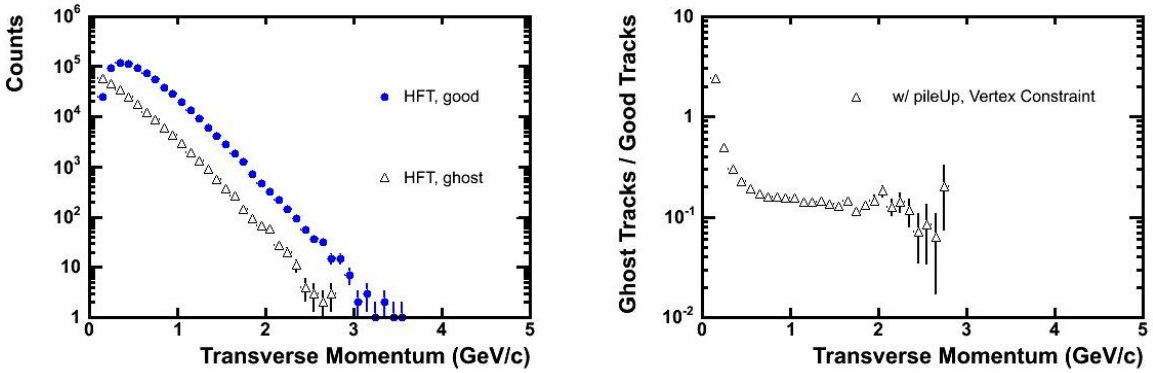

Figure 27: Reconstructed tracks with false HFT hits. Left – The number of ghost tracks and reconstructed tracks passing through the pixels of the HFT as a function of p_T. Right - The ratio of ghost tracks to good tracks. The increased ghosting rate at lower transverse momentum is a direct consequence of multiple Coulomb scattering, and is the motivating factor to make the detector as thin as possible.

3.7 Open Charm Reconstruction Simulation

As previously discussed, particles containing charm and beauty quarks are the probes relevant for the main thrust of our physics objectives. Charm and beauty quarks occur in a wide variety of hadrons, and these hadrons decay into a large number of different channels. To demonstrate the power of the HFT, we have simulated several specific charm meson decay channels, including $D^0 \rightarrow K^- \pi^+$ and $D_s^+ \rightarrow K^- \pi^+ K^+$, because of their large relative branching ratios. Table 9 displays some of the properties of these channels.

particle	Daughters	Cτ (μm)	Mass (GeV)
D^0	$K^-\pi^+$ (3.8%)	123	1.8646
$D^\pm$	$K^-\pi^+\pi^+$ (9.2%)	312	1.8694
D_s	$K^+K^-\pi^+$ (4.4%) $\pi^+\pi^+\pi^-$ (1.0%)	147	1.9683
Λ_c	$p K^-\pi^+$ (5.0%)	59.9	2.2849

Table 9: Open charm hadron properties

Signal and background events are generated separately. The signal consists of one D^0 or D_s^+ per event. The transverse momentum distribution of the charmed hadrons follows a Boltzman distribution which reproduces the $\langle p_T \rangle$ of D-mesons as measured by STAR in d + Au collisions at $\sqrt{s_{NN}}$ = 200 GeV and the rapidity distribution suggested by perturbative QCD calculations applying the program code Pythia[19]. The background is simulated using the MevSim event generator parameterized to reproduce the experimentally measured particle multiplicities in Au + Au collisions at $\sqrt{s_{NN}}$ = 200 GeV.

Our parameterization is accurate for particles below 3 GeV/c. It may underestimate the background above this momentum. The distributions of reconstructed D-meson signal and background were scaled to match the expected D-meson production per central Au + Au collision[44]. Also, the higher track reconstruction efficiency in single (D^0 signal) events compared to central Au +Au collisions (background) was taken into account.

Analysis of the reconstructed tracks to identify the 'signal' particle is done separately for the signal and background events. We use a direct reconstruction approach, where the daughter particles are identified as originating from a vertex displaced from the primary vertex. The invariant mass of the parent particle is then calculated from the kinematics of the daughters. This technique is superior to techniques depending on calculating all track combinations in an event both in signal to noise and analysis speed. The distributions from the analysis of signal and background events are then combined for the finished invariant mass distributions.

The heavy flavor tracker is designed to allow us to directly reconstruct mesons containing charm quarks. Thus we should see differences between the charm meson daughter tracks and the background and the primary tracks in several important variables. The distance of closest approach between the tracks and the vertex is an important example of this; see Figure 28. The distributions of reconstructed D^0 and D^+ daughters is compared to the primary track background. The charm meson tracks clearly have a broader distribution, driven by the decay length of the charm mesons. Cutting on the track DCA, then, will improve the signal to noise in the analyses.

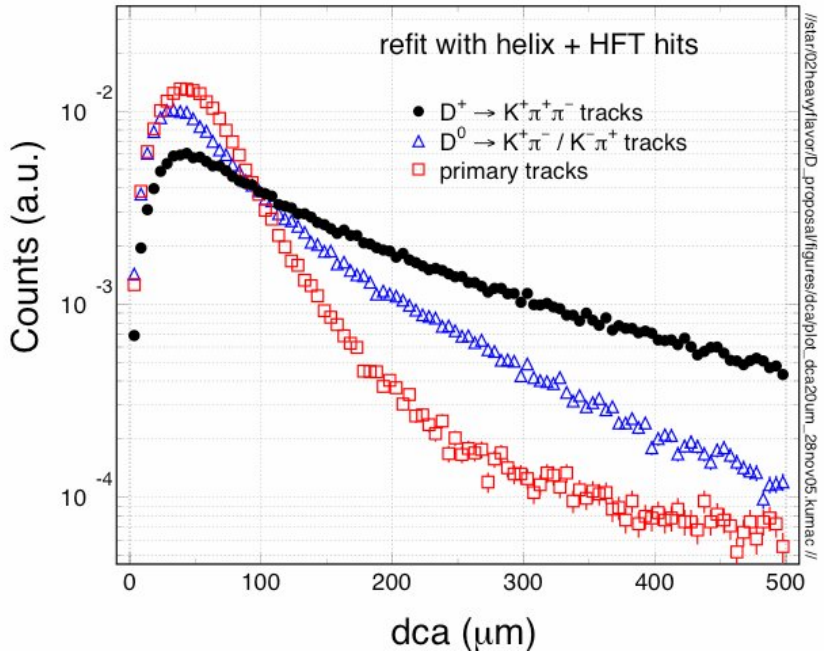

Figure 28: The distance of closest approach (dca) distributions for D^0 (triangles) and D^+ (circles). The results of the dca distribution for primary tracks are shown in squares.

3.7.1 D^0 reconstruction

The HFT detector allows us to identify a D^0 decay-vertex by reconstructing the trajectory of its two daughters. Figure 29 shows the topology of the decay.

The following selection criteria were used to separate the D^0 signal from background:

- The decay length *l*; with *l* the distance between the primary vertex and the D-meson vertex
- The difference, Δm, between the reconstructed invariant mass and the D^0 rest mass
- The distance of closest approach $DCA_{\pi K}$, between the two daughter tracks
- Isolation cuts on cos(θ), with θ being the angle between the D^0 momentum (vector sum of the two daughter momenta) and the vector joining the primary vertex to the D-meson decay vertex
- Isolation cuts on cos(θ*), with θ* being the angle between the kaon in the D-meson center of mass frame and the D-meson momentum

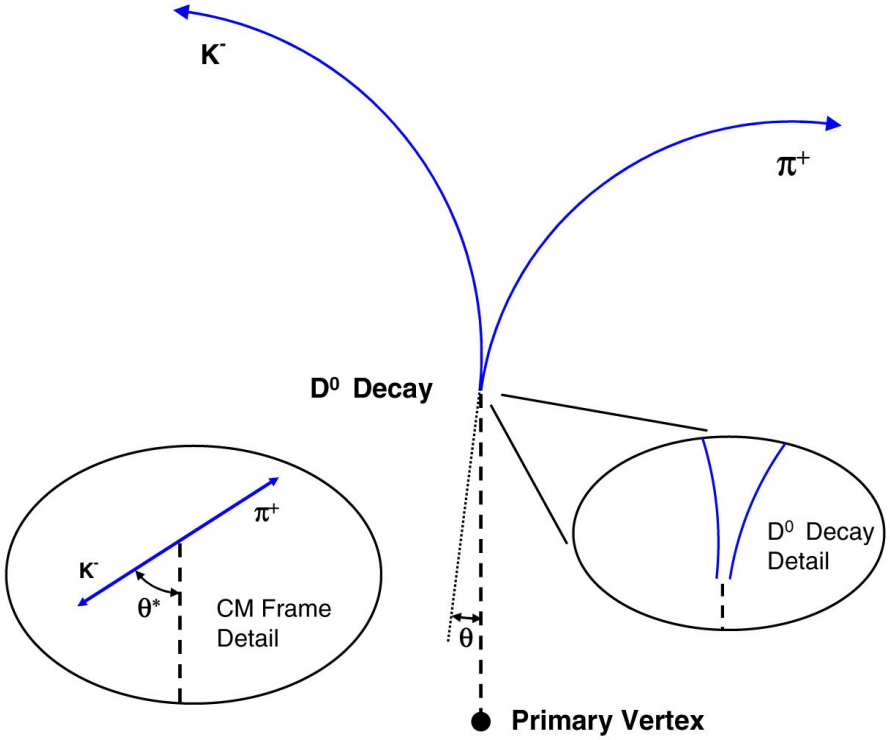

Figure 29: The decay topology for a D^0 decaying to a kaon and a pion. Isolation cuts to identify the D^0 from the background tracks are described in the text.

Charged decay daughters were identified by their specific energy loss in the TPC gas and the time of flight measured in the TOF. For example, to identify pions, we used a 3σ cut around the expected band for pions. The width of this distribution is momentum dependent, and was extracted from experimental data. With this method, pions can be

separated from kaons up to 700 MeV/c. The TOF detector extends this range up to 1.6 GeV/c, as demonstrated from existing STAR data with a small version of the full TOF detector. Tracks with a momentum above the range of these PID methods can still be used, but they must be entered into the reconstruction algorithm twice, once under a pion mass assumption, once assuming a kaon mass.

The selection of proper cuts is very important in order to reduce the background. The applied cuts for D^0 reconstruction were determined by using the program MINUIT. To achieve the best sensitivity, we selected the cuts to optimize the signal (D^0 yield, S) to noise (N) ratio = $S/\sqrt{(S+N)}$. See Table **10** for the values that were determined this way. Comparisons of signal and background distributions for various cut variables is shown in Figure 30 (and Figure 33 for the D^+), along with the final cut values. Figure 31 demonstrates that the significance, of course, depends critically on the proper choice of cuts.

Cuts	**D^0**	**D^+**
nFit >	15	15
$\|\eta\|$ <	1.0	1.0
HFT hits =	2	2
dca(global) ≥		100 μm
dca(V_0) ≤	35 μm	100 μm
decay length ≥	150 μm	150 μm
$\cos(\vartheta)$ >	0.996	0.85
Δm ≤	40 MeV	

Table 10: The cuts for the D0 and D+ reconstruction and efficiency analysis. The input D0 and D+ spectra followed an exponential distribution, <pt>=1.3 GeV/c.

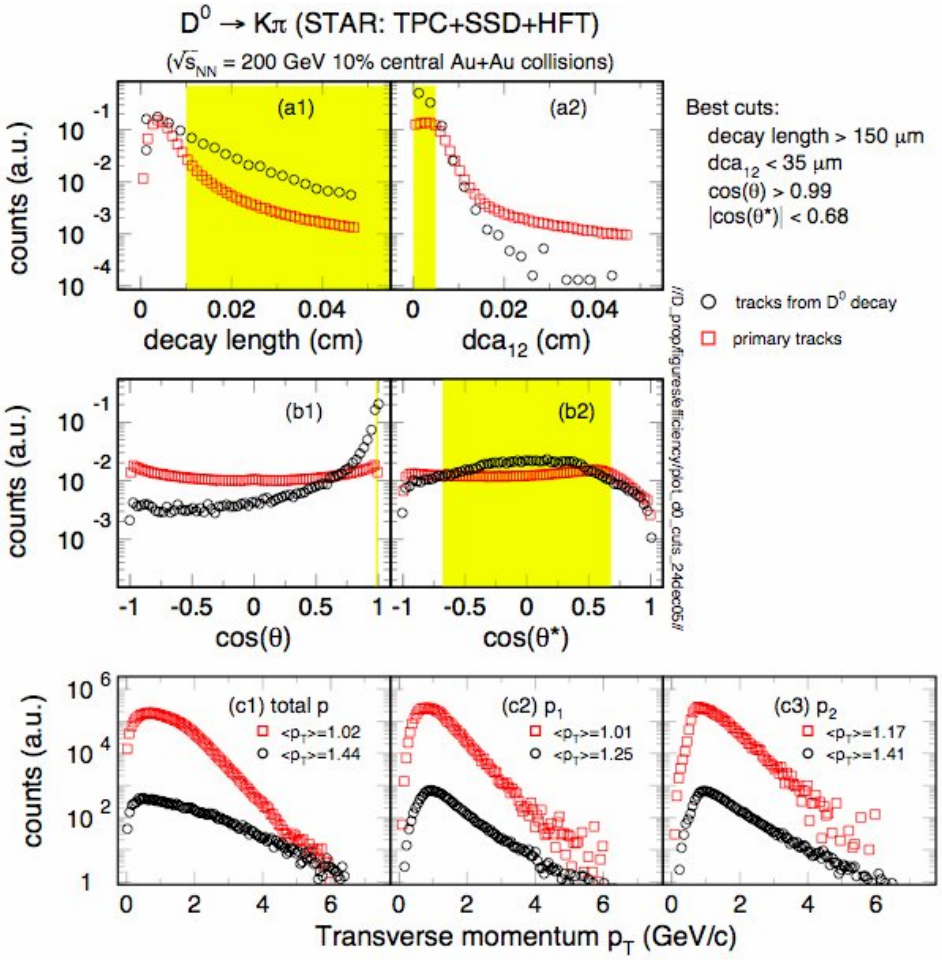

Figure 30: Distribution of quantities used to distinguish signal from background. Panels a1, a2, b1, and b2 compare the difference between background events and D0 mesons for different variables. The yellow shaded area shows the regions where we places cuts to enrich the D0 to background ratio. The lower panels, c1, c2, and c2, show the pt distribution for signal and background event tracks with a 100μm error vertex (c1), 20μm error vertex (c2), and perfect vertex (c3). Central Au + Au collisions are assumed for the background primary tracks.

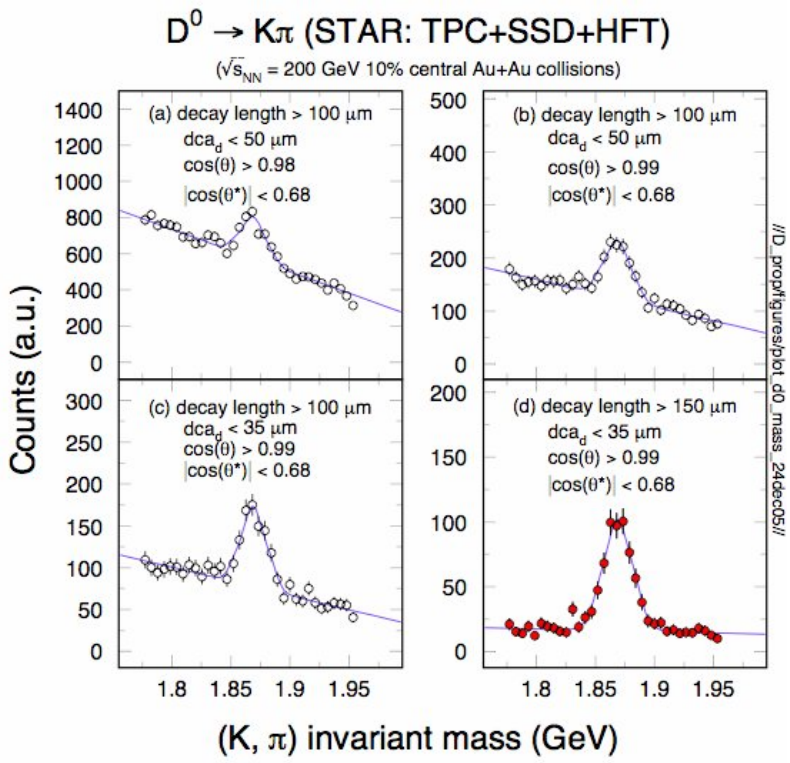

Figure 31: D^0 invariant mass with different cut sets. The power of the cuts to enhance the signal relative to the background is clear.

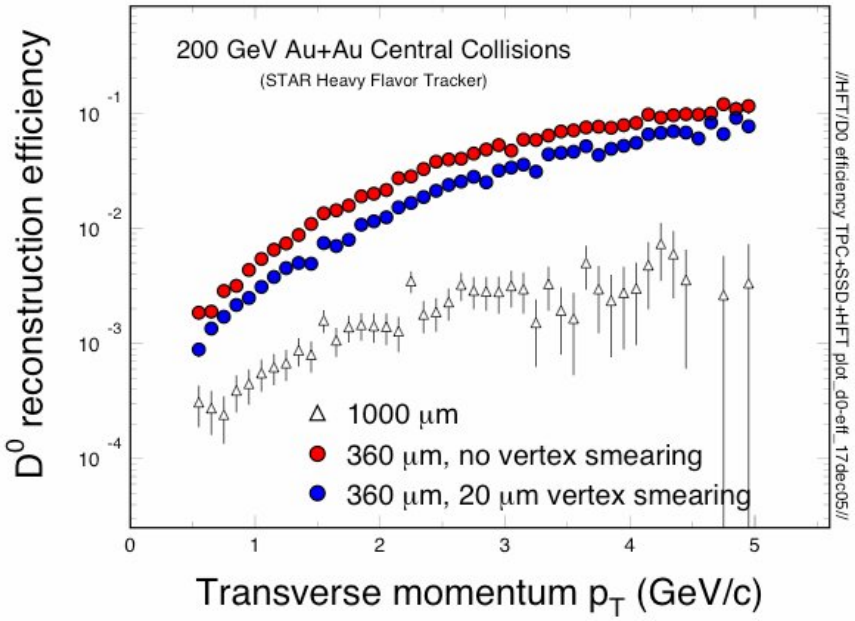

Figure 32: The absolute yield of D^0 into the TPC + SSD + HFT divided by the input D^0 yield. For comparison, a simulation with thick Si detectors that are similar to the wafers used in the ALICE vertex detector is also shown (1000 μm effective silicon thickness).

Once we have made these cuts, we can study the reconstruction efficiency. The overall efficiency takes into account acceptance, single track efficiency and D^0 reconstruction efficiency. We have studied the D^0 detection efficiency for three cases: knowledge of the exact location of the vertex, a vertex that is known to 20 μm, and an ALICE like detector. Figure 32 shows that the overall reconstruction efficiency increases with increasing momentum and saturates above 3 GeV/c at a value of about 10%. The efficiency of a 1000 μm detector is about an order of magnitude less.*

Since the single track efficiency of the HFT is 50%, the maximum D^0 reconstruction efficiency can be estimated to be 0.5×0.5 (tracks) = 25%, not taking into account the D^0 acceptance effects. This efficiency directly impacts the feasibility of a D^0 measurement for topics such as charm flow. Full estimates of the expected rate for detecting D^0's and the data needed to accomplish the flow measurement are detailed in section 3.8 In the next section, we will describe a related analysis; the reconstruction of the D^+ meson.

3.7.2 D^+ reconstruction

The dca-distribution, cos(θ), and decay-length distribution for both primary tracks (open-squares) and D+ decayed tracks are shown in Figure 33. Clearly the decayed tracks are well separated from the primary track. For D^+ reconstruction, a slightly different method was used compared to that of the D^0. The 'signal event' and 'background event' were mixed together. The distribution of the invariant mass from a K and two π tracks is then formed. The number of tracks used in the background events is consistent with the top 10% central Au + Au collisions at RHIC. The resulting invariant mass distributions for several p_T bins are shown in Figure 34. For the p_T bins studied so far, the significance $S/\sqrt{(S+B)}$ is better than 3.

---

* The results from a silicon sensor with the thickness used in the ALICE detector (3 times thicker than the STAR design) results in the D^0 reconstruction efficiency dropping by a factor 8, independent of momentum. To achieve the same statistical significance would then require an 8 times longer data taking period. As a result, we have excluded the ALICE detector technology from our design considerations.

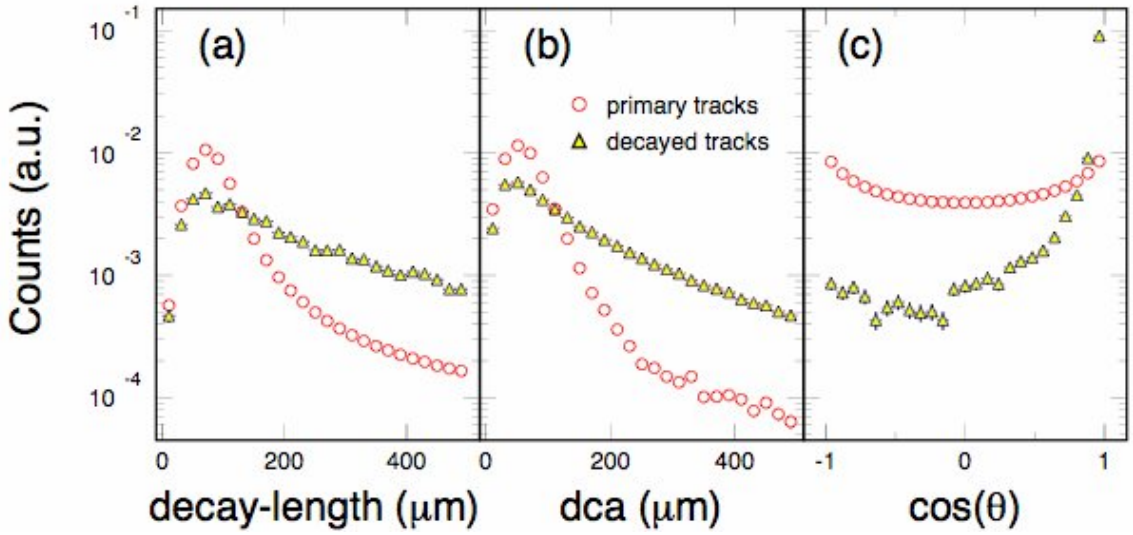

Figure 33: The D^+ decayed tracks decay-length, dca, and cos(θ) distributions (triangles). The same distributions for primary tracks are also shown (squares).

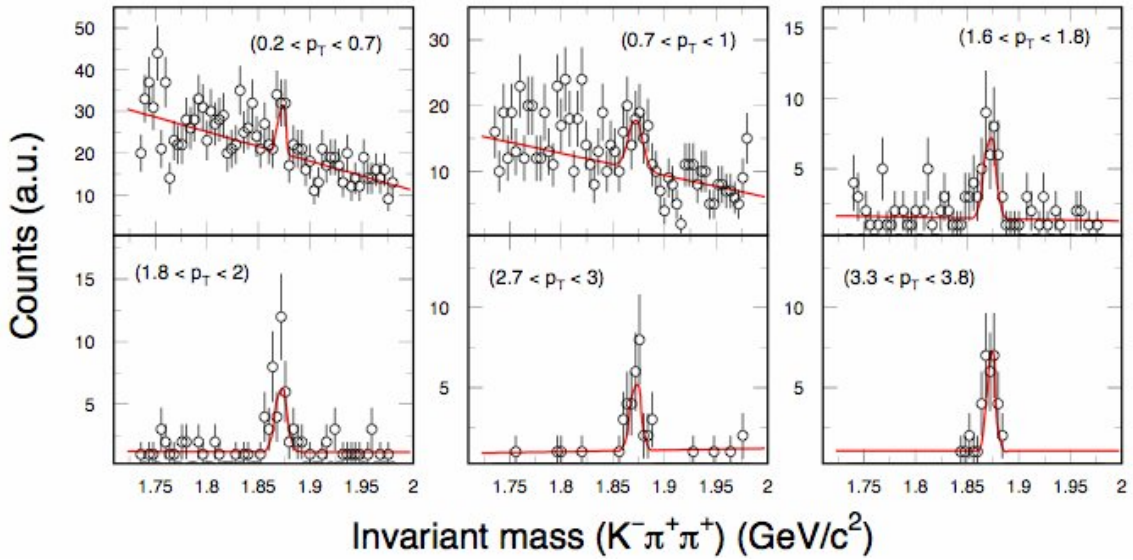

Figure 34: Invariant mass distributions for D^+ for several p_T windows. The lines are a polynomial (up to 2nd order) + Gaussian fit.

The final reconstruction efficiencies for D^0 and D^+ mesons are shown in Figure 35. Below $p_T \sim 0.5$ GeV/c for the Ds, the efficiency is very low since the slow charged daughter particles do not make it into the TPC. Above $p_T \sim 1$ GeV/c, both efficiencies increases as a function of the transverse momentum. The large difference between D^0 and D^+ efficiencies is caused by the topological cuts used for the reconstruction. Although the numbers are not yet fully optimized, these efficiencies are already usable for data analysis.

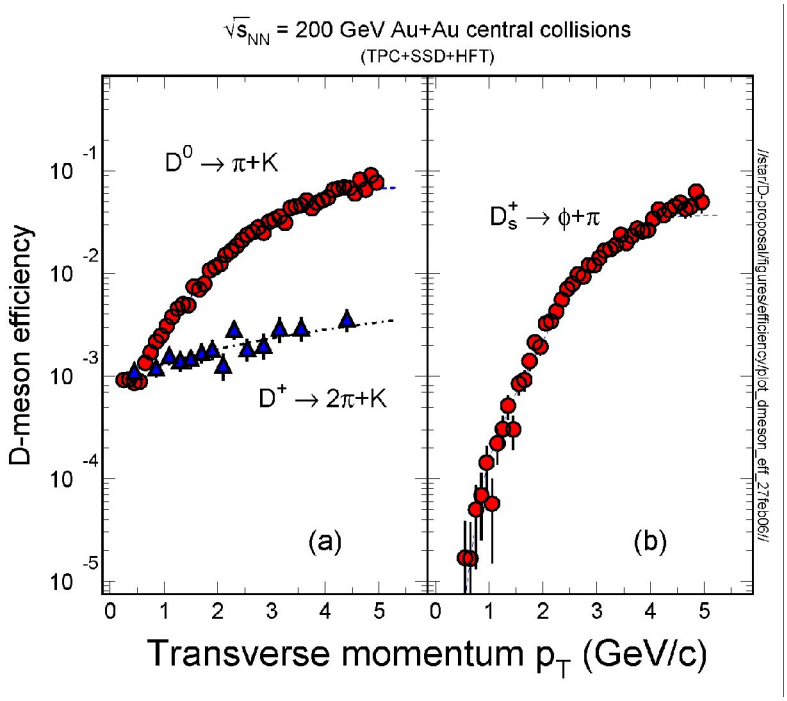

Figure 35: D-meson efficiencies as a function of transverse momentum, together with fits. to the distributions. The D^0 efficiency approaches 10%, while the D^+ efficiency approaches 3%.

3.8 Charm Elliptic Flow

As stated in Section 2, a measurement of charm elliptic flow is one of the main goals of the HFT. The measurement is necessary to understand the degree of thermalization in the partonic phase of a relativistic collision. To study the sensitivity of the HFT for such a measurement, we will focus on the capability of the HFT to measure the flow of D^0 mesons. The simulated D^0 transverse momentum distribution was generated from 200 GeV p + p collisions in Pythia[47]. The shape follows a power-law, and the integrated yield is fixed to the yield measured at mid-rapidity at RHIC[18], or dN/dy = 0.03 . The default value of dN/dy in Pythia is about a factor of 3 lower.

For the 10% most-central and 0-80% minimum bias Au + Au collision events, the number of binary collisions are 950 and 290, respectively[103]. The resulting distributions together with the efficiencies described previously are shown in Figure 36. The final measured particle yield versus p_T is also shown. Assuming 10% statistical errors in each p_T bin, the number of events required can be easily calculated, and the results are given in Table 11. At $p_T \sim 10$ GeV/c, a good R_{AA} measurement requires about 7.5 billion p + p events and 10 million Au + Au 10% central events. These numbers are achievable with the planned RHIC luminosity[104], 60% duty factor, and the current STAR detector system in a week of RHIC running.

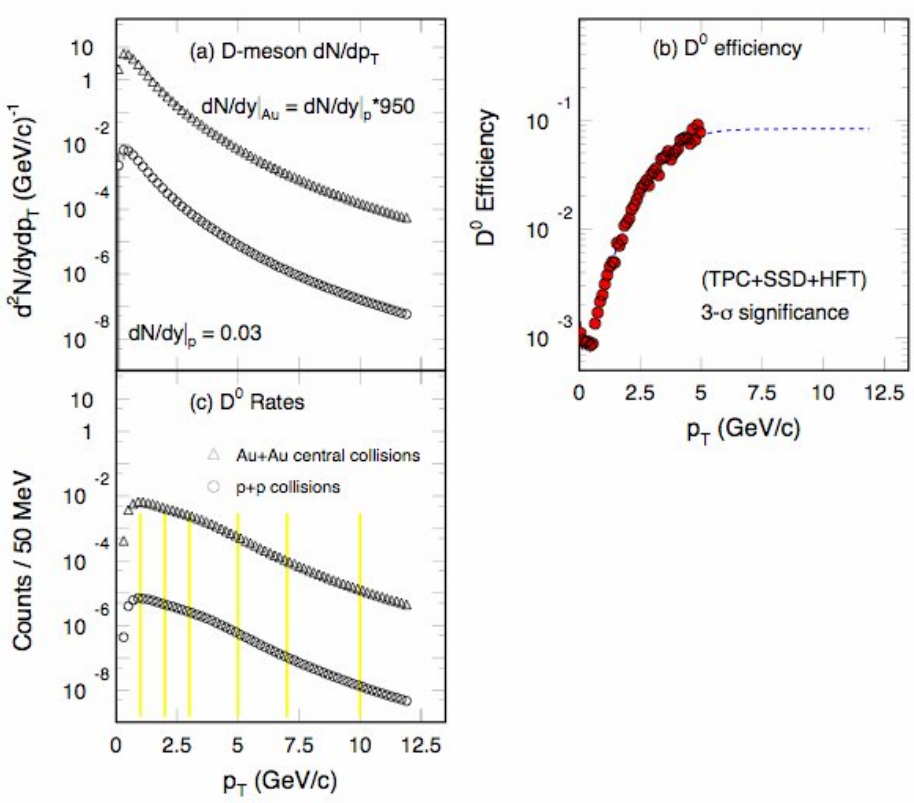

Figure 36: D-meson rates estimates: (a) dN/dp_T distributions for D-mesons. The integrated yield dN/dy = 0.03 as measured in p + p collisions at 200 GeV [Ref. 18]. The number of binary collisions (N_{bin}) = 950, corresponds to the top 10% most central Au + Au collisions at RHIC and is used to scale the Au + Au collisions; (b) 3-σ significance D^0 efficiency with TPC+SSD+HFT. The dashed-line is the fit to the simulation results; (c) D^0 meson rates from p + p and top 10% central Au + Au collisions at 200 GeV.

p_T (GeV/c)	Δp_T (GeV/c)	# of Events (p + p)	# of Events 0-10% Au + Au (N_{bin} = 950)	# of Events 0-80% Au + Au (N_{bin} = 290)
1.0	0.5	44×10^6	0.45×10^6	1.75×10^6
2.0	0.5	70×10^6	0.45×10^6	1.75×10^6
3.5	1.0	70×10^6	0.45×10^6	1.75×10^6
5.5	1.0	350×10^6	0.75×10^6	3×10^6
7.5	1.0	1200×10^6	3.5×10^6	11×10^6
10.5	1.5	7500×10^6	9×10^6	30×10^6

Table 11: An estimate of the number of events required to achieve 10% statistical errors for the spectra measurements of 200 GeV p + p collisions and 0-10%/ 0-80% Au + Au collisions. A power-law shape p_T distribution from the p + p collision has been assumed with the mid-rapidity dN/dy = 0.03 [Ref. 18]. The number of binary collisions is from Glauber calculations [Ref. 24].

In order to make a rate estimate relevant for the charm v_2 measurement, we need to make further assumptions about the p_T dependence of the anisotropy. Models of D^0 flow with and without charm flow[37], represent the extreme cases and thus the expected measurement range. The corresponding distributions are shown in Figure 37. In the same figure, the K_0 v_2 is shown as a line. With these assumptions and the known efficiency, the estimated rates per event can be estimated. Assuming the desired statistical uncertainties are less than 10%, the resulting required number of minimum bias events for the D^0 v_2 measurement is provided in Table 12 for various p_T bins. As one can see, with 500 million events, the D^0 v_2 (p_T) can be measured up to $p_T \sim 5$ GeV/c, using the proposed STAR HFT.

p_T (GeV/c)	Δp_T (GeV/c)	# of Events q_c does flow	# of Events q_c does not flow
0.6	0.2	260×10^6	525×10^6
1.0	0.5	70×10^6	140×10^6
2.0	0.5	53×10^6	125×10^6
3.0	1.0	105×10^6	175×10^6
5.0	1.0	210×10^6	440×10^6

Table 12: An estimate of the number events required for 10% statistical errors for D^0 v2 measurements of 200 GeV 0-80% Au + Au collisions (N_{bin}=290). A power-law shape p_T distribution from the p + p collision has been assumed with the mid-rapidity dN/dy = 0.03 [Ref. 18]. The number of binary collisions is from the GlauborGlauber calculations [Ref. 24].

As mentioned earlier, the assumptions in the model[37] are extreme limits. In order to test the thermodynamic behavior of the D-meson, the most important region is $p_T < 3$ GeV/c because at higher p_T, other dynamical effects will become important (e.g. jet correlations). The proposed STAR HFT detector will be able to make precise v_2 measurements in the transverse momentum region $0.7 < p_T < 3$ GeV/c. As we have done with the hadrons from the light-flavor sector[5], the combined analysis of the D-meson spectra, v_2 distributions and ratios will allow us to determine the charm quark collectivity and the thermodynamic nature of the medium created in heavy ion collisions at RHIC.

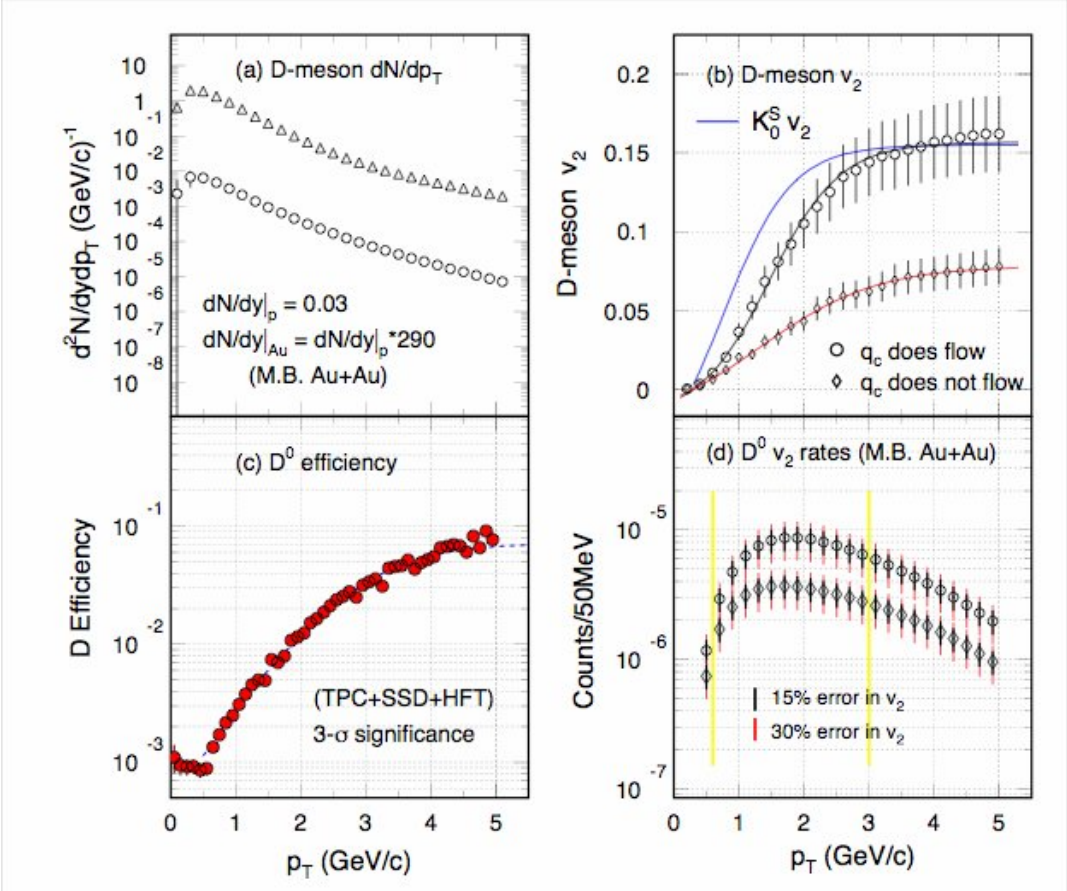

Figure 37: D-meson v_2 rate estimates: (a) dN/dp_T distributions for D-meson. The integrated yield dN/dy = 0.03 as measured in p + p collisions at 200 GeV [Ref. 18]. The number of binary collisions N_{bin} = 290, corresponding to the minimum bias Au + Au collisions, is used to scale the Au + Au collisions. A power-law shape from p + p collisions is assumed; (b) Assumed v_2 distributions for D-mesons. The solid-line is the results of fit to the measured Kaon v_2 [Ref. 24]. Both circle- and diamond-symbols are from [Ref. 47] for the case with and without charm quark flow, respectively. Error bars shown are from 15% systematic errors; (c) 3-σ significance D^0 efficiency with TPC+SSD+HFT. The Dashed-line is the fit to the simulated result; (d) D^0 meson v_2 rates from minimum bias Au + Au collisions at 200 GeV. The small and large error bars are for 15% and 30% systematic errors, respectively. For the v_2 analysis, 12 bins in φ are used.

3.9 Reconstruction of the Λ_c Baryon

The Λ_c is the lowest lying heavy flavored baryon. Roughly 10% of the charm quarks end up in the baryon sector[105] following a heavy ion collision. As has been mentioned in chapter 2, the measurement of the Λ_c is the best way for us to study heavy-flavored baryon/meson differences. It is important ingredient in our understanding of the hadro-chemistry and hadronization involving heavy-flavors. The branching ratio of Λ_c to the non-resonant decay is about 5% with a $c\tau$ = 60 μm. With a similar reconstruction algorithm used in the previous sections of this proposal, we have simulated the reconstruction efficiencies for Λ_c.

Plots (a), (b) and (c) in Figure 38 are the dca distributions (distance of closet approach of the Λ_c to the primary vertex), decay length (the distance from primary vertex to the decay vertex), and cos(θ) distributions (the angle between reconstructed Λ_c momentum vector and the direction of the primary vertex), respectively. (See Figure 29.) The red-lines in Figure 38 are for primary charged tracks and the circles are for tracks from Λ_c decay. The cuts on dca, decay length and cos(θ) are $35 < \text{dca} < 300$ μm, $50 < \text{decay length} < 350$ μm, and $\cos(\theta) > 0.92$. Plots (d) and (e) are the invariant mass plots in the momentum windows: $2.0 < p_T < 2.2$ GeV/c and $4 < p_T < 4.5$ GeV/c, respectively. The reconstructed efficiency is shown in plot (f). Additional work to further optimize the cuts, especially for the low pT region, is underway.

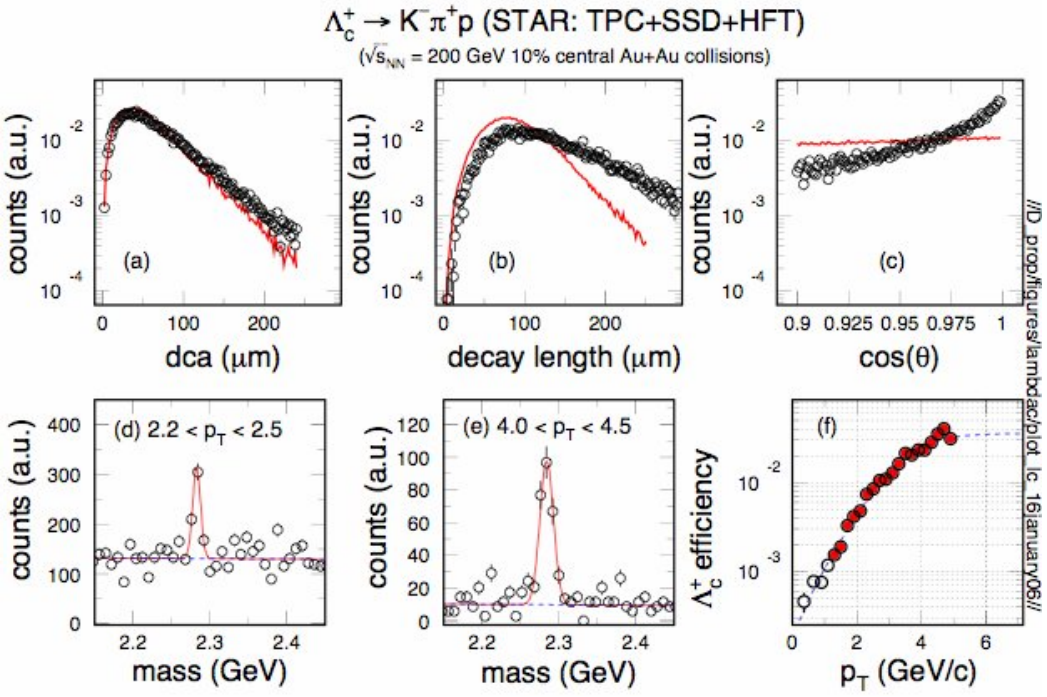

Figure 38: Λ_c decay length, dca, and invariant mass distributions.

In this study, an average of 0.8 Λ_c per event was used. Below $p_T < 2$ GeV/c, the signal over background ratio S/(S+B) is less than 3. 50 M central events (top 10%) are needed in order to measure a Λ_c p_T distribution from 200 GeV Au+Au collisions. Assuming binary scattering scaling for the heavy flavor production at 200 GeV, we find that 1000 M peripheral events (60-80%) will be required to measure the nuclear modification factor $R_{AA}(p_T)$ with an error of about 20% up to $p_T \sim 5$ GeV/c. This can then be used to compare with other heavy-flavor mesons and light-flavor hadrons.

4 Pixel Detector (PIXEL)

4.1 Introduction

The STAR heavy flavor physics program requires a thin, fast, detector that can operate in a relatively high radiation environment. A precision flow measurement requires to determine transverse momenta down to 150 MeV/c. To reach this low threshold requires a very thin pixel detector in order to maintain precise tracking without degradation by multiple Coulomb scattering. It is difficult to meet all of these requirements using the "usual" techniques currently employed in high energy physics experiments.

The emergence of CMOS sensor technology offers a new perspective on high precision charged particle tracking and vertex finding. This technology can provide the performance parameters required by the PIXEL. Recent developments have shown that CMOS technology is capable of excellent spatial resolution and charge collection efficiency, together with satisfactory radiation tolerance.

4.1.1 Choice of technology

We have evaluated the available technologies in detail. At this time, there are four good technologies that can be used for a thin vertex detectors: Charge Coupled Devices (CCD), Active Pixel Sensors (APS), Hybrid Pixels, and DEPleted Field Effect Transistor structure (DEPFET). Each of these devices has strengths and weaknesses. In the process of preparing this proposal, we have evaluated each and selected APS as our choice for the PIXEL detector.

CCDs

At SLAC, the SLD collaboration built and successfully operated a pixel vertex detector[106], VXD3, based on CCD technology.[107] But since silicon is damaged by radiation and CCDs require that the charge be transferred from one pixel to another, CCDs are more susceptible to radiation than other vertex devices. Charge in the end row of a CCD chip, for example a 1000 × 1000 array, must be transferred through more than 1000 pixels before being digitized. Therefore, any small loss in charge transfer produces large signal losses and signal sharing. The SLD vertex detector ran at a relatively low radiation intensity because that is the nature of the SLAC Linear electron Collider (SLC), so the SLC CCD could tolerate the radiation environment. In addition, the complexity of the clocking makes the readout slow. This was suitable for the SLC where it only had to be operated at 2 Hz.

CCDs require significant power to clock the charge around the chip because high capacitance electrode structures covering the whole chip must be voltage switched. This becomes a power versus speed trade off with consequences in the mass budget because

liquid cooling is usually required. In any case, cooling is a complication for CCD operation. For instance, VXD3 used LN_2 gas to cool the device but because the ladders were operated far below room temperature, elaborate mechanical and alignment systems were needed to achieve the excellent resolution of about 30 μm for determining the impact parameter. An outer heated jacket was needed to prevent condensation and the cooling system added extra complications and created additional mass.

Finally, to fabricate CCDs requires specialized knowledge, is expensive, and requires a long learning curve to become familiar with its details. Currently, there is a group studying whether the limitations of the process can be overcome to use this technology at a future electron collider.[108]

Hybrid Pixels

At the Large Hadron Collider (LHC)[109] the three major experiments decided to use a hybrid technology where the sensor is bump bonded to a read-out chip. The hybrid technology has the disadvantage that the pixel size is much greater than a CCD pixel and two chips have to be layered on top of each other. The two chips and their interconnection are much thicker than can be done in CCD technology.

DEPFET

The Munich MPI Semicondcutor Laboratory has recently invented[110] and continues to be the leader in the use of DEPFETs.[111] This concept is based on the combination of the sideward depletion, as used in a semiconductor drift detector with a field effect transistor to collect the charge. The MPI Group has a conceptual design for a detector for the Linear Collider but much development is needed to make a realistic device. DEPFETs require a very special process and MPI is the only producer of this device so any development must be done within that institute.

Active Pixel Sensors

APS devices have been used as photon detectors since late 1960s.[112] They have recently surpassed CCDs in the photography market because of their lower cost and lower demand for power. Power consumption is important in a particle detector application because a detector that can be air cooled is overall thinner than a detector that requires water cooling. The CNRS group in Strasbourg France has done a great deal of research on these detectors; taking them from small prototypes to large arrays of successful detector elements. Table 13 presents a detailed listing of the CMOS sensor program.

APS technology is our preferred technology for the PIXEL and we are working with the Strasbourg group to design and utilize this technology in our detector. The APS technology will be described in more detail in the next section.

Chip	Year	Process (µm)	Epi. (µm)	Pitch (µm)	Pixels	Comments
MIMOSA-1	1999	AMS 0.6	14	20	4k	thick epitaxial layer
MIMOSA-2	2000	MIETEC 0.35	4.2	20	4k	thin epitaxial layer
MIMOSA-3	2001	IBM 0.25	2	8	32k	deep sub-mm
MIMOSA-4	2001	AMS 0.35	no	20	4k	low dopant substrate
MIMOSA-5	2001	AMS 0.6	14	17	1M	real scale 1M pixels
MIMOSA-6	2002	AMIS 0.35	4.2	28	3k	fast column parallel readout internal data sparsification
MIMOSA-7	2003	AMS 0.35	no	25	1k	fast column parallel readout internal data sparsification. (photoFET)
MIMOSA-8	2003	TSMC 0.25	~8	25	4k	fast column parallel readout internal data sparsificaton
MIMOSA-9	2004	AMS 0.35 opto	~14	20 30 40	7k	tests diodes/pitch/leakage current
MIMOSA-9 (no epi)	2004	AMS 0.35 opto	no	20 30 40	7k	tests diodes/pitch/leakage current
MIMOSA-10 (MIMOSTAR-1)	2004	TSMC 0.25	~8	30	16k	first prototype for STAR PIXEL
MIMOSA-11	2005	AMS 0.35 opto	~14	30	7k	radiation tolerant structure
MIMOSA-12 (Mosaic 1)	2005	AMS 0.35 high resistive	no	35	0.6k	multi-memory pixels (FAPS)
MIMOSA-13 (Mosaic 2)	2005	AMS 0.35 high resistive	no	20	1.4k	fast column readout
MIMOSA-14 (MIMOSTAR-2)	2005	AMS 0.35 opto	no	30	16k	second prototype STAR PIXEL
MIMOSA15	2005	AMS 0.35 opto	~14	20 30	7k	multi-purpose tracker-imager
SUC 1	2003	AMIS 0.35	4.2	25 35	4k	radiation tolerant structure (SUCIMA project)
SUC 2	2003	AMS 0.35	no	40	2k	low dopant substrate (SUCIMA project)
SUC 3	2003	AMIS 0.35	4.2	20	8k	radiation tolerant structure (SUCIMA project)
SUC 4 Mtera	2004	AMS 0.35	14	150	12.5k	Hadron therapy/beam monitor. (SUCIMA project)
SUC 5	2004	AMIS 0.35	4.2	30	65k	proton dosimetry (SUCIMA project)

Table 13: Table – Chart of APS chips that the CNRS group has produced in the past 5 years [113].

4.2 Main Features and Performance of CMOS Active Pixel Sensors

CMOS sensors are manufactured using industry-standard CMOS technology. This offers low fabrication costs and fast turn-around times in their development. The key element of this technology, for our purposes, is the use of an n-well/p-epi diode to collect the charge, through thermal diffusion, which is generated by the impinging particles in the thin epitaxial layer underneath the read-out electronics,[114] schematically shown in Figure 39. An attractive feature of these sensors is that they allow fabrication of System-on-Chips (SoC) by integrating signal processing micro-circuits (amplification, pedestal correction, digitization, discrimination, etc.) on the detector substrate. Moreover, a CMOS substrate can be thinned down to a few tens of microns because the active region is less than 20 μm thick.

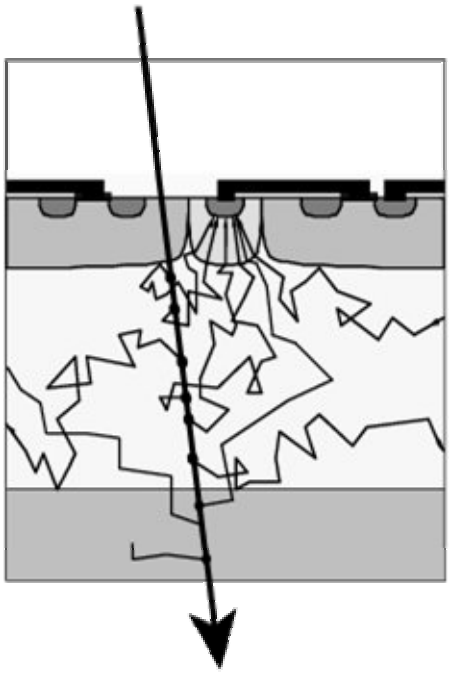

Figure 39: Epitaxial Silicon used as a sensor. In this design, a primary ionizing particle creates free charges in the epitaxialy grown Si layer that is a few tens of microns thick and a few electrons in the bulk layers. The liberated charges are then free to diffuse towards a potential well structure at the top of the sensor where they are extracted and read out into a DAQ system.

The ability of these sensors to provide charged particle tracking is now well established.[115] The CNRS group, at Strasbourg, has built a series of these sensors, which they called MIMOSA.[116] Similarly, the LBNL/UCI group has also built and successfully tested these sensors. The MIMOSA line of detectors has explored different CMOS fabrication processes and key parameters of the charge sensing system, and the results demonstrate that a detection efficiency of ~ 99% and a single point resolution of ~2 μm can be achieved using a pixel pitch of 20 μm. The prototypes also show that digitizing the charge with a small number of ADC bits does not degrade the resolution significantly (the measured reduction was ~ 2.5–3 μm) while the double hit resolution is ~ 30 μm.

The radiation tolerance of the sensors to bulk damage[117] was also investigated. No significant performance loss was observed up to fluences close to 10^{12} n_{eq} cm^{-2}. As far as

ionizing radiation damage is concerned, the real potential of this technology is still being explored, but it is already established that it stands up to more than 100 kRad.

Most of the R&D at CNRS was performed with small prototypes (a few mm^2) containing a few thousand pixels. Figure 40 shows a full size prototype (i.e. ~3.5 cm^2) called MIMOSA-5. It is composed of ~ 1 million pixels per chip, and it was fabricated on a 6 inch wafer, as shown in the figure. The wafers were thinned down to 120 μm before the chip was cut and diced into individual, reticle sized, detector elements.

Tests at the CERN-SPS confirmed that MIMOSA-5 performed as well as the smaller prototypes: a 99% detection efficiency was observed with ~ 2 μm single point resolution. The prototypes were operated with a read-out time of 25 ms, which was limited by the maximum operation frequency of the read-out board (i.e. 10 MHz). The chip was actually designed for a 4 times faster read-out speed. The LBNL group has tested several of these chips at the LBNL ALS and has measured the expected Landau spectrum on each.

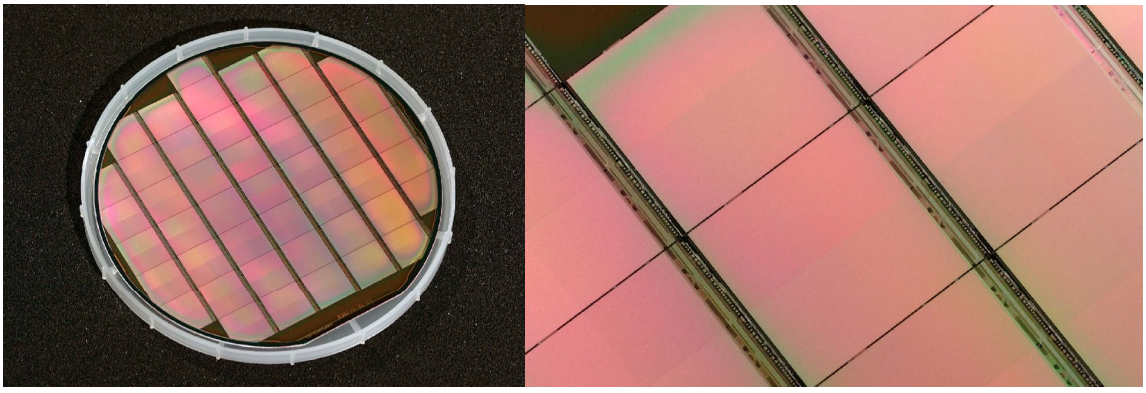

Figure 40: Wafer of reticle size sensors (left) and zoomed-in view of individual chips (right).

After MIMOSTAR-5, several fabrication processes were explored, aiming to find the process providing the smallest leakage current. In general, several parameters underlying the sensor performance depend on features specific to each fabrication process and so the process specific characteristics need to be explored in parallel with the development of the chip architecture.

For instance, a new fabrication technology, relying on a lightly doped substrate but exhibiting no epitaxial layer was investigated with two different prototypes chips. Further CNRS tests show that a detection efficiency of 99.9% can be achieved with this technology, as well as a single point resolution of about 2.5 μm[118]. A major advantage of this technology is that a large signal can be generated because the charges are collected from several tens of microns of Si instead of from ~ 10 μm in an epitaxial layer. The extra charge makes it well suited to applications with substantial electronic noise.

4.3 Thinning

Up to now, tested MIMOSA-5 chips have been thinned down to 120 μm thickness. This operation was successful and we have not found any degradation of the sensor parameters.

In the PIXEL, the MIMOSTAR thickness will be 50 μm. Thinning a 6 or 8 inch wafer down to this thickness is not expected to be a problem, since the process is an industry standard technique. We have demonstrated that 50 μm sensors are mechanically stable and can be assembled into ladders. We have used low-yield MIMOSA-5 wafers to make these investigations and have successfully thinned detectors to 50 μm.[119] Our colleagues at the LBNL light source (ALS) have just characterized several MIMOSA-5 chips in the 1.5 GeV/c electron beam and have subsequently thinned them. Tests of the thinned chips are completed and we find no degradation of signal from thinned chips.

4.4 Additional R&D

CMOS sensors have been developed in Strasbourg since 1999 for various applications, which range from vertex detectors for subatomic physics, to bio-medical imaging (e.g. beam monitoring for oncotherapy, dosimeters for brachyotherapy) and operational dosimetry (e.g. control of ambient radon and neutron radiation levels in nuclear plants).

Several application domains call for SoCs providing fast read-out speed (meaning signal treatment and data flow reduction integrated on the chip), high radiation tolerance, minimal material budget and low power dissipation. Developments for the STAR upgrade will thus benefit from the synergy with the R&D for other applications, in terms of fabrication process exploration, development of fast signal processing architectures, radiation tolerance investigations, and other improvements. More information on the activities and achievements of the Strasbourg research team are available in Ref. [120].

Starting with a CNRS design, the LBNL/UCI group has built several generations of APS sensors. These devices were built in the 0.25 μm process at TSMC. These ICs have been tested using different sources, i.e. ^{55}Fe, 1.5 GeV accelerator electrons and a scanning electron microscope. Figure 41 shows one of the sensors that has 16 different test structures.

Our measurements have confirmed the CNRS results that APS sensors can measure charged particles with excellent spatial resolution.[121,122] Figure 42 shows several 1.5 GeV electrons recorded at LBNL's Advanced Light Source.

To study the effects of radiation, we have exposed the chips to protons at LBNL's 88" Cyclotron. Afterwards, we measured the change in leakage current and pulse height. These results show that there was a modest change with an irradiation of 300 krad. What was most interesting is that after 6 months the device self annealed. Therefore, the effect

of gradual radiation is much less than that of an acute exposure.[123] These radiation measurements are complementary to the neutron exposures studied by the CNRS group.

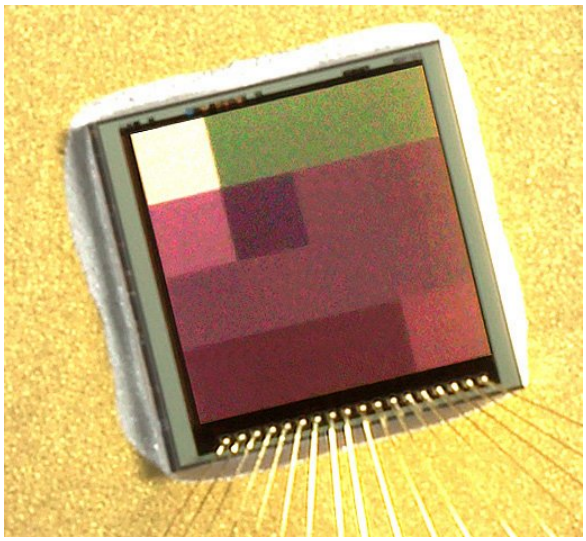

Figure 41: An APS Sensors developed by the LBNL/UIC group. The picture shows 16 separate test structures. Each structure has a 36 × 36 array of 20 μm pixels.

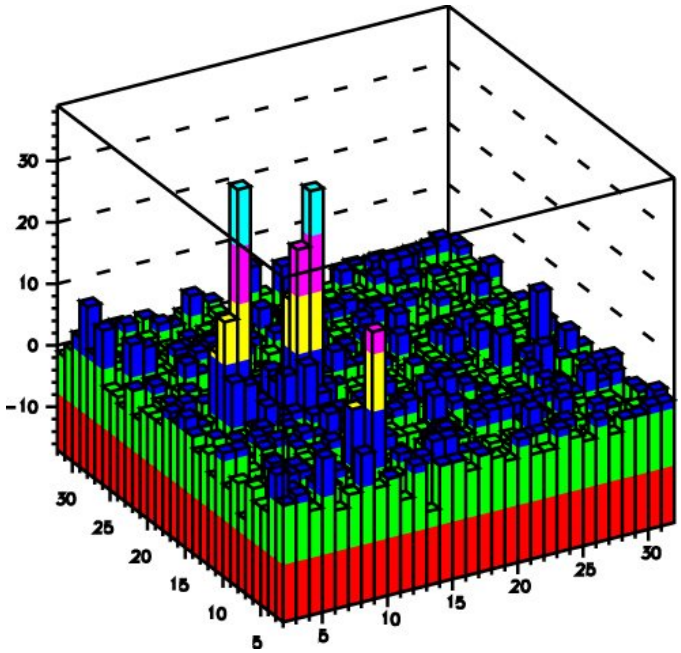

Figure 42: This graph shows the results of one event taken with 1.5 GeV electrons. Each bin represents one pixel and the height is proportional to the measured charge. Several electron hits can be identified in the plot.

We also completed a study on the effects of varying the pixel pitch. We built and tested a sensor with 5, 10, 20 and 30 μm spacing. Our tests show that to first order the charge

collection was identical when comparing the central pixel to the charge collected on its neighbors.[124] As the pixel spacing decreases, more total charge is collected. This observation can be explained by the fact that as pixel spacing becomes smaller, the charge is collected by the diode faster, so there is less time for it to recombine. This result implies that we can easily extrapolate our measurements at 20 μm spacing to the selected spacing of 30 μm for MIMOSTAR.

We have been looking at several other techniques to improve APS sensors. It is clearly desirable to speed up the readout as well as reduce the signal spreading to multiple pixel diodes. Concentrating the signal onto a single diode would improve signal to noise.

We can increase the fraction of charge collected by a single pixel using the photo-gate technology. In principle, this technology allows us to use a large area photo-gate for charge collection, without increasing the capacitance, because the charge is transferred from the photogate region to a low capacitance diode. Even though we have demonstrated the sensitivity of the photo-gate structure to X-rays, we have not achieved the expected performance of the device. The transfer time required for moving electrons from the photo-gate to the drain appears to be very long (several ms). We believe this undesirable signal delay is consistent with surface traps at the $Si0_2$ silicon boundary. Studies to find a way to avoid this delay have been studies in a SBIR proposal.

Correlated double sampling (CDS) is a standard technique that is used to remove the fixed pattern noise and KTC noise introduced by the reset transistor. Its main drawback is the required read out and storage of a full frame of data. To avoid doing CDS, we have produced a clamp circuit[125] that reduces the reset noise by a factor of 3**.**

Two generations of "active reset chips" have been fabricated and tested. In this approach the pixel voltage is reset to the empty level with a feed back amplifier potentially reducing fixed pattern noise and the KTC noise associated with a passive reset switch. Preliminary testing shows some noise reduction, but not the full potential improvement. We will be making some changes to this circuit and fabricating this in a new sensor design.

To explore how charge is collected on a sensor as a function of position, we tested a device at LBNL's National Center for Electron Microscopy. Using the scanning electron microscope, we have been able to position the beam on a pixel with precision of about 1 μm. This allows us to explore algorithms for determining the position of an incoming particle by relating how charge is shared among neighboring pixels. The results show that we can easily obtain the position of the incoming electron by weighting the charge collected from nearby pixels.

We have also been collaborating with colleagues at UC San Diego on the suitability of using an APS sensor in an electron microscope[126]. We have been studying the response

of electrons from energies of 100 keV to 300 keV. Results show that single electrons can be detected with a good signal to noise ratio. This technique is well suited for this application as it overcomes problems for traditional CCDs that suffer radiation damage. Excellent pictures of proteins have been taken. Using APS devices is very appealing for this different types of application.

We continue to try to further improve the devices. We have fabricated a sensor with different diode sizes. We have used this device to understand the effect of diode size on signal to noise. The results show that the smallest diode that meets the design rules produces the best signal to noise.

Recently, we submitted an IC design without an epi-layer. We have received the sensor and in the process of testing it. Simulations show that we should be able to collect more charge from the process.

In addition, we are studying ways to reduce the sampling time. In the current MIMOSTAR design, the sensor is always sensitive to radiation. We will study a sample-and-hold circuit to see if we can reduce the time window during which the detector is sensitive. If we could gate such a sensor, then pile-up effects of out of time interactions would be significantly reduced.

4.5 MIMOSTAR Sensor Design

Based on our experience with CMOS technology, a new series of chips, MIMOSTAR, have been fabricated. The first chip in the series is also called MIMOSA-10, which indicates its place in the evolution tree of CMOS sensors. Its most significant design parameters are:

- Pixel pitch: 30 μm
- Passive forward bias diode in place of reset switch
- Additional details can be found in Ref. [127].

The goal of the MIMOSTAR series is to provide for a full-scale prototype that is suitable for evaluating the performance of a CMOS sensor in a collider environment.

Since the read-out speed requirement for this prototype is modest, the chip's architecture is based on relatively slow signal processing at the pixel level. This low speed requirement enables us to quickly implement this sensor, while at the same time we are independently developing a sensor that fulfills STAR's requirements. Its design favors moderately low noise and modest power consumption. On the other hand, high speed signal processing is needed at the chip level (i.e. after amplification and multiplexing) due to the need for short integration times and limited shot noise.

The chip includes JTAG based remote control functionality (e.g. bias setting, test settings, etc.). The power dissipation of this architecture is estimated to be slightly more than 50 mW (i.e. less than 15 mW/cm^2), which can easily be cooled with air.

The CNRS group has studied MIMOSTAR-1, which was fabricated in the TSMC 0.25 μm process. They showed that the conventional controls work (via the JTAG controller), and that the bias circuits work and exhibit linear response via their DACs. The analog performance of the chips has been tested and the gain on the pre-amplifiers was about 3.5 at the two 10 MHz outputs. However, due to the inherent properties of the TSMC process, the charge collected on the n-diode could not hold the collected charge long enough for it to be read out. Our group at Berkeley Lab observed a similar effect with another chip designed in collaboration with UCI, which also was fabricated in the TSMC 0.25 process.

Consequently, we decided to switch to the AMS 0.35 OPTO process, in which the passive forward bias diode reset circuit has already been demonstrated to work. A new chip, MIMOSTAR-2, has been fabricated, passed ^{55}Fe tests, and then tested in DESY's 5 GeV electron beam. A radiation tolerant design and a standard design showed efficiency greater than 99.7% at a temperature of 40 C. The radiation tolerant design showed a very small increase in noise at 40 C when it was exposed to 23 kRad of ^{60}Co.

4.6 The Path to a CMOS Pixel Detector

With this research and development done at CNRS and LBNL, we are confident that we can build a CMOS sensor appropriate for RHIC II luminosities. To achieve this goal, we have identified a series of steps that must be taken before we can design and build the final PIXEL sensor. In the next subsections, we will describe the different R & D steps necessary to achieve this ultimate goal.

4.6.1 MIMOSTAR-3 – a Half Sized Chip

MIMOSTAR-3, which is half the size of the final sensor, continues the work done on MIMOSTAR-2. It is made up of 640 × 320 pixels. The fabrication will rely on an engineering run in AMS 0.35 OPTO technology. The chip has two analog outputs implemented on the same side of the sensor. Each output runs in parallel at 50 MHz so the total time for readout is 2 ms.

Once these chips have been tested, they will be incorporated on a ladder for a full function test in STAR. As a ladder will be half the final size, significant tests will be able to be done.

4.6.2 MIMOSTAR-4 – a Full Sized Chip

Using the experience gained from building and testing MIMOSTAR-3, we will design and manufacture a full sized sensor that can both be used in a full sized ladder prototype. This chip will be twice the size of MIMOSTAR-3, so it will be 640 × 640 pixels. It will have 2 analog outputs on one side running at the same speed of MIMOSTAR-3, so it will take 4 ms to read out all of the pixels. The fabrication of this chip will be done in a production run.

Table 14 shows how the measured performance of the MIMOSA-5 sensor compares to the specifications of MIMOSTAR-4. Most of the requirements (granularity, radiation tolerance, thinning, read-out speed, power dissipation, and sensor size) have already been demonstrated with MIMOSA-5. Some effort is still needed to achieve a higher read-out speed and higher yield during thinning. Moreover, since the sensors will be operated at room temperature, special attention will be given to the magnitude of the leakage current in order to keep the corresponding shot noise at an acceptable level.

Parameter	MIMOSTAR-4 specifications	MIMOSA-5 performance
Detection efficiency	> 98% at 30 – 40° C	~99% ≤ 20° C
Single point resolution	< 10 μm	~2 μm
Granularity (pixel pitch)	30 μm	17 μm
Read-out time	4 ms	24 ms (< 20 ms possible)
Ionizing radiation tolerance	3.7. kRad/yr[†]	> 100 kRad
Fluence tolerance	2×10^{10} n_{eq}/cm^2	$\leq 10^{12}$ n_{eq}/cm^2
Power dissipation	< 100 mW/cm^2	~10 mW/cm^2
Chip size	~2 × 2 cm^2	1.9 × 1.7 cm^2
Chip thickness	~50 μm	120 μm

Table 14: Comparison between MIMOSA-5 characteristics and MIMOSTAR-4 specifications.

4.6.3 The Ultimate sensor

A next generation CMOS IC is needed to meet the requirements of the high intensity at RHIC II. At these higher luminosities, we need to read-out the chip to match the 1 ms readout time of the TPC and to have the chip sensitive for a much shorter time to reduce

[†] Estimate based on RHIC achieving an average Au + Au luminosity of 1.0×10^{27} cm^{-2}s^{-1} for 21 weeks at 60% efficiency. T. Roser, W. Fischer, A. Drees, H. Huang, V. Ptitsyn, "RHIC Collider Projections (FY2006-FY2008). July 19, 2005. http://www.agsrhichome.bnl.gov/AP/RHIC2004/RhicProjections.pdf

the effect of pileup. The goal of our R&D program is to find a sensor that can meet the specifications listed in Table 15.

This sensor will be the same size as MIMOSTAR-4. It will have the same pitch, 30 μm, and pixel array, 640 x 640 μm. It also will be thinned to 50 μm. A specific architecture needs to be developed for this design. Based on our experience, we have a good description for this sensor. The device has a active time period much shorter than the readout time. The active period of time is strobed by the STAR trigger, followed by a 1 ms period to read out the full number of pixels.

The general organization of the chip relies on columns processed in parallel. The chip operation includes a continuous cycling over the array with an integration time of 100 to 200 μs. There will be in-pixel storage of the integrated charges, but at this time it is not clear whether CDS can be done "on chip".

The details of the signal processing, i.e. ADC or double threshold discrimination for zero suppression are still open and need to be studied with real data. Studies on this chip will commence this year.

Ladder active area	2 cm × 20 cm
Pixel size	30 μm × 30 μm
~Pixel mapping on the ladder	640 × 6400
Minimum operating distance from beam	1.5 cm
Power	≤200 mW/cm^2
Operating temperature	≥30 °C
Integration time[‡]	≤0.2 ms
Mean silicon thickness	≤100 μm
Readout time	≤1 ms
Efficiency (min I)[§]	≥98%
Accidental cluster density	≤22/cm^2
Binary readout, number of threshold bits[**]	1 or 2
Radiation tolerance [††]	≥171 kRad
Number of conductors supporting the ladder (10 chips/ladder)[‡‡]	≤140
Triggered readout, maximum trigger delay[§§]	2 μs

Table 15: Silicon requirements for maximum average Au+Au RHIC luminosity of 7.0 × 10^{27} Hz/cm^2 or 2.5 nb^{-1}/week.

[‡] The time that a pixel is sensitive to tracks, this determines amount of pileup.

[§] Efficiency after cluster filter on binary threshold information from the detector

[**] To satisfy both the efficiency and accidental requirements it is expected that some off chip cluster analysis will be required. Depending on signal to noise either one or two thresholds will be needed.

[††] 4 year operation at maximum RHIC luminosity for a running period of 21 weeks/year see: W. Fisher, T. Roser, I. Ben-Zvi, A Fedotov, 16-Mar-2005
http://www.phenix.bnl.gov/phenix/WWW/publish/leitch/rhicii-forward/RHIC_II_Luminosity_Roser.pdf

[‡‡] This requirement addresses the radiation thickness of the flex cable that is part of the thin ladder structure. The current proto-type ladder that uses the MIMOSA5 chips has this many conductors. At the end of the ladder there can be additional mass for cables, drivers and cooling.

[§§] The short integration time allows operation of the pixel detector like any other STAR detector, namely one frame associated with one interaction event only. The STAR trigger is delivered 1.6 μs following the collision.

4.7 Mechanical Support Structure

Simulations have shown that for good D meson identification in the high track density environment of Au + Au collisions, it is important to minimize the scattering thickness of the beam pipe and the first detection layer. This requirement has been the primary driver of the current design. By using APS technology we can use thinned silicon with modest connection requirements to minimize the support electronics and cable thickness. In addition, the low power nature of these devices allows a mechanical design that is air-cooled which helps to minimize scattering material in the track path. Several conceptual designs have been considered. We present the design that is currently the focus of our investigations.

In recognition of difficulties encountered in previous experiments, we are adopting design requirements for rapid insertion and removal of the vertex detector, rapid calibration and calibration transfer and multiple detector copies. By addressing these issues early in the design cycle the requirements can be met without major cost impact.

Our mechanical design makes significant use of carbon composite material, which has nearly the same radiation length as beryllium. This allows us to take advantage of the extensive work going on at LBNL for the ATLAS pixel detector.

Since the design of the original STAR detector system, there has been significant progress in tools available for mechanical work. Very powerful low cost 3D CAD programs are now available which allow complex modeling with moving parts and direct interfacing to CNC machines and rapid prototyping. These tools provide the means to tackle the more complex mechanical designs required for rapid insertion and alignment.

4.8 Support Carriage for Pixel Detector for Rapid Installation and Removal

A conceptual design has been developed for the support carriage that will permit rapid insertion and removal without moving other detector components. This system is shown in Figure 43 as it will be positioned for operation in the STAR detector system. The pixel detector is a small detector at the center of the STAR system. Additional layers of tracking (not shown), the IST and the SSD, lie outside of the pixel detector. As shown, the mechanical support and electronic service for the pixel detector is located on one end only. The transparent tan structure in Figure 43 represents the support structure that will be permanently installed and supported by the exiting West cone. This provides support for the pixel detector and its electronics that slide in as a unit. The structure also supports the middle of the beam pipe so that in fine tuning position the pixel detector and beam pipe move as a unit. The detector system shown in Figure 43 allows for rapid removal and replacement while maintaining reproducible position through the use of fully defined

kinematic mounts. For simplicity, several existing STAR structures are not shown in the figure.

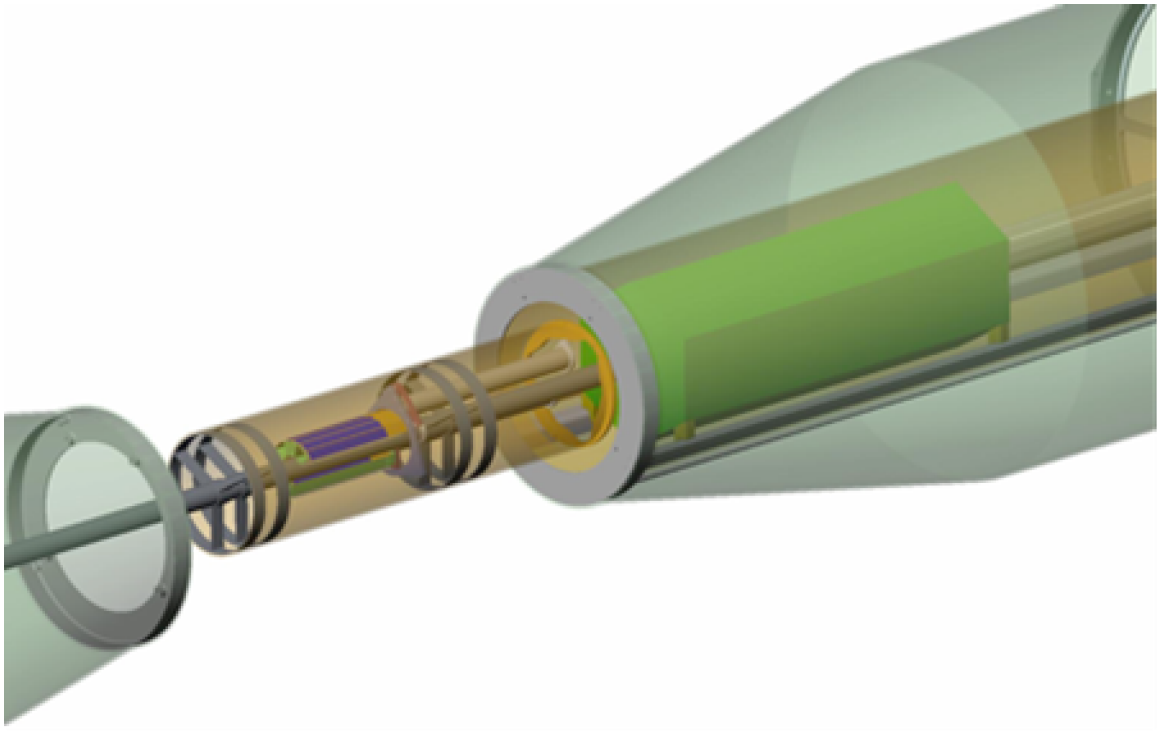

Figure 43: The PIXEL is shown integrated with the STAR inner detectors cone assembly.

A close up view in Figure 44 shows the pixel detector ladder arrangement. There are two tracking layers: one at 2.5 cm radius and the other at 5.0 cm radius. The design shown in this figure consists of ALICE style thin carbon beams that supports 3 detector ladders each, one inner radius ladder and two outer radius ladders. The ladders are composed of thinned detector chips mounted on a flex PC cable that is backed by a thin carbon composite layer. The carbon beam structures are arranged in three modules with three beams per module.

A cut away view of this pixel detector structure is shown in Figure 45. The cooling fin elements which are out of the tracking area provide additional air cooling for the driver heat load at the end of the ladders. Also shown is the 3-point kinematic support for each of the three modules. These kinematic mounts define precise reproducible positions for the ladders.

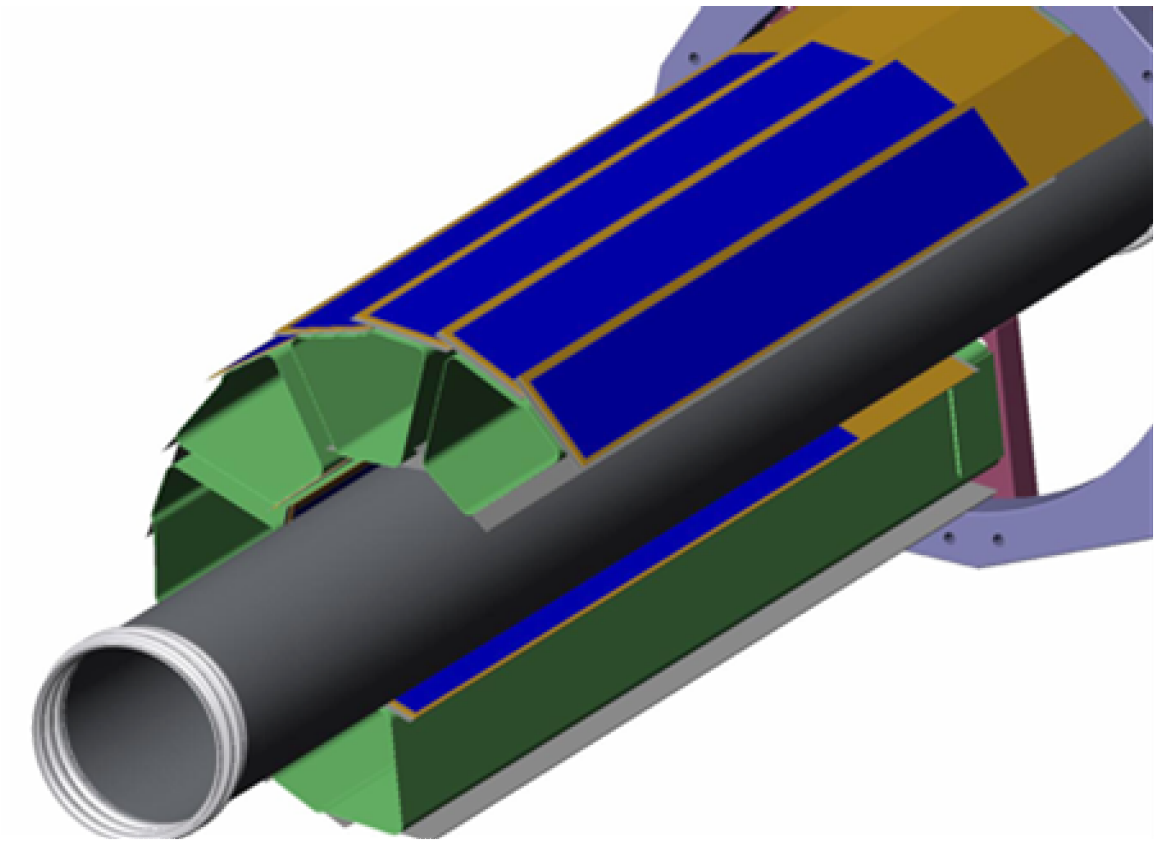

Figure 44: Close up view of the pixel ladders. The system is composed of three separate modules, one of which is removed in this illustration

During installation and withdrawal the modules open up in a controlled path to clear the beam pipe and beam pipe support structures.

4.8.1 Position Alignment and Calibration

The required position resolution of better than 10 μm is a significant challenge for calibration and alignment. The detector system is small and so it permits a design with a single kinematic support to define a reproducible position centered on the STAR system. With the proposed mechanical design the detector system can be moved as a unit between the visual coordinate measuring system and the docking support in the STAR experiment without disturbing the relative pixel ladder positions. The detector silicon will be patterned with a fiducial grid in the top aluminum connection layer. This fine-grained grid will be mapped in 3D with a visual coordinate measuring machine.

The pixel-to-pixel mapping will be preserved through transfer and docking in the middle of the STAR detector system. The calibration burden by track matching will be limited to determining the 6 parameters defining the location of the vertex detector unit within the other STAR detectors. It is expected that success of this approach will require careful temperature control. Further analysis and measurements will quantify this requirement.

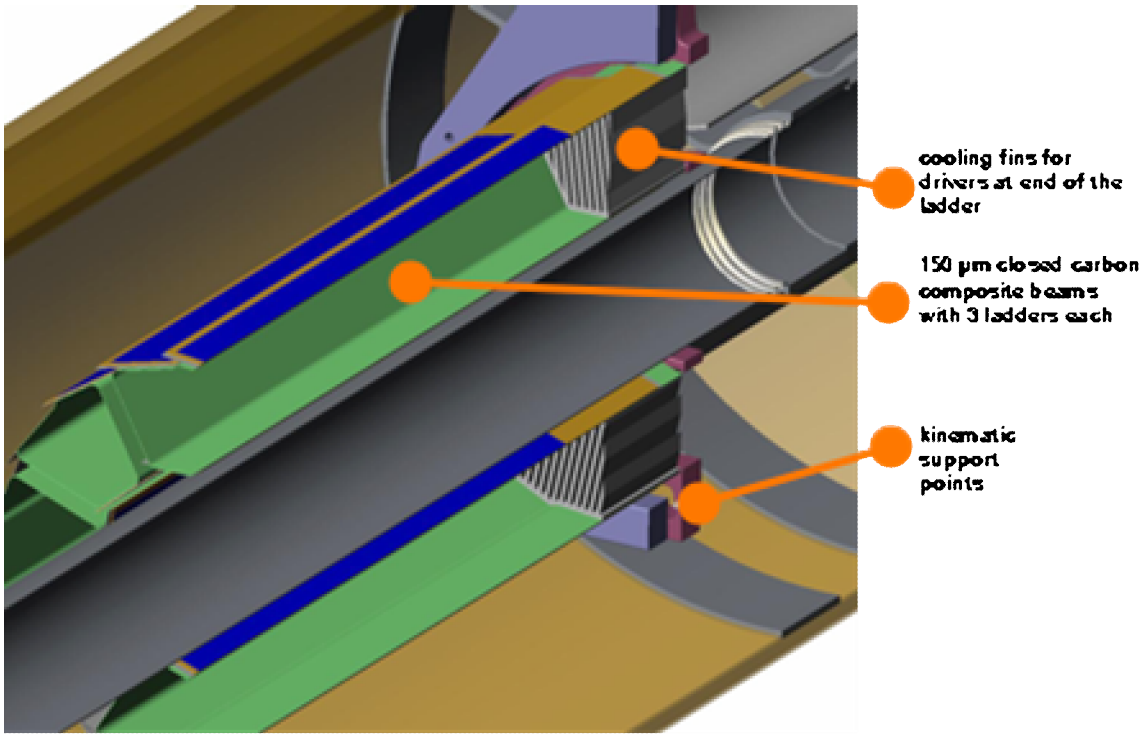

Figure 45: Detector support structure with kinematic mounts to insure repeatable detector positioning.

4.9 Ladder Design and Fabrication

A variety of ladder designs have been evaluated. One design was composed of thinned silicon on a flex PC Kapton cable bonded to thin composite structure with two skins separated by carbon foam. The radiation thickness of this structure is characterized in Table 16. Analysis of this design shows thermal distortion in excess of our desired goal of 20 microns or less. We are now analyzing the design illustrated in **Error! Reference source not found.** and in Figure 47. This is based on the ALICE design and should provide a more stable rigid structure while maintaining comparable radiation thickness.

It was found with test structures that it is relatively straightforward to make wire bonds on these thinned devices where vacuum chucks maintain the sandwich as a flat firm surface. A method to bond the silicon sandwich has been developed using DuPont Pyralux LF thermally activated acrylic sheet adhesive. Advantages of using sheet adhesive include fixed bondline thickness and ease of handling. Other bonding methods including low viscosity epoxies are also under investigation.

A complete ladder using silicon-sandwiches has not been produced yet but we have tested fabrication methods that use a uni-layer silicon structure. We have used vacuum chuck fixturing to butt-join chips side by side against a straight edge and have then

bonded to kapton with Pyralux. This bonded structure was then bonded at room temperature to the carbon beam using Hysol EA9396 aerospace epoxy.

A few μm protective polymer, Parylene, will be used to protect the exposed wire bonds and to control the spread of carbon dust. The Parylene coating process is available in the electronics industry. The coating material is applied at the molecular level by a vacuum deposition process at ambient temperature. The thickness is well controlled and it is uniform without pinholes, so protection can be achieved without compromising detector thickness. Application at room temperature avoids introducing stresses that distort the ladder shape.

4.9.1 Detector Radiation Length

Multiple scattering in the beam pipe and the first inner layer of the vertex detector sets the intrinsic limit of precision for vertex resolution. The radiation thickness for an inner ladder and the beam pipe is given in Table 16. The detector ladder is placed at an angle and is quite close to the interaction point so particles pass through the material at varying angles. This results in path length through the materials that is greater than the thickness. Table 16 also shows the thickness and radiation length of a ladder and the beampipe.

Material	Si equivalent (μm)	Material thickness (μm)	% X_0
Beryllium beam pipe	133	500	0.14
Silicon	50	50	0.053
Adhesive	13.4	50	0.014
Cable Assembly	83.9	125	0.089
Adhesive	13.4	50	0.014
Carbon Composite	103	3200	0.11
Total for **one ladder**	264	3475	0.282

Table 16: Materials in the beam pipe and the first detector layer with their total thickness and radiation length. For details see Ref. [128]

4.9.2 Expected Radiation Exposure

RHIC luminosity projected to 2008 with the assumptions of a 21 week running period and a 60% operating efficiency for Au + Au give a radiation dose of approximately 3.7 kRad/year. This calculation can be found on the web.[129] The materials that we anticipate using in the pixel detector are the same as used in much higher radiation environments like the Atlas pixel detector. One exception is the acrylic adhesive, which exhibits excellent radiation resistance (Radiation Index ~5).[130] Our structure should not exhibit any mechanical degradation from the absorbed dose.

4.10 Ladder Mechanical Tests

4.10.1 Load Distortion Tests

Figure 47 shows an early prototype ladder and detector carrier that we have built. **Error! Reference source not found.** shows a cross-sectional view of the ladder. The mechanical tests have shown that the stiffness and bending characteristics of the assembly are acceptable. For these and similar tests,[131] the ladder's mechanical structure was supported on one end and the surface contours were measured with and without a 10 gram end load using the vision measuring machine at LBNL. The deflection profile is shown in Figure 48 along with the calculated deflection for a simple triangular closed beam. The stiffness is within 20% of expectations from an engineering model. The measured fundamental frequency of the ladder is 140 Hz while the engineering model gives a resonant frequency of 135 Hz and a Q of 45.[132] We have measured the vibrational environment at the STAR detector and it is dominated by low frequencies and so we anticipate that the ladders with the stiffness of our test structure will maintain a relative position to each other of better than a micron.[133]

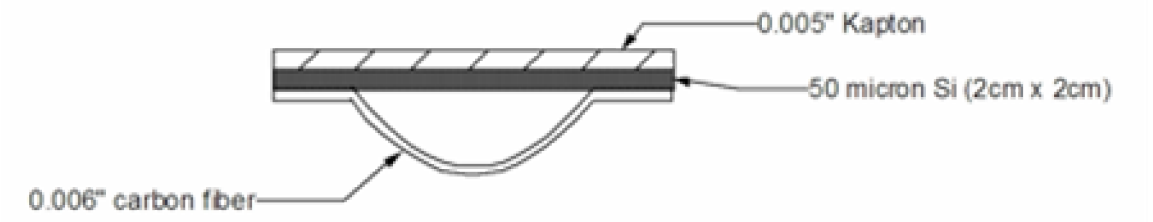

Figure 46: A cross-section of the prototype detector ladder showing its structure and materials

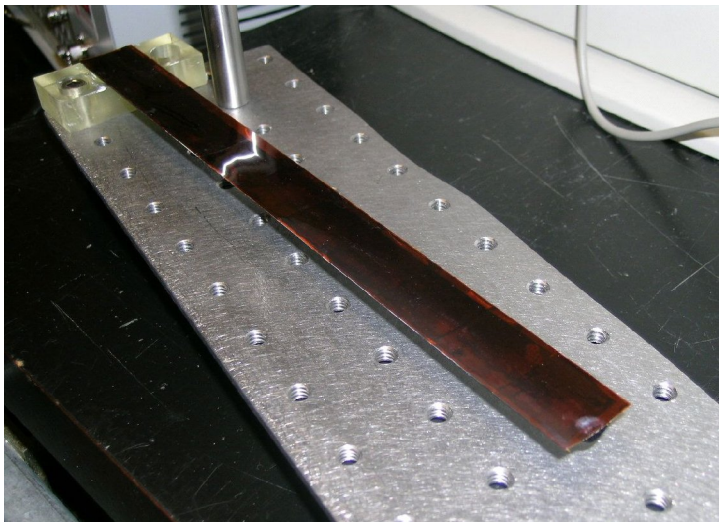

Figure 47: Early prototype ladder and detector carrier.

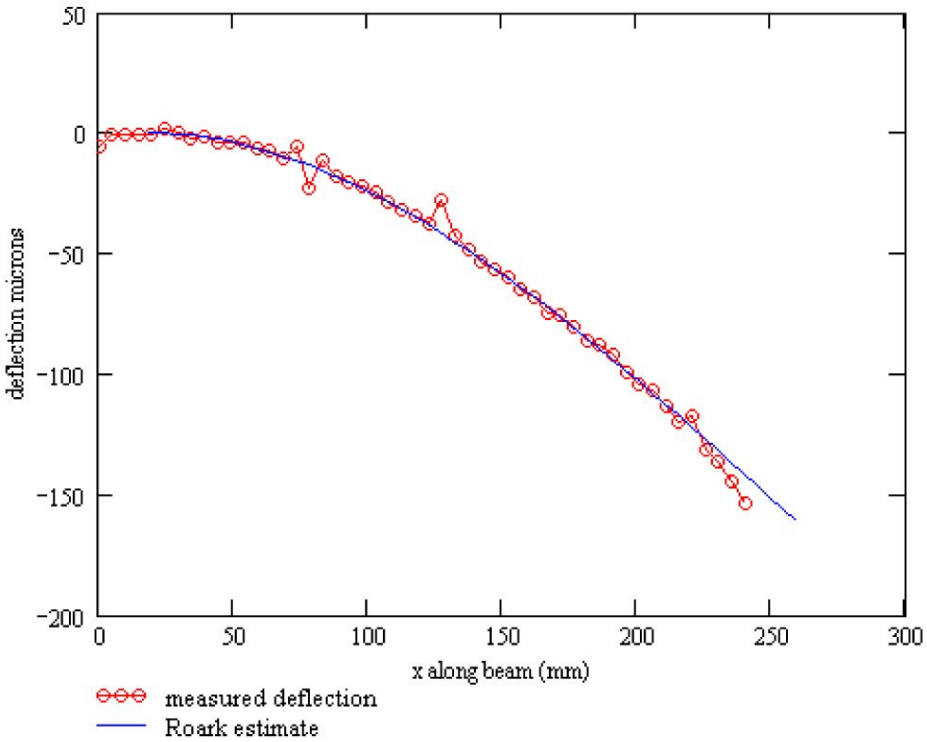

Figure 48: Measured bend of a silicon/carbon composite ladder test structure and the calculated bend shape. The ladder was rigidly supported at one end with a 10 gram weight placed on the other.

4.10.2 Thermal Distortion Tests

We have measured thermally generated deflections using TV holography.[134] This tool, available to us, courtesy of the ATLAS Pixel project, provides a rapid visual distortion map on the sub micron scale. This is proving to be a useful tool for identifying and understanding different design parameters. Measurements are done on structures thermally isolated in a transparent box as shown in Figure 49. This tool will also be used to test the stability of the final detector.

4.10.3 Cooling Measurements

In the interest of low mass, the detector system is being designed to use air-cooling for the detector structure in the active tracking volume. A small wind tunnel has been constructed (see Figure 49) to evaluate the cooling capacity of air and the design of the system. Measurements with resistive heated ladder test structures and thermocouple readouts show that air velocities on the order of 1 m/s are sufficient to handle power levels of 150 mW/cm^2. This setup, with its thermal camera, will be used to check operating silicon-ladder-devices to evaluate localized heating issues. In addition to cooling tests the wind tunnel is being used to evaluate the vibration stability of the ladder design under the required wind flow conditions. The amplitude of cooling air driven vibrations in the ladder is measured with non-contact capacitive probes[135] and if necessary specific vibration modes can be monitored with the TV holography system. The vibration induced by the air cooling gives an acceptable positional location σ of 1.6 μm. The low mass ladder structure is the critical design element requiring vibration testing, but the full detector structure will be evaluated with this system as well.[136] Additional information on the cooling studies is available on the web.[137]

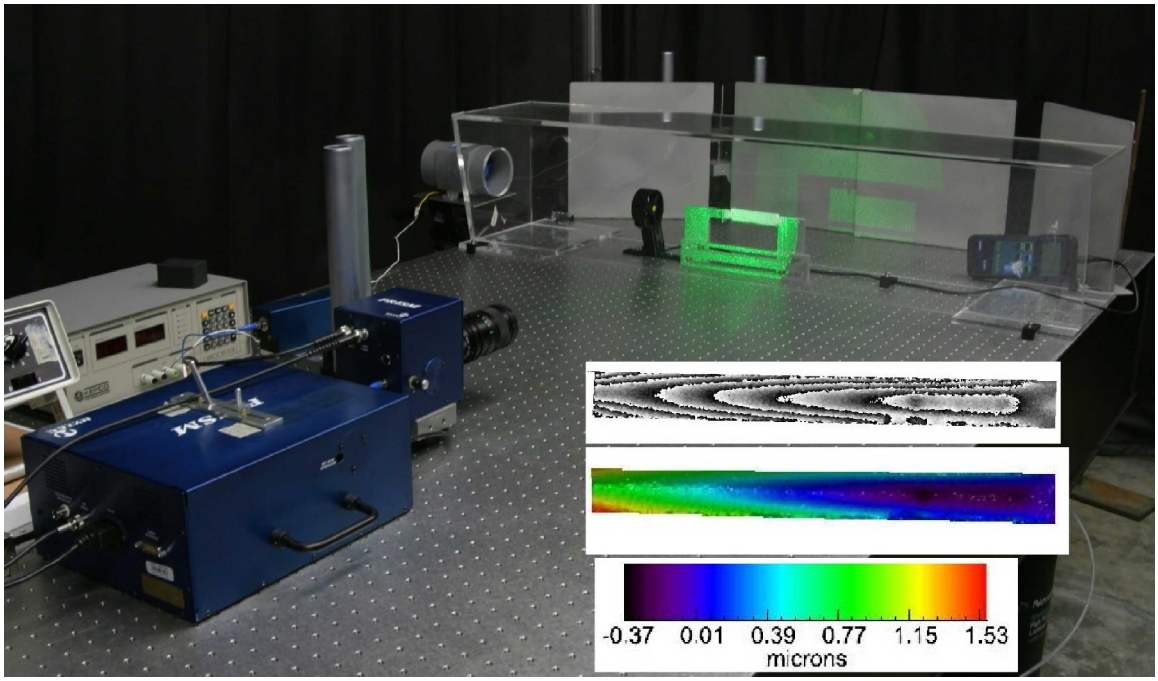

Figure 49: TV Holography system viewing test ladder in a small transparent wind tunnel. Inset shows diffraction pattern with color map of the surface displacement.

4.11 Cabling

Connection to the detector readout chips will be done with an aluminum kapton cable. The cable is part of the ladder and is located underneath the pixel chip. It will carry power, clock, analogue signals and control. We have found a commercial vendor that makes aluminum cables with vias. Fabrication tests have been done with 0.35 mil aluminum with 1 mil Kapton plus two 1 mil acrylic adhesive layers. Wire bonding tests with this material have been successful.

Figure 50 shows the prototype for a pixel readout cable. The prototype is an active cable with a buffer and differential amplifier for each sector of 10 MIMOSA-5 detectors. The final detector readout cable will not have the components shown, will be narrower, and will be sized to be slightly wider than the detectors themselves to allow wire bonding. The cable in the figure uses a copper conductor on a 25 μm Kapton insulator. The final cable will be a 4-layer low-mass aluminum conductor cable with a radiation length equivalent of 84 μm of Si. The prototype has been successfully tested and is working in our prototype ladder readout system. Additional and more recent information on cable and ladder developments may be found on the web.[138]

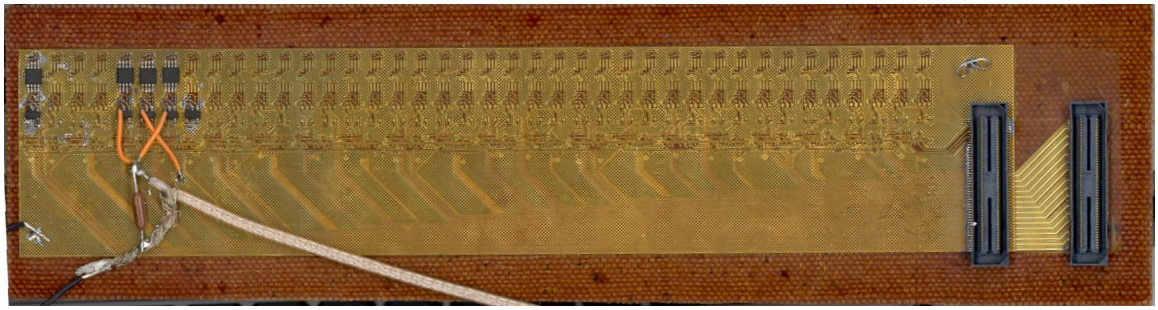

Figure 50: A prototype readout cable for the PIXEL.

Figure 51 shows a mechanical Prototype with 4 MIMOSA-5 detectors glued to the Kapton cable assembly with a thin acrylic film adhesive. The adhesive has a bond line of 50 μm. The MIMOSA is relatively flat in horizontal direction but has a "dish" shape in vertical (y) direction. The magnitude of these distortions is, however, quite small. The largest deviation from a linear fit in y is only ± 6 μm. This low rate of deformation will allow us to make a minimum number of measurements of the detector positions on the ladders in order to locate the individual pixel position to the required accuracy by a parameterized location function.[139]

Figure 51: Mechanical Prototype with 4 MIMOSA-5 detectors glued to the Kapton cable assembly.

4.12 Data Acquisition and Readout

We are designing the readout and data acquisition system for the PIXEL in two stages. These stages follow the development of the silicon sensors in our project. The initial prototype readout system is designed to read out the MIMOSTAR-4 detectors which have

analog outputs and a 4 ms readout time. The second stage is for use with the final Ultimate series sensors which have a digital output and a 1 ms readout time but only a 200 μs integration time. The goal of the first stage is to develop much of the infrastructure for doing cluster finding and data sparsification, the interfaces to trigger and DAQ and the mechanical readout structures and assemble a working prototype detector with the MIMOSTAR-4 sensors. The second stage would make use of the development that we have done with the prototype detector and integrate the Ultimate series sensors with a developed readout system.

4.13 Requirements and Prototype Design

The requirements for the prototype and final readout system are very similar. They include:

- Triggered detector system fitting into existing STAR infrastructure and interfaces to the existing Trigger and DAQ systems.
- Deliver full frame events to STAR DAQ for event building at approximately the same rate as the TPC.
- Reduce the total data rate of the detector to a manageable level (< TPC rate)

We have designed the prototype data acquisition system to read out the large body of data from the individual MIMOSA4 sensors, to digitize the signals, to perform data compression, and to deliver the sparsified data to an event building and storage device. A summary of the specifications and requirements is provided in Table 17.

Total number of pixels	1.35×10^8
Number of pixels per chip	640×640
Pixel Readout rate (analog output)	2×50 MHz / chip
Readout time per frame	4 ms
Frame integration time	4 ms
Noise after Correlated Double Sampling	10 e^-
Maximum signal	900 e^-
Dynamic range after Correlated Double Sampling	8 bits
Total sensor power consumption (24 33 ladders)	90 132 W

Table 17: Prototype Stage Requirement Summary - constraints for the MIMOSTAR-4 APS.

Digitizing the analog signal on each pixel into a 12 bit digital signal yields approximately 1.2 Gb/s per sensor chip when read out in 4 ms. Thus, the total front end data rate is ~50.7 GB/s. Clearly, the volume of data must be reduced before being passed to the DAQ event builder and written to storage.

Data compression is achieved by performing correlated double sampling (CDS) i.e. subtraction of two consecutive frames followed by zero suppression. CDS cancels out fixed pattern and reset noise and reduces 1/f noise. The fixed pattern noise corresponds to the spread of the baseline voltage in all pixels. It has been measured on the MIMOSA-5 chip to be 2000 electrons. The noise remaining after CDS must be on the order of 14 e^- to guarantee an efficiency of greater than 98%. The maximum signal is estimated from dE/dx calculation and by measuring how the charge spreads over pixels. The signal can be truncated above 900 e^- without compromising either the efficiency or the position resolution, so 8 bits is a sufficient dynamic range for signal storage. A synchronous cluster finding algorithm and the reduction of the data to addresses of cluster center pixels reduce the data to a manageable rate.

4.14 Architecture for the Prototype System

The basic flow of a ladder data path starts with the APS sensors. An PIXEL ladder has 10 MIMOSTAR-4 APS chips each with a 640 by 640 pixel array. Each chip is divided in half with two sectors each containing a separate analogue, differential current output buffer. The chips are continuously clocked at 50 MHz and the data is read out, running serially through all the pixels connecting them to the output buffer. This operation is continuous during the operation of the MIMOSTAR detectors on the PIXEL ladder. Analog data is carried from the two 50 MHz outputs in each sensor in parallel on a low mass ladder flex printed circuit board to discrete electronics at the end of the ladder and out of the low mass detector region. This electronics performs current to voltage conversion and contains buffers and drivers for the clocks and other control signals needed for ladder operation.

Each MIMOSTAR detector requires a JTAG connection for configuration of the chip, power, ground and a 50 MHz readout clock. These signals and power as well as the analog outputs and synchronization and marker signals from the detectors are carried via a low mass twisted pair cable from the discrete electronics at the end of the ladder to the readout electronics located about 1 meter from the PIXEL ladders. There is one readout board per PIXEL ladder. A functional diagram of a PIXEL ladder and a description of the data flow are shown in Figure 52.

The readout electronics currently consist of a motherboard and daughter card configuration. A functional block diagram is shown in Figure 53. There are 3 daughter cards per motherboard and each daughter card is capable of servicing 4 of the MIMOSTAR sensors on the ladder. The analog signals are carried to the daughter cards where they are digitized with a 12-bit ADC at 50 MHz. Following digitization, ADC values are passed synchronously to an FPGA for CDS. Performing CDS requires that a data sample be stored for each pixel of the detector. This requirement drives the need for

external RAM on the daughter cards. After CDS and pedestal subtraction, 8 bits is used to represent the data. The data is then transferred to the next stage for hit finding and data reduction.

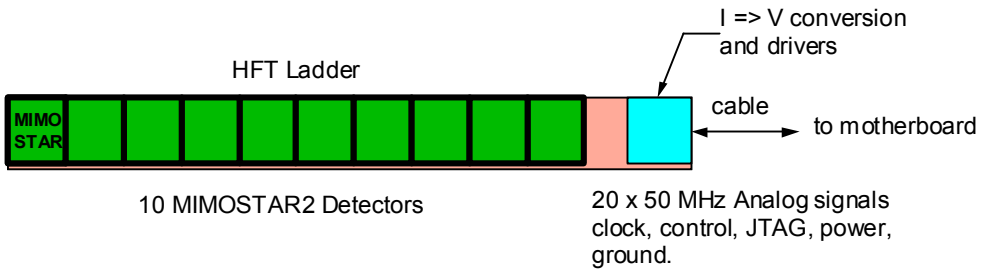

Figure 52: Ladder Layout - sketch of the readout-topology on a detector ladder. This figure shows the ten APS and the corresponding current to voltage conversion and driver electronics. The drivers will be located out of the low mass region of the detector and may require additional cooling.

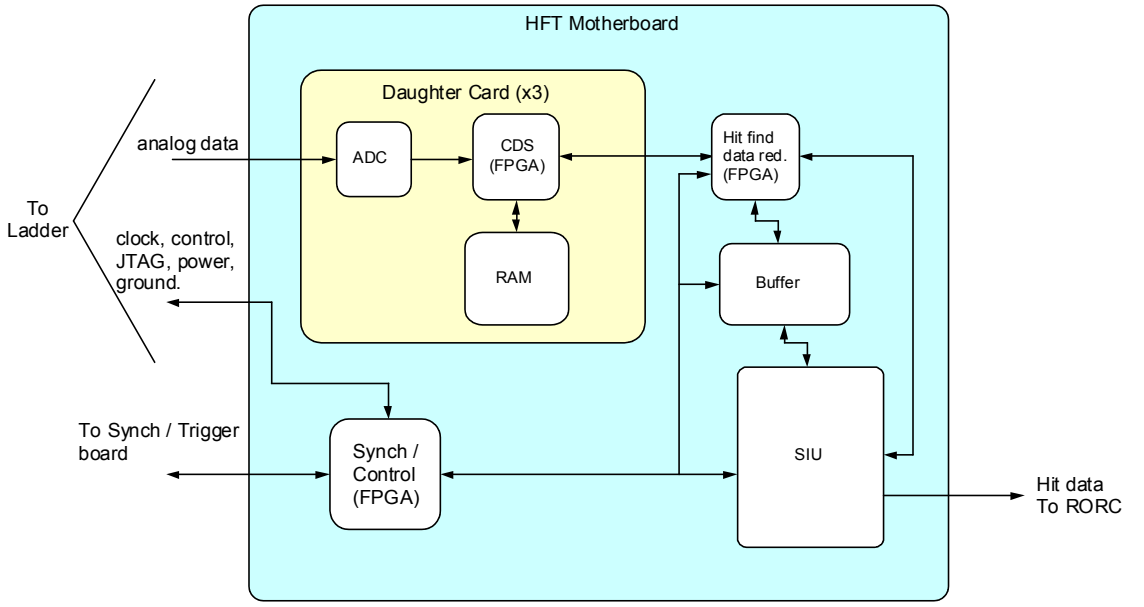

Figure 53: Prototype DAQ Layout: schematic of DAQ system for a single MIMOSTAR-4 ladder. Analog data is carried as differential current on the low mass cable at 50 MHz. The signals are driven in parallel over short (~1m) twisted pair cables to the motherboard. Analog to digital conversion, CDS and data reduction are performed in the Motherboard/Daughter cards. The reduced hit data is transferred digitally to the SIU and carried to Linux based readout PCs via an optical fiber. Control, synchronization, and event ID tagging are accomplished in the Control/Trigger FPGA on the motherboard.

The 8-bit data data exiting the CDS stage is resorted on the fly to be a traditional raster scan through the pixels of the sector. This stream of rasterized data can then be passed to the cluster finder. We are currently investigating methods of hit finding and data

reduction for use on the motherboard. A simple readout of the address of a center pixel high threshold hit with the surrounding 8 pixels meeting additional cluster selection criteria such as at least 1 cell over the low threshold is our default approach. This can be implemented in an FPGA and run as a pipeline filling the output buffer with center pixel address values. A simple example of an FPGA logic diagram that accomplishes this can be seen in Figure 54. We are also investigating a number of cluster selection methods including summing algorithms around different thresholds and center pixel determination by geometric pattern with high and low thresholds. A preliminary study of some simple and FPGA implementable cluster finding algorithms shows promising results for efficiency and noise rejection. A sample of these results is shown in Figure 55 and Figure 56 where one can see that the efficiency and fake hit rate for a low threshold crossing in one of the surrounding 8 pixels of a 9 pixel cluster candidate is comparable to a much more complex ADC sum for a reasonable range of cuts and provides greater than 99 percent efficiency with an accidental rate of less than 10^{-4}.

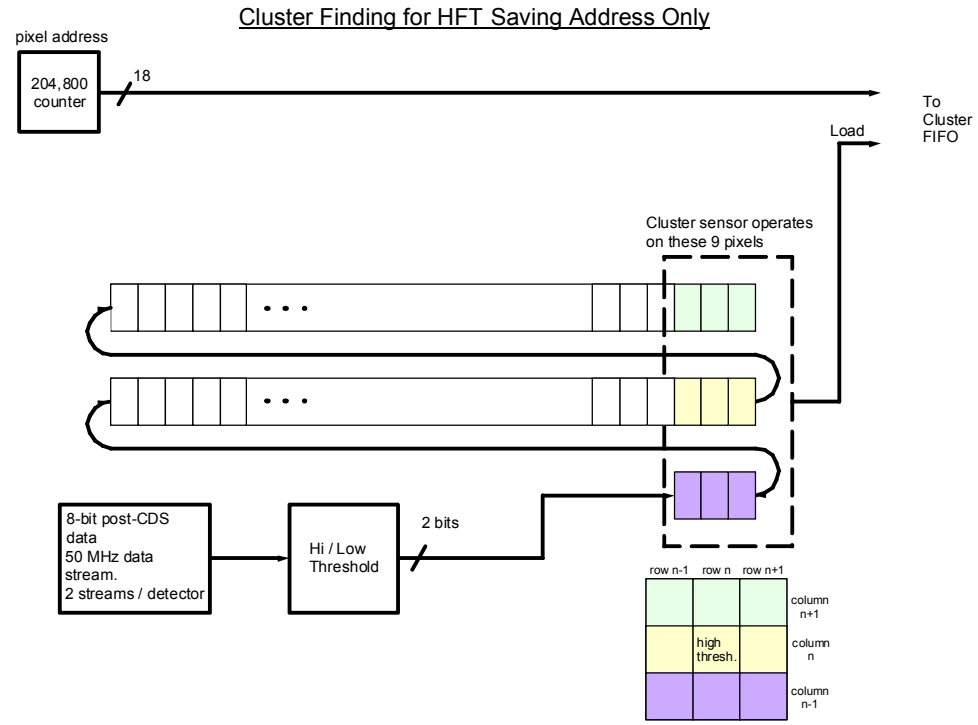

Figure 54: A simple cluster finding algorithm for the PIXEL detector. ADC data from two MIMOSTAR detector columns + 3 pixels are sent to a high/low threshold discriminator. The resulting 2 bits are fed sequentially in an 2-bit wide shift register. The center pixel of a 3 × 3 pixel window is compared to a high threshold with each clock tick. If the threshold is exceeded, the additional cluster identification criteria are checked for the 3 x 3 pixel window. If the results meet the critera for a cluster, the center pixel address is stored into a readout FIFO.

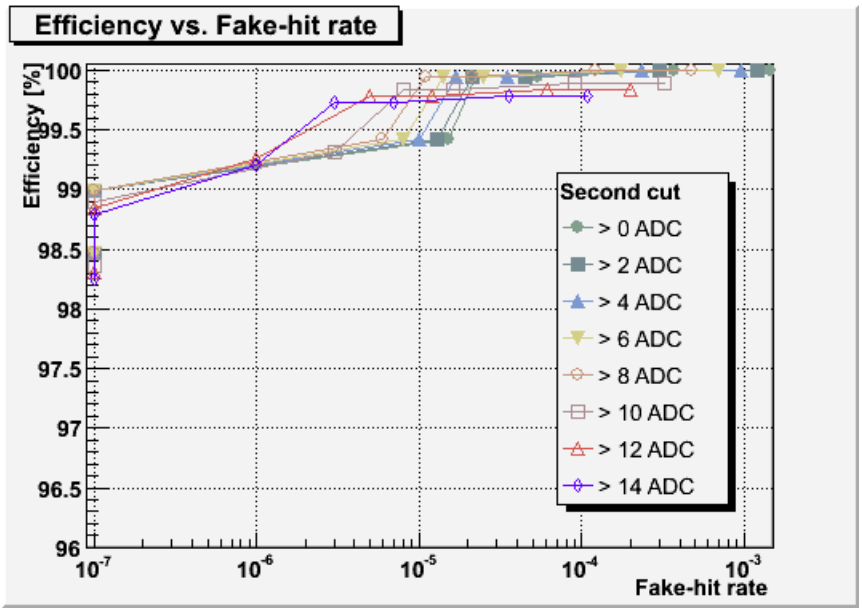

Figure 55: Efficiency versus accidentals and fake hit rate as a function of cuts for a standard cluster finding algorithms run on cluster data from a MIMOSA5 detector. Note that some parameter combinations of this algorithm are already over 98% efficient with consisting of a accidentals rate of 1-2 hits / cm^{2}high center pixel ADC and a sum of the surrounding eight pixels in a 3 x 3 pixel box. Center pixel ADC cut runs from 15 to 8 and is denoted by the markers. The color of the line denotes the cut on the 8 surrounding pixel sum.

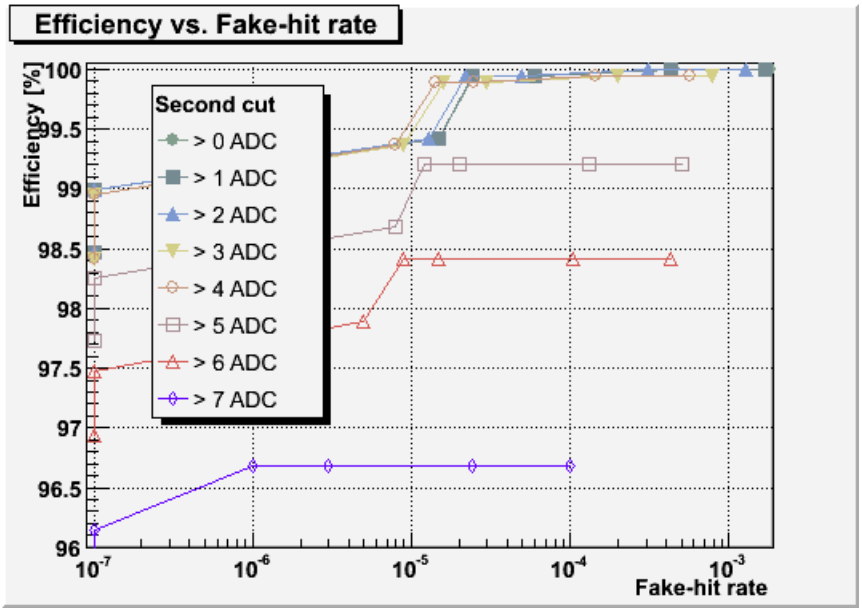

Figure 56: Efficiency and fake hit rate as a function of cuts for the proposed cluster finding algorithm with a high threshold crossing in the center pixel and a low threshold crossing in any of the surrounding eight pixels in a 3 x 3 pixel box. For a reasonable range of cuts, this algorithm is quite comparable to the traditional ADC sum method.

The reduced data is then buffered and transferred to the STAR DAQ system over a high-speed bi-directional fiber link. We intend to use the Source Interface Unit (SIU) and

Readout Receiver Cards (RORC) developed for ALICE as our optical link hardware to transfer data to and from the STAR DAQ system. These links have been chosen as the primary readout connections for the new STAR TPC FEE. Leveraging existing hardware and expertise in STAR allows for a faster and more reliable design than developing our own custom solution. The complete system consists of a parallel set of ladder readouts consisting of 33 separate chains.

4.15 Data Synchronization, Readout and Latency

The readout of the prototype PIXEL sensors is continuous and hit and cluster finding is always in operation during the normal running of the detector. The receipt of a trigger initiates the saving of the found clusters into a FIFO for 1 frame (204,800 pixels). The PIXEL detector as a whole will be triggered via the standard STAR TCD module. Since 4 ms are required to read out the complete frame of interest, the data will be passed to DAQ for event building ~ 4 ms after the trigger is received. We will provide multiple buffers that will allow the capture of temporally overlapping complete frames. This will allow us to service multiple triggers within the 4 ms readout time. A functional block diagram of this system is shown in Figure 57. In this system, the cluster data is fanned out to 5 Event FIFOs. A separate Event FIFO is enabled for the duration of one frame upon the receipt of a trigger from the TCD. Subsequent triggers enable additional Event FIFOs until all of the event FIFOs are full and the system goes busy. The resulting separate complete frames are then passed to STAR DAQ as they are completed in the Event FIFOs. This multiple stream buffering gives a system that can be triggered up to the expected rate of the STAR TPC (approximately 1 KHz) after the DAQ1K upgrade. This will result in the duplication of some data in frames that overlap in time, but our data rate is low and the duplication of some data allows for contiguous event building in the STAR DAQ, which greatly eases the offline analysis. In addition, synchronization between the ladders/boards must be maintained. The PIXEL will receive a clock via the standard STAR TCD and will derive its internal clocks from the RHIC strobe. We will provide functionality to allow the motherboards to be synchronized at startup and any point thereafter.

4.16 Data Rates for the Prototype RDO

The ADC data rate from each 640 × 640 MIMOSTAR detector is approximately 4.9 Mb per frame or 1.2 Gb/sec. The total rate of raw ADC data entering the processing chain in the detector is thus approximately 50.7 GB/sec. After CDS, the data can be represented by 8 bits. Pixel addressing within a sector requires 18 bits. The sector-in-ladder address will be accomplished as address words in the data stream. Ladder address will be added at the DAQ receivers. This covers the address space to map the detector pixel space.

Each cluster word stored in the FIFO contains the 18 address bits of a cluster central pixel. Combining this with the occupancy per layer, the overhead for event format and headers and the readout rate of 1 KHz (with data duplication in the event FIFOs) gives an event size of 114 KB and data rate from the detector of 114 MB/sec. Figure 58 shows this graphically.

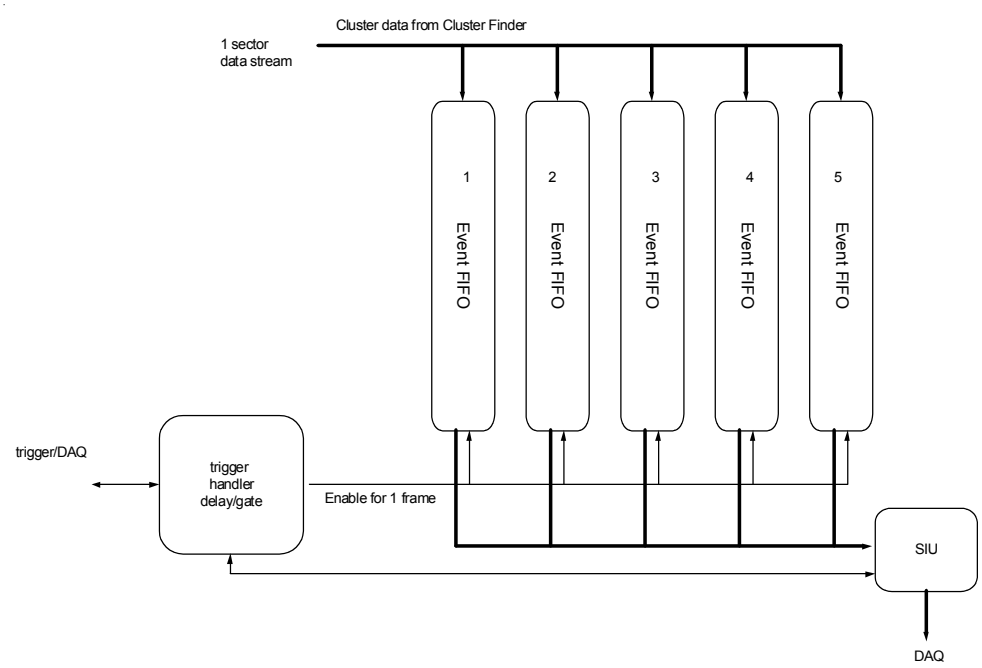

Figure 57: Multiple event FIFOs are fed in parallel from the cluster finder. A separate Event FIFO is enabled for one frame upon the receipt of a trigger from the TCD. The resulting separate complete frames are then passed to STAR DAQ as they are completed in the Event FIFOs.

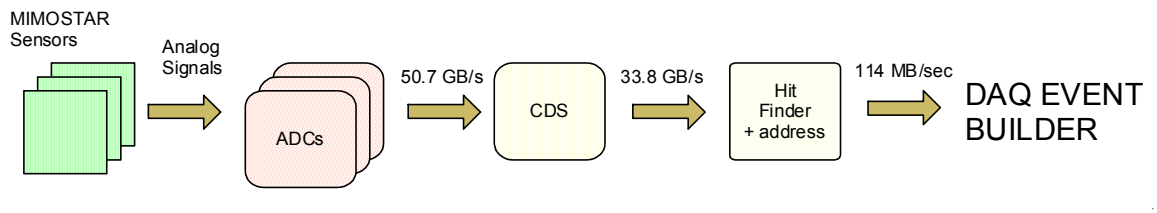

Figure 58: Data rates at the various stages of the Prototype MIMOSTAR-4 readout chain.

Item	Number

Bits/address	18
Inner ladders (r=2.5 cm)	9
Middle ladders (r=6.5 cm)	12
Outer ladders (r=7.5 cm)	12
MIMOSTAR sensors per ladder	10
Average hits/sensor, inner, L = 10^{27}	212
Average hits/sensor, middle, L = 10^{27}	43
Average hits/sensorr, outer, L = 10^{27}	35
Trigger rate	1 KHz

Table 18: Data rate calculation parameters

4.17 Requirements for the Ultimate Design

The Ultimate series of APS detector will incorporate several changes from the previous MIMOSTAR versions. The primary changes include on pixel CDS and a two level programmable discriminator applied to the CDS output for each chip. The Ultimate chip will be read out digitally in 2 bit words / pixel through 4 LVDS outputs / chip. The control functions for the chip are still via the JTAG interface. A summary of basic requirements is given below..

Physical

- 640 x 640 pixels with 30um pitch.
- Minimum of 3 fiducial marks / chip for optical survey purposes.
- All bonding pads located along 1 side of chip
- Two bonding pads per I/O of the chip to facilitate probe testing before sensor mounting.

Electronic

- Continuous cycling 100-200 μs integration time.
- Trigger input reads out the previous 200 μs integration window.
- On chip CDS for the pixels.
- On chip JTAG programmable discriminator thresholds, biases, etc.
- 4 LVDS readout channels / chip with a full readout time of less than 1 ms.
- JTAG programmable testing modes.
- Appropriate flags for readout synchronization, e.g. first.pixel marker
- Synch input to start chip function.

- Signal / Noise > 9 at operating temperature of 30 degrees C.
- Maximum average power dissipation of 100 mW / cm2.

This system readout is different from the previous MIMOSTAR-4 based readout but most components are the same.

4.18 Architecture for the Ultimate System

In this system, much of the functionality of the daughter cards has been moved into the Ultimate sensors themselves. The correlated double sampling and dual level discriminator functionality are now integrated onto the sensor and there are 4 LVDS readout lines / chip. The rest of the system, however, remains substantially the same. A revised functional block diagram is shown below in Figure 59.

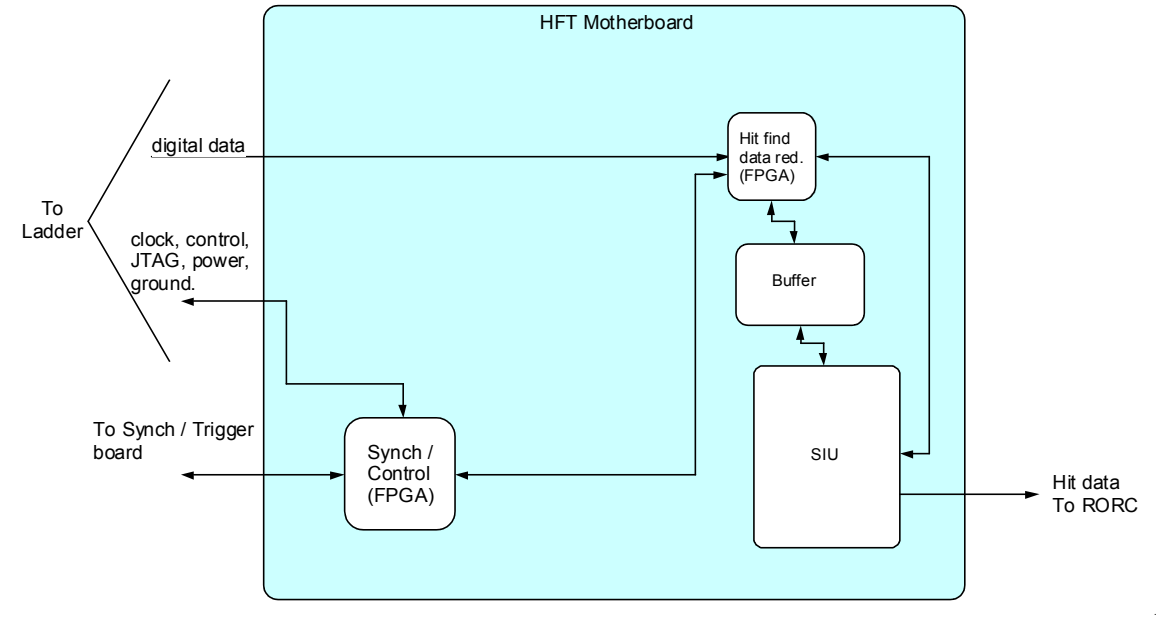

Figure 59: Functional block diagram for Ultimate sensor based readout system.

4.18.1 Data Flow

The Ultimate sensor readout system is a parallel system of 33 ladders, each with the same readout, thus the readout system for a single ladder is presented as the basic building block of the system. In this readout design, the sensors are as described above and are triggered. Triggers, clock, JTAG, Synchronization and markers are provided from the Readout board. After receiving a trigger, the sensors perform a high/low threshold compare to the CDS value for each pixel and send a serial stream of the logic values results of this threshold comparison through LVDS buffers located at the end of the ladder (out of the low mass region) to the Readout board via low mass twisted pair cable.

On the Readout board the data is transferred into high speed memory located in an FPGA. This memory now contains the full contents of each pixel on the sensor represented by a 2 bit string with the hot pixel map implemented as a mask. The sensor threshold data is then run through a cluster finder with the same form as previously described in our readout system and the resulting center address is passed to a cluster FIFO. The contents of these cluster FIFOs are built into an event with header and event ID information and the resulting event is passed to DAQ via the DDL.

4.18.2 Timing and Implementation

The proposed time structure of the readout is shown in Figure 60.

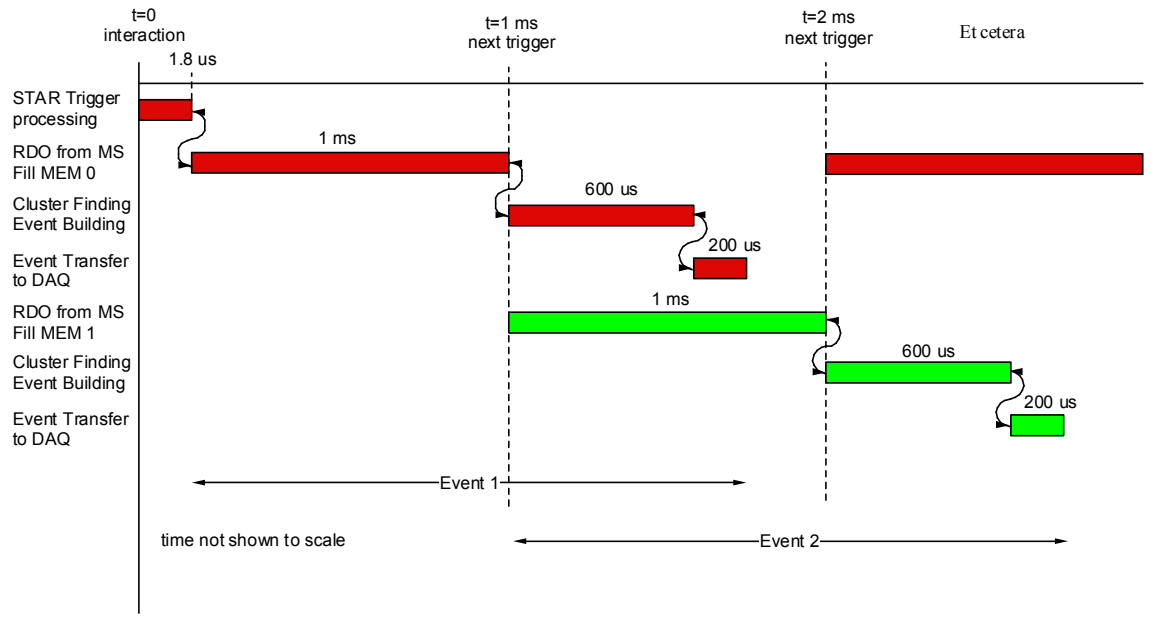

Figure 60 - Proposed time structure of the Mimostar Ultimate readout. To meet the 1 KHz trigger requirement, we require two memory buffers to allow for immediately retriggered readout of the sensor.

The requirement of servicing a 1 KHz trigger combined with the 1 ms readout time of the sensors drives us to implementing two full sensor readout buffers in a ping-pong configuration. Data resorting, if required, will be implemented in the memory controller to give a raster scan data image in the memory. The hot pixel map will also be implemented as a mask in the memory. Unlike the synchronous analog readout cluster finder, which operates on the readout clock (50 MHz), the cluster finding for the Ultimate sensor can run at implementation speed in the FPGA which is significantly faster. The event building readout into the event buffer similarly will run at FPGA implementation speed. Data transfer through the DDL is fast and additional event FIFO buffers can be implemented if needed.

It is important to note that current FPGAs have significant memory block resources. The Xilinx Virtex-5 can be purchased in configurations that have 11.664 Mbit of block memory and 550MHz internal clock distribution.[140] We could implement the entire RDO system for one ladder on two Xilinx Virtex-5 FPGAs in the current technology. By the time this design will be implemented we expect to see further improvements in FPGA technology.

4.19 Data Rates for the Ultimate RDO

We use the same parameters as used in the prototype system data rate calculations but scale the occupancy to reflect the much smaller 200 μs integration time. We obtain the following rates. Note that the rates are still for the 10^{27} luminosity. Please scale as appropriate.

The data rate from each 640 × 640 Ultimate detector is 102 MB / sec. The total rate of raw data entering the processing chain in the detector is thus approximately 3.38 GB/sec. Pixel addressing within a sector still requires 18 bits and is padded to 32 bits in our event format. Combining this with the occupancy per layer and the readout rate of 1 KHz gives an event size of 22.8 KB and data rate from the detector of 22.8 MB/sec. Figure 61 shows this graphically.

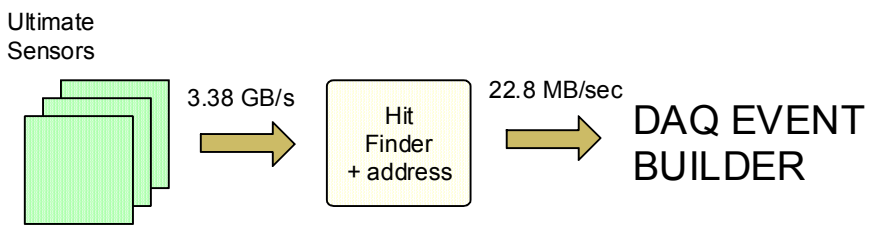

Figure 61: Data rates in ULTIMATE PIXEL readout.

4.20 Prototype Telescope

Several different prototype readout electronics boards have been constructed and tested that are very similar to the proposed prototype readout electronics described above. In Figure 62 one can see the prototyping results of a low mass flex PCB on a ladder with MIMOSA-5 detectors. This prototype flex cable has the signal trace configuration that we expect to use (except in copper conductor rather than aluminum) for the final readout for both the prototype and Ultimate ladder readout.

Figure 62: A prototype ladder showing low mass PCB, MIMOSA5 detectors and driver electronics bonded to a mechanical carbon fiber and reticulated vitreous carbon foam based carrier.

A prototype readout system for reading the MIMOSTAR-2 sensors was also constructed. The MIMOSTAR-2 sensor is a preliminary prototype for the MIMOSTAR-4 and contains the basic interface and functionality that we expect to have in the first stage prototype detector[141]. We are developing a three MIMOSTAR-2 sensor telescope for test during the 2007 beam run at RHIC. Our goal is to test functionality of a prototype MIMOSTAR-2 detector in the STAR environment. We anticipate gathering information on:

- Charged particle environment near the interaction region in STAR.
- Performance of our cluster finding algorithm.
- Performance of the MIMOSTAR-2 sensors.
- Functionality of our tested interfaces to the other STAR subsystems.
- Performance of our hardware and firmware as a system.
- The noise environment in the area in which we expect to put the final pixel detector.

To realize this goal we are assembling a prototype telescope and the mechanical infrastructure and positioning system to allow us to place a 3 MIMOSTAR-2 detector telescope into the STAR magnet near the interaction region. This plan presents challenges in the mechanical, electronics, firmware and infrastructure aspects of assembling and integrating a prototype system into the STAR environment.

Three separate MIMOSTAR-2 chips are mounted in a telescope configuration. This system is controlled and read out into a motherboard mounted to a Stratix development board.[142] Trigger and clock come from the STAR TPC detector subsystem cables as does power. This system is meant to be a functional test of our intended prototype PIXEL readout system. A block diagram of the test system is shown in Figure 63.

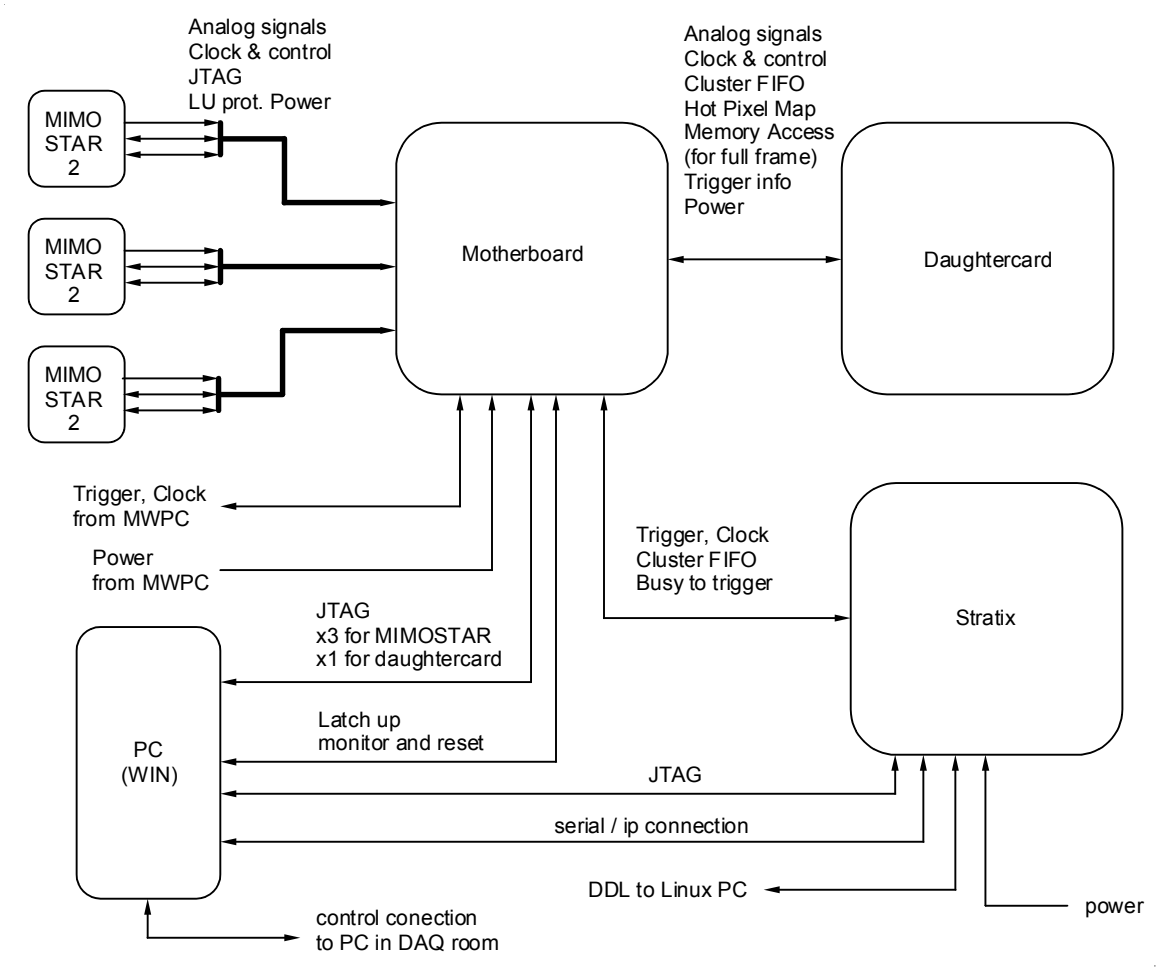

Figure 63: Block diagram for the PIXEL MIMOSTAR-2 three detector telescope to be tested in the STAR 2007 beam run.

In this test, the basic data flow is as follows. Triggers are received from the STAR triggering system into the motherboard and implemented in the FPGA on the daughter card. MIMOSTAR-2 Configuration (JTAG), latch up protected power, clock, sync and reset are provided via shielded CAT-5 cables from the motherboard.[143] The MIMOSTAR-2s will be running in parallel with multidrop LVDS clock and only 1 marker signal is brought out for synchronization. The analog signals and marker signals are transferred from the MIMOSTAR-2 detectors mounted on the flex PCBs[144] via the same CAT-5 cables back to the motherboard and routed to the daughter card[145] for ADC conversion, data resorting, CDS and cluster finding. Cluster addresses or full frame data (raw or CDS) is then routed from the daughter card through the motherboard into the Stratix development board and to our data acquisition linux PC via the CERN ALICE DDL / RORC modules. From the DAQ linux PC, the events are built into the STAR event structure and/or into our own event files.

The hardware used in this test consists of 3 MIMOSTAR-2 detectors mounted on 25 micron kapton flex PCBs, a motherboard, daughter card, Stratix development board, DDL, DAQ linux PC and configuration PC. Photographs of the assembled motherboard, daughter card, Stratix development board and DDL, and of the assembled cable are shown in Figure 64.and in Figure 65.

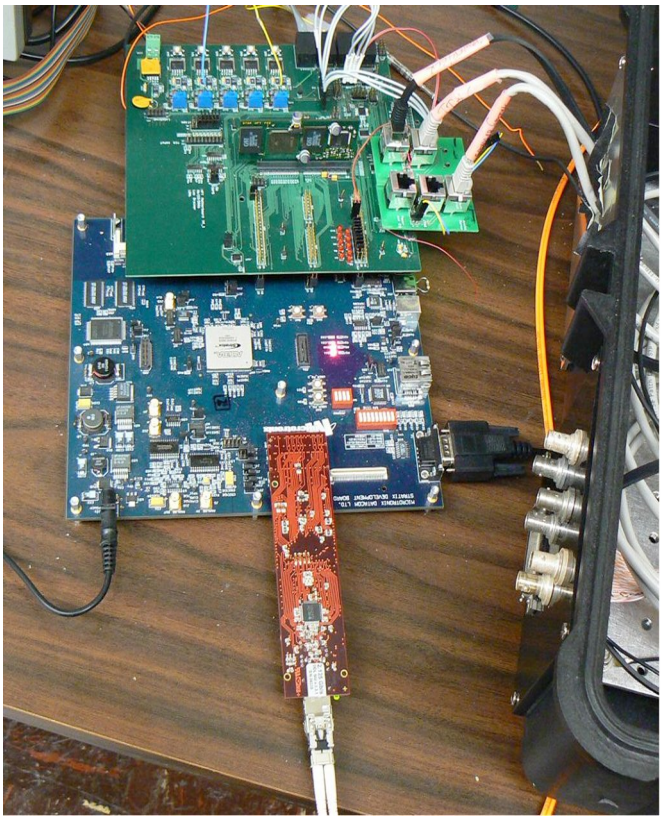

Figure 64: Photograph of PIXEL prototype readout system containing motherboard, daughter card, Microtronix Stratix development board and CERN DDL fiber optic interface module.

The firmware required for this test includes most all of the functionality of the final firmware needed for the full detector. The following basic functionality is required:

Implemented on daughter card

- Accept and respond appropriately to triggers in the STAR trigger system.
- SRAM memory controller
- 50MHz 12bit ADC serial interface
- Data re-sorter
- CDS
- Full frame readout
- Cluster finding
- Cluster FIFO building

Implemented on Stratix board

- Event building
- JTAG configuration of the chained MIMOSTAR-2 chips from the Stratix board.
- Interface to control shell
- DDL control and interface
- Latch-up detection and remote reset

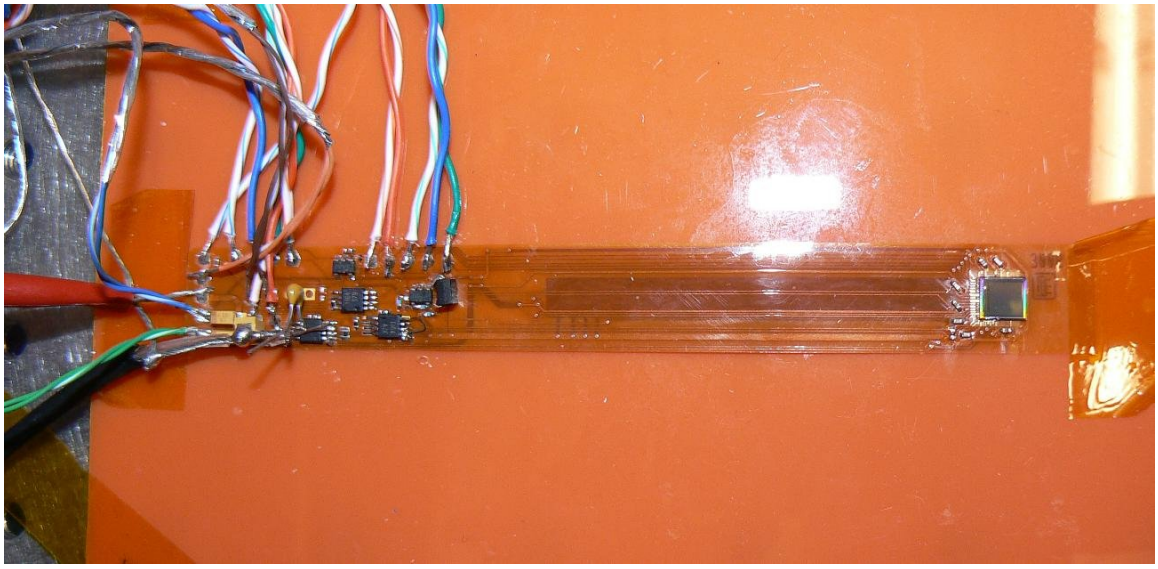

Figure 65: 25 µm Kapton flex cable with MIMOSTAR-2 sensor mounted and bonded. Three of these will be stacked to form a telescope.

Some significant effort is required to insert this telescope into the STAR experiment close to the interaction point. An insertion system, electronics control box and cooling system have been designed and fabricated. The basic system is shown in Figure 66.

In this diagram, the insertion tube that carries our telescope to a point near the interaction region is shown with respect to the STAR magnet pole tip. The electronics box is mounted in the hole in the pole tip above the beam pipe. Cooling is provided by a vacuum system that draws air past the MIMOSTAR-2 detectors through a tube that also carries our signal cables. The MIMOSTAR-2 detectors on their flex cables will be mounted into a positioning assembly (shown below) that will hold position and protect the telescope as it is slid into the insertion tube.

One can see that this test contains most all of the required firmware development and experiment interfaces required for both generations of detector.

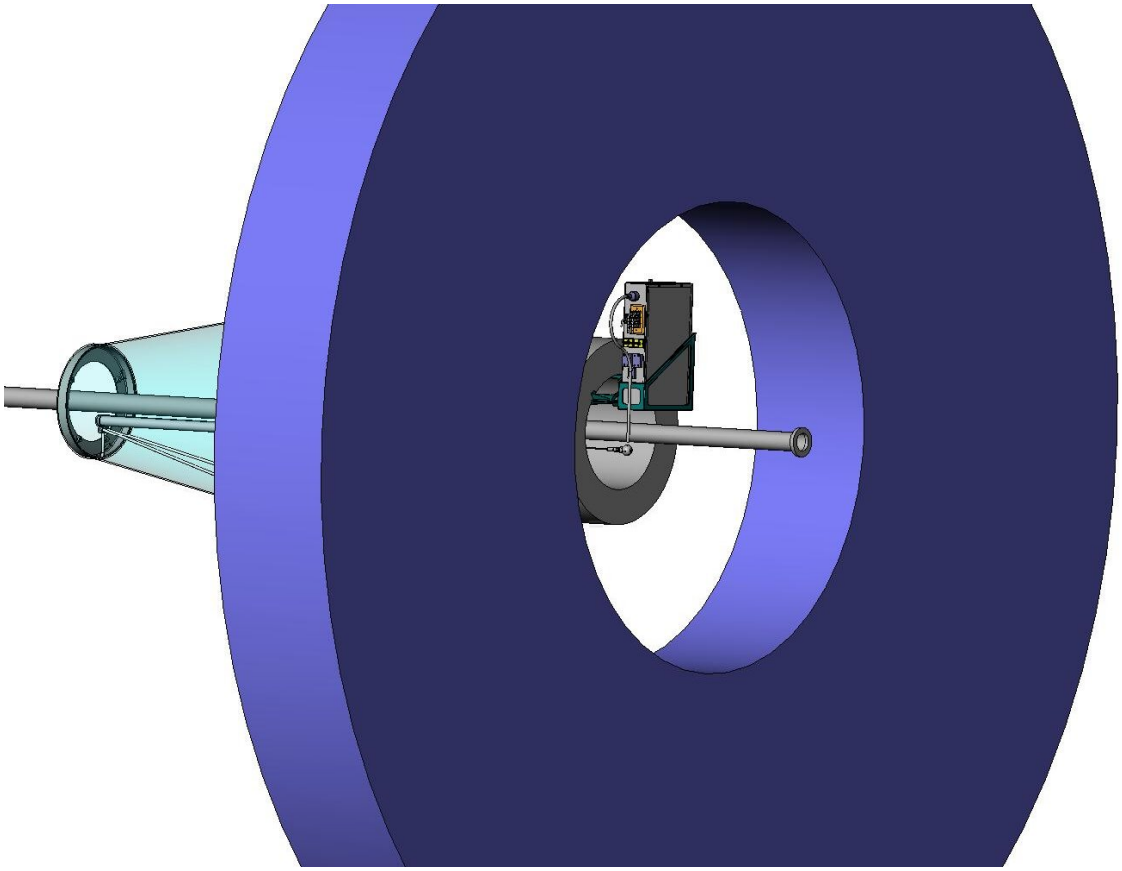

Figure 66: Solid model of telescope insertion system and electronics box position. The large blue toroid is the magnet endcap. The insertion tube is shown below the beampipe.

Figure 67: Telescope mechanical housing and positioning head. The MIMOSTAR-2 flex cables will be glued to the aluminum support and positioning brackets.

5 The Strip Detector (IST)

5.1 Overview

To reach its full physics capabilities, the Heavy Flavor Tracker requires tracks with good pointing resolution at its outer layer. TPC tracks alone provide a pointing resolution of around 1000 μm at the outer layer of the PIXEL. The existing SSD yields an improvement only in the r-ϕ direction because of its modest resolution in the z-direction. The SSD layer (at a radius of 23 cm) will be relatively far from the outer layer of the PIXEL (at a radius of about 7 cm), which is not optimal for the pointing resolution.

The Intermediate Silicon Tracker (IST) will provide space points with high accuracy in r-ϕ and z. The IST will consist of two concentric layers between the PIXEL and the SSD, as shown in Figure 17.

The IST will make use of a combination of standard silicon strip sensors and silicon striplet sensors. The striplet sensors will be very similar to the strip sensors but the strip length will be halved by an equatorial divide of the sensor to lower the double hit probability. Various technical details will draw to a large extend from previous experience on the design and operation of silicon tracker systems such as the PHOBOS silicon tracker stations. This project will make use of existing equipment and infrastructure from the PHOBOS silicon tracker through the MIT group.

5.2 Requirements

The following requirements are imposed on a new Intermediate-Silicon Tracker (IST):

Radii: The location of the IST layers is constrained by the outer radius of the Silicon Pixel Detector (PIXEL) and the inner radius of the STAR Silicon Strip Detector (SSD). The PIXEL will occupy space out to a radius of approximately 190 mm and the SSD occupies space down to a radius of approximately 190 mm. The most probable radii for the IST layers falls in the range from 120 to 180 mm.

Length: Tracking with the IST is intended to cover the pseudo-rapidity region of $-1<\eta<1$ with full coverage of the PIXEL and fair sampling of the vertex-distribution in STAR. At probable radii between 120 and 170 mm this implies active lengths of 400 to 520 mm.

Multiplicity: If the first layer of the IST is located at a radius of 120 mm then it will be subject to a particle flux of approximately 1 particle per square centimeter per central Au+Au at 200 GeV. This first layer should be capable of resolving these hits and, as a general rule of thumb, it is desirable to keep the occupancy below 10% .

Mass: The mass requirements for the IST are defined by the heavy ion physics requirements in the mid-rapidity region and by the *W*-boson spin physics program for more forward rapidities. The heavy ion vector meson program, going to di-electrons, is marginal given the existing mass of the SVT in the mid-rapidity region. Similarly, the upsilon program is marginal with the existing mass of the SVT. The IST should thus strive to be as thin or thinner than the current azimuthally averaged 4.5% radiation lengths of the SVT. The *W*-physics spin program is hindered by SVT support structures in the pseudo-rapidity region of $1<\eta<2$. Support structures for the IST should thus be designed to reduce mass in this region.

Thickness per layer: 1% to 1.5% radiation lengths per layer of Si has been routinely achieved by RHIC detectors. The STAR SVT is 1.5% radiation lengths thick per layer and the SSD is 1% radiation length thick when averaged over the full azimuthal range. A new tracker should strive to achieve a comparable or smaller thickness.

Pointing Accuracy: About 18 events will be piled up in the PIXEL with a 200 μs readout time at the anticipated RHICII luminosity of $90 \cdot 10^{26} cm^{-2} s^{-1}$ for Au+Au at 200 GeV. To keep the ghosting level below 5% a pointing resolution to the outer PIXEL of 170μm (1σ) is required.

Efficiency and purity: The proposed tracking layers should have a tracking efficiency and purity of tracks which is sufficient to do the expected physics programs within a reasonable running time.

Vertex resolution: The vertex resolution of the IST should be adequate to resolve displaced vertices from intermediate to large *B*-meson decays in 500 GeV p+p collisions.

Intrinsic sampling speed: The spin program at RHIC relies on individual beam bunch crossings to set and determine the relative spin orientations in the proton beams. The IST should be able to resolve individual beam bunches.

Rate capability: The IST should be able to handle the full RHIC-II peak luminosity of $90 \cdot 10^{26} cm^{-2} s^{-1}$ for Au+Au at 200 GeV and $4 \cdot 10^{32} cm^{-2} s^{-1}$ for p+p.

5.3 Proposed configuration

The Intermediate Silicon Tracker (IST) will consist of two concentric layers as shown in Figure 68. Each layer will be assembled from ladders. Since these ladders, most likely, will have to be glued together, they can be considered as the smallest building block of the IST. There will be two ladder types, their length determined by the layer they will be located in. Having the ladders only cover the rapidity range of interest is the most cost

effective solution, but 2 different ladders does complicate the production of the ladders. The inner ladders will carry one layer of silicon sensors with short strips. The outer ladders will carry 2 layers of silicon sensors arranged back to back. Radii, number of sensors per ladder and number of ladders per layer can be found in Table 19.

	Layer 1	Layer 2	Total
Radius [mm]	120	170	
No. of sensors per ladder	10	26	
No. Ladders	19	27	
No. Sensors per layer	190	702	1082
No. Readout chips	1900	3510	5410
No. Channels	243200	449280	692480

Table 19: Overview of IST layout parameters.

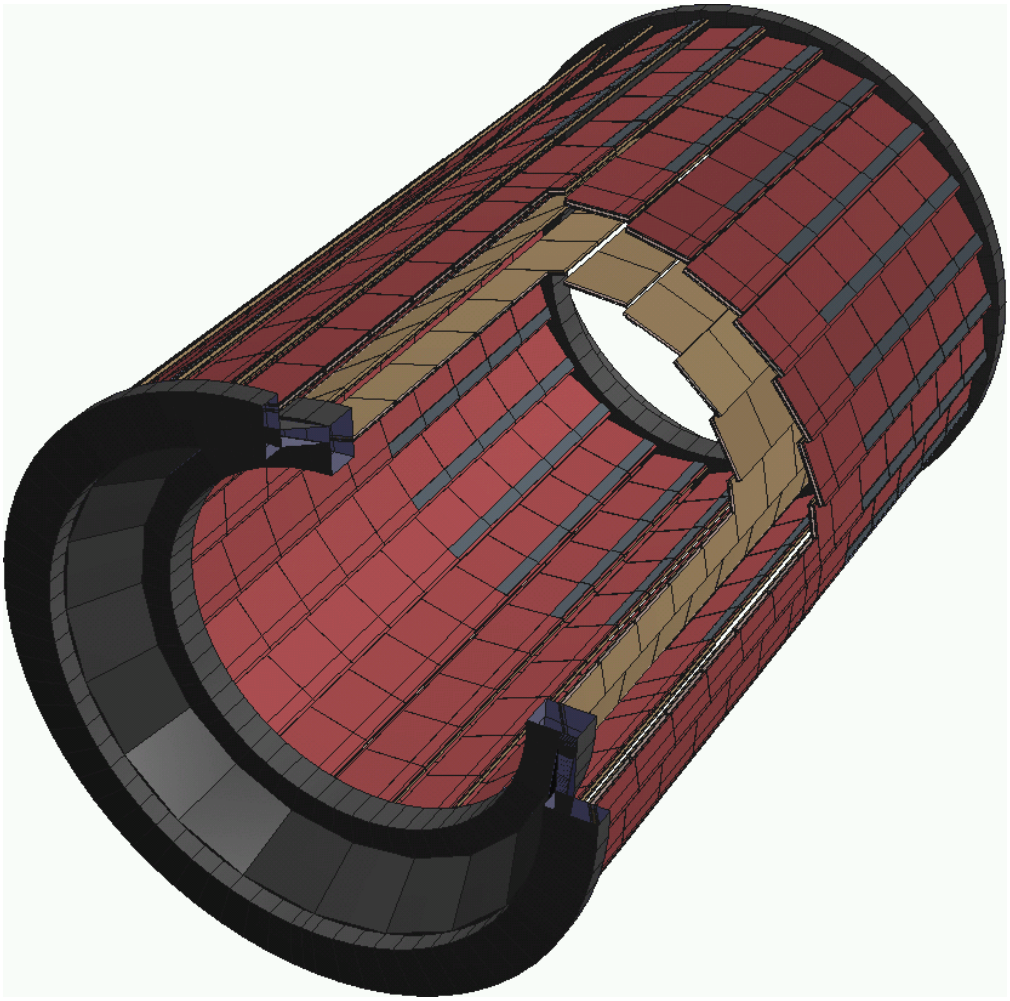

Figure 68: Geometry drawing of the two IST layers.

The anticipated material budget for the two IST layers is shown in Figure 69 and Figure 70. The top plots give the observed radiation length versus rapidity and averaged over ϕ. The bottom plots are for the radiation length versus ϕ at mid-rapidity. These results where obtained by propagating 100,000 geantinos through the IST geometry using GEANT 3.21/08. Care was taken to include a realistic estimate for the ladder material and readout cables. The support structures are simplified but should still give an adequate measure of the amount of material. Figure 71 gives the total material budget for the two layers of the IST. The asymmetry in the rapidity plots in Figure 69, Figure 70 and Figure 71 is caused by the readout cables all running in positive rapidity direction.

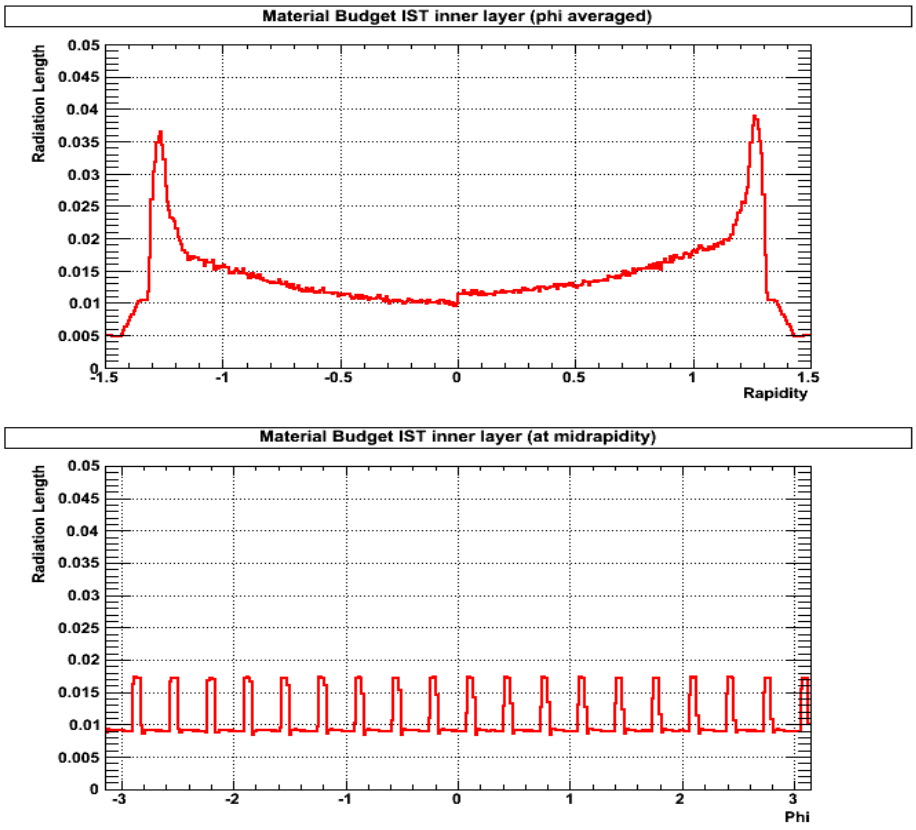

Figure 69: Material budget versus rapidity (top) and ϕ (bottom) for the inner layer of the IST.

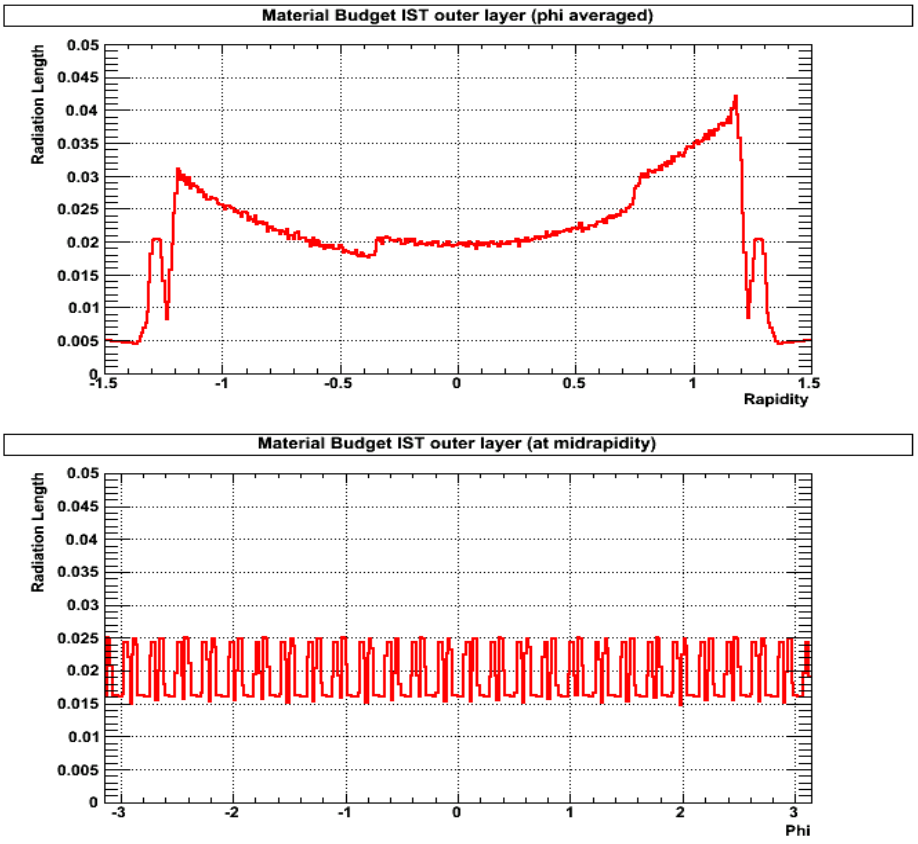

Figure 70: Material budget versus rapidity (top) and ϕ (bottom) for the outer layer of the IST.

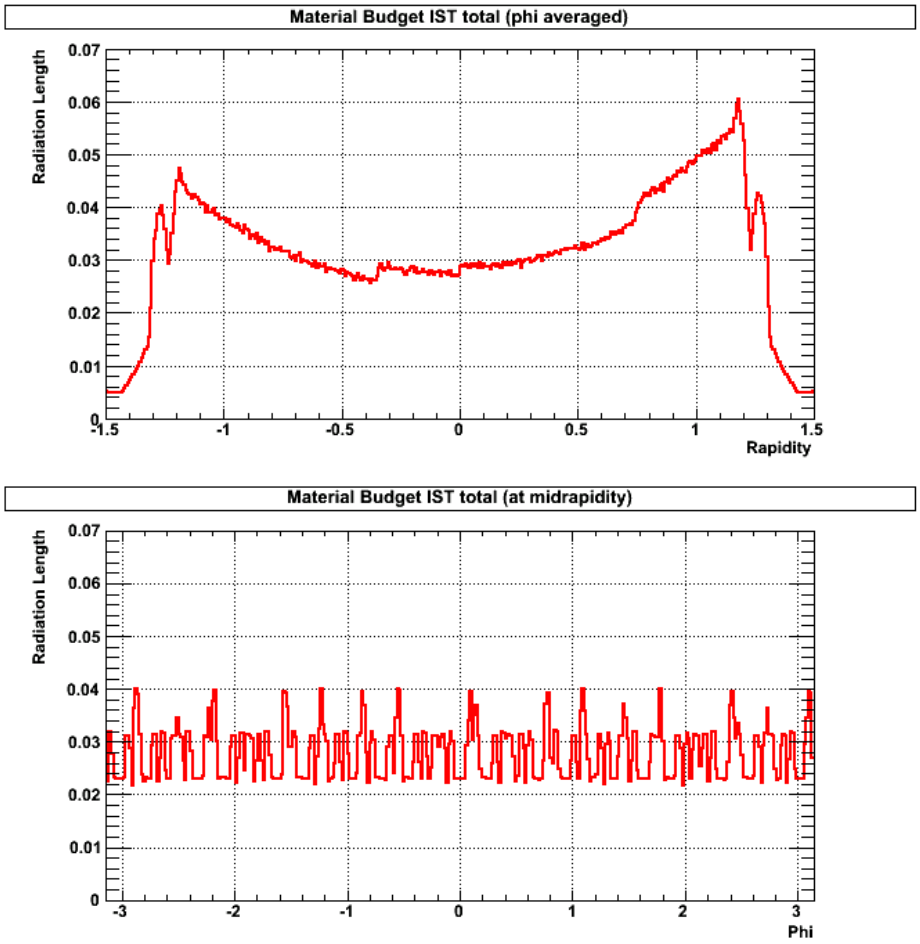

Figure 71: Total IST material budget versus rapidity (top) and ϕ (bottom).

5.4 Support structure

The support structure of the intermediate silicon tracker should be both mechanically stable and low mass. The amount of material in this structure will for a large part determine how its performance will be affected by non-desired processes like multiple scattering, conversions, delta rays and nuclear interactions. On the other hand it has to provide a mechanically and thermally stable support for the detector elements. To make it possible to carry out maintenance work and to accommodate a possible staged installation schedule, the structure also has to be highly modular.

It is foreseen that this support structure will have to support the 2 barrel layers of the intermediate silicon tracker, the 6 disks of the planned forward GEM tracker and that it will provide a high accuracy mechanical connection for the active pixel detector. It will also have to support the existing silicon strip barrel. However, it should be kept in mind

that the stiffness, accuracy and final cost of the structure will benefit from keeping its dimensions small.

The mechanical support structure should be made with an overall accuracy of 100μm, which is about the best accuracy which can be achieved for mechanical structures of this size. This overall accuracy will be sufficient to assemble the different parts of the system. Trying to improve on this accuracy would immediately drive up the cost. Locally the structure will have to be more accurate than 100μm. For instance, the mounting surfaces of the sensor modules will have to be flat to within 50μm to avoid stress, and possibly breakage, of the sensors.

The structure should also be thermally sound. It is not foreseen that the detector will be operated other than at room temperature, both during lab testing and while installed in STAR. However, there is always the chance of thermal excursions and the structure should be able to handle those. Preferably the thermal expansion coefficient should be zero. Where this can not be achieved, there should be enough slack to take up the expansion to avoid putting stress on components. For instance, sensor ladders can be mounted only rigidly on one side while the other side is seated in sapphire mounts which make longitudinal expansion possible. Also special care should be taken in the choice of adhesives and avoiding 'bimetal' effects during construction of the parts.

A structure made out of carbon fiber composites currently seems the most promising choice. Many groups are using this material to build highly accurate trackers. There is substantial experience, e.g. among the LHC experiments, that we can rely on when designing and building such a complex structure. It is clear that significant R&D is necessary to achieve a low mass system.

5.5 Silicon sensors

The most conservative choice for a silicon tracker is to use silicon strip sensors. The manufacturing techniques for these types of sensors are well established and are mastered by several manufacturers. Silicon strips have been and remain the first choice for most high energy experiment trackers.

The preference is to produce single sided devices with p^+ implants on n-bulk silicon and poly-silicon biased. They are relatively easy to produce with high yields and can also be handled without much difficulty in a standard semi-conductor lab. In contrast, double-sided devices have lower yields (so more expensive) and need special equipment to handle them. For matter of convenience we would prefer to have all sensors have the same dimensions and the same strip pitch of 60 μm.

Central Au+Au collisions at 200 GeV/c lead to a particle density of about 1 per cm^2 at the inner IST barrel near mid-rapidity. At the outer barrel the particle density will be a factor of 2 lower. For the outer barrel we are planning to use reasonably standard silicon strip sensors, i.e. with strips running over the whole length of the sensor. There will be two layers of silicon sensors in the outer barrel with the sensors mounted back-to-back on the ladders. The sensors on the outside of this barrel will have their strips running parallel to the beam-axis, so giving a good r-ϕ resolution. This orientation is the same as for the SSD and will provide redundancy. The sensors on the inside of the barrel will be identical to the ones on the outside but rotated by 90 degrees, which results in a good z resolution. The chosen sensor size of 4 x 4 cm^2 will give acceptable double hit probabilities for the outer barrel. Using the same sensors in the inner barrel would lead to unacceptable double hit levels. Therefore, we have decided to adapt the sensors of the outer barrel to the higher particle density by dividing the strips in half at the middle of the sensor. The resulting striplets will run parallel to the beam-axis and will give good r-ϕ resolution.

In total there will be two different sensor designs. Figure 72 shows the two designs for the strip and striplet in the intermediate silicon tracker (IST). From the manufacturing point of view all the designs under investigation are reasonably standard.

Preliminary discussions with Hamamatsu showed that they are able to make the outer barrel silicon strip designs we proposed to them within the proposed budget. We will need to contact them again to inquire after the price and feasibility of the proposed silicon striplet sensors.

Table 20 provides information about the sensors that are needed.

	IST strip	IST striplet
Number of sensors	702	190
Die size [mm^2]	40 x 40	40 x 40
Number of channels	640	1280

Table 20: The characteristics of the silicon sensors needed for the IST.

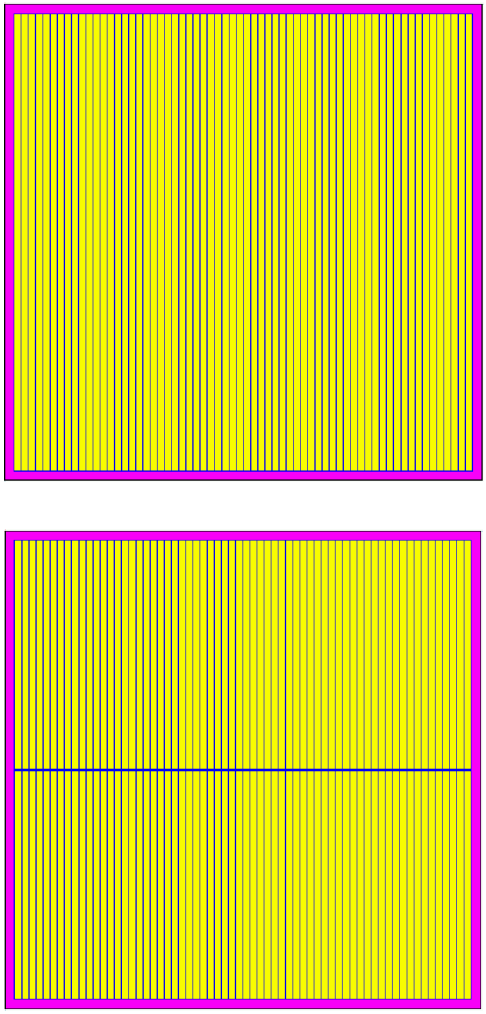

Figure 72: Sketch of the IST silicon strip (top) and striplet (bottom) sensors.

5.6 Ladders and cooling system

A substantial amount of R&D will have to go in developing a low mass and stable ladder structure on which the silicon sensors can be mounted. The best candidate for the ladder material seems to be a thermally conductive carbon foam developed by Oak Ridge National Laboratory. It combines a very low density to high strength and a thermal conductivity close to that of Aluminum.

The inner layer of the tracking system will dissipate about 3 Watt per sensor assuming 10 APV25-S2 readout chips per sensor. Since the radiation levels are not an issue the system can be kept at room temperature, this avoids problems with condensation and makes maintenance of the system much less complicated.

The current R&D focuses on using air cooling channels through a ladder made out of the thermally conductive carbon foam. By internally shaping the cooling channels an increased turbulence will make the cooling more efficient than just blowing air over the sensors.

5.7 Dry air system

It is preferable to keep the ladders and especially the sensors of the IST in a low humidity environment. We propose to copy the PHOBOS dry air system which has kept the PHOBOS silicon system at about 10% relative humidity for the duration of the PHOBOS operation. This is a very simple system which boils off liquid nitrogen from a supply tank and feeds it into the almost airtight enclosure of the PHOBOS silicon system. The flow is just enough to maintain a slight overpressure in the enclosure to keep the higher humidity air from the experimental area out of the system. The pressure is regulated by one valve which provides just enough nitrogen boil off to maintain the required overpressure. The system has proven to be very reliable.

5.8 Front-end electronics and DAQ system

The current best estimate is that there will be about 700,000 channels to be read out in the IST. Designing and producing specialized readout chips for this system is not feasible because of the lack of time and manpower. For the sake of expedience it was decided to try to find a readout chip which was already being used for similar purposes by other experiments.

The best candidate so far is the APV25-S1 readout chip which was designed for the CMS silicon tracker and of which about 75,000 will be used in CMS. Each channel of the APV25-S1 chip consists of a charge sensitive amplifier whose output signal is sampled at 40MHz which accounts for the LHC interaction rate. The samples are stored in a $4\mu s$ deep analogue pipeline. Following a trigger the data in the pipeline can be processed by an analogue circuit, mainly de-convoluting the amplifier response from the actual signal and associating the signal with a certain interaction (or rather beam crossing at LHC). The resulting analogue data can then be multiplexed and send to digitizer boards. Although the analogue data leads to higher data volumes at the front-end, it is an enormous advantage that charge sharing between strips and common mode noise can be studied in detail, which will greatly improve the understanding and performance of the detector. The Equivalent Noise Charge (ENC) of the APV25-S1 depends on the capacitance of the strips and the de-convolution algorithm used, but, for our purposes, it will be better than 2000 electrons. With $300\mu m$ thick silicon sensors this will give a signal-to-noise ratio of better than 11:1 when we take the most probably energy deposition by a Minimum Ionizing Particle (MIP). The power consumption of the

APV25-S1 is about 2 mW/channel, i.e. about 0.25 Watt/chip. The chips are fabricated in the radiation hard deep sub-micron (0.25μm) process. Figure 73 shows a close-up of the APV25-S1 chip.

A prototype readout system for the APV25-S1 chips has been designed and is currently being tested. This is part of the triple-GEM prototype effort. More details on the overall readout system will be presented in Section 5.14.

The STAR radiation environment will be less harsh than that of CMS, it could well be that the front-end digitizers can be located much closer to the detector and that there is no need for 100 meter long analogue optical links. The preference is that the readout system of the silicon system will be the same as for of the forward GEM system, which is also utilizing the APV25-S1 readout chip. Considering that about 900,000 analogue channels have to be digitized there is probably also the need for a zero suppression system as part of the readout system.

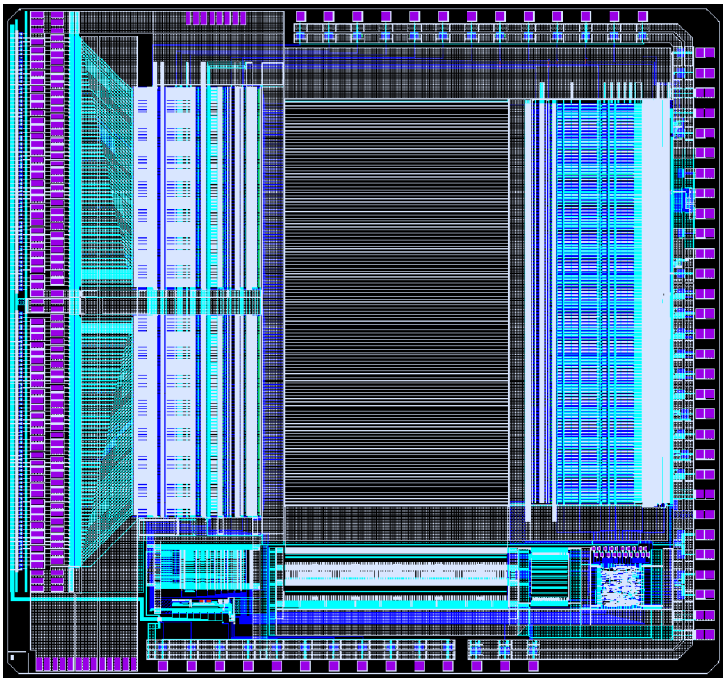

Figure 73: Picture of the APV25-S1 die. On the left are the input pads, on the right the output pads, control pads, etcetera are visible. The whole die measures 8055 by 7100 μm^2.

5.9 Flex cable / hybrid

To keep the material budget as low as possible a new kapton cable/hybrid cable is under investigation. This flexible cable combines the hybrid, which carries the readout chips, with the long readout cable. This cable will be made out of kapton with a total thickness of about 100µm. The hybrid end will be glued down on the sensor, the other end plugs into the a readout unit which will be located just outside of the central TPC area. Figure 74 shows one of the prototype cables which are currently being used for building an IST prototype module.

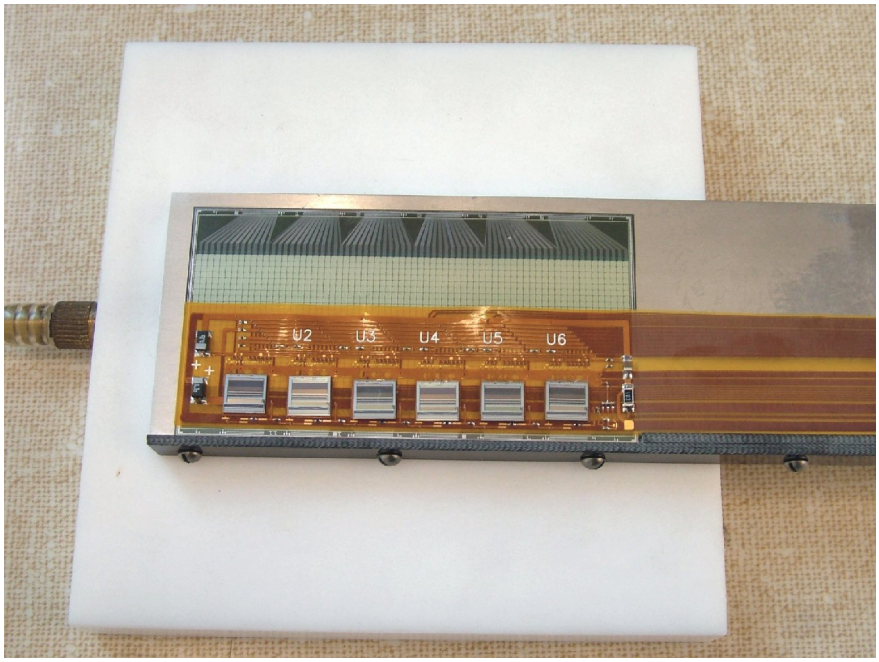

Figure 74: Prototype cable/hybrid, equipped with readout chips and mounted on a Type 1 PHOBOS silicon pad sensor.

5.10 High-voltage and low-voltage system

Considering the standard requirements both for the high voltage and low voltage system, the hardware can likely be obtained as almost off the shelf components. Since these systems will be located relatively close to the detector there is the need for remote control and monitoring. Companies like Wiener can build these systems to the desired specifications, including a CANBUS interface.

5.11 Alignment system

The final alignment of the inner silicon tracker will have to be done by tracks. Usually this is done through an iterative residual method. For this method to work the positions of the strips will have to be known with an accuracy comparable to their width, i.e. 60μm, which is going to be very challenging.

Finding the position of each detector element on a ladder is relatively straightforward. An optical surveying system, which is available at MIT, makes it possible to do this with an accuracy of about 10 μm in the plane of the sensors and about 50 μm to 100 μm perpendicular to the plane of the sensors.

While the ladders are being assembled into barrel layers the next survey step has to be taken. It is very unlikely that the MIT optical surveying station will be able to handle the size of the assembled barrel layers. Logistically it is preferable that the barrel assembly takes place at BNL to avoid shipping of these vulnerable structures from another place to BNL. The optical survey station and touch probe system which were used for the STAR SVT should be able to determine the ladder positions within the inner barrel structure with an accuracy of 50μm or better. The assembly will then have to take place in 3 stages. First the inner most layer will have to be put together and then surveyed. Then the same needs to be done for the second and then the third layer.

The whole structure has to be stiff enough to retain the surveyed positions after installation in the STAR magnet. A system with very accurate positioning pins and surfaces will be needed to position the whole system with respect to the Heavy Flavor Tracker.

5.12 Slow control systems

A slow control system has to measure all working parameters of the intermediate and forward silicon tracker. The temperature of the hybrids and the currents and voltages of the components on the hybrids need to be monitored continuously. Also cooling water temperatures and water flow rates and dry air flow rates need to be recorded regularly. Preferably all these monitoring values get entered into a database. In case that the parameters get out of predefined operating values alarms should be send to the shift crew and interlocks should be activated if necessary.

Although STAR is using EPICS as its standard slow control system there is a slight preference to use LabView instead. LabView provides the user with virtually any instrument driver and has a very convenient user interface. LabView runs on both Windows and Linux. It is relatively simple to interface LabView and EPICS. However, at the moment, both options are still open.

5.13 Installation procedures

It is foreseen to assemble the complete inner tracking system including a new beam pipe outside, e.g. in the STAR experimental hall. This should include a system test using a cosmic ray test setup. This would also allow to test the integration into the STAR DAQ system at the same time. This step has been proven by many experiments as a critical step for a successful operation after installation. After completion of a complete system test, the inner tracking system including a new beam pipe would be then installed as one unit inside STAR.

5.14 Readout system

A prototype readout system has been completed adapted to the STAR Forward-GEM Tracker (FGT) upgrade project. The readout chip is identical to the IST. The readout system following the chip front-end electronics is expected to be rather similar to the FGT system. The following section provides a brief description of the prototype and setup and the anticipated readout system integrated into the STAR DAQ environment.

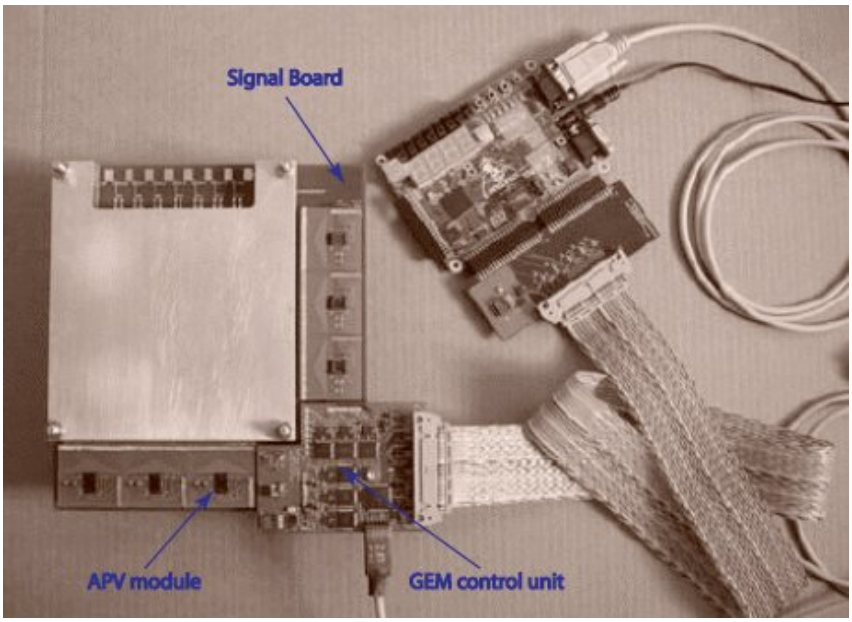

Figure 75: Prototype APV25-S1 readout system adapted to the STAR Forward-GEM Tracker (FGT) prototype chamber. The location of the APV module, GEM control unit and signal board is indicated.

Data from the 2D triple-GEM detectors are read out by the APV25-S1 readout system which consists of the following components:

- Signal Boards
- APV Module
- GEM Control Unit

The signal board collects the charge from the detector on a two dimensional strip pattern connected. The boards are fabricated from FR4 as a regular double sided 62mil PC (Printed Circuits) board which has a 50 μm thick Kapton foil glued on top which in turn is covered by 5 μm thick and 508 μm wide sensor strips on the bottom and 5μm thick and 127 μm wide sensor strips on the top side in the case of the prototype detectors. Kapton material between top strips is removed through laser etching to uncover the bottom strips which are then gold plated. Signal strips have a 635 μm pitch. The top strips are perpendicular to the bottom strips to form a two dimensional readout board. Each signal strip is connected to the bottom side of the signal board through vias connections and to 635 μm pitch SAMTEC connectors. Those provide then the connections to the APV module.

There are two sets of SAMTEC connectors, one for the X and one for the Y direction. The signal board also has two sets of an integrated bus system as part of the communication and data collection between the APV module and GEM control unit.

For the final disk design of the detectors the geometry of the readout structure has to be adapted to the detector geometry. The fabrication process of the boards will be the same as for the prototype detectors, however a lower mass construction will be used. Figure \ref{fig:ReadoutStrips} shows a schematic sketch of the readout geometry of the disk detectors, using a two dimensional strip readout with strips in the r and ϕ direction. The strip pitch is around 400 μm on both coordinates. The exact geometry and implementation of the final signal board is still under investigation. The total number of readout channels for the 6 disk FGT will be around 67,000, requiring the use of approximately 550 APV25-S1 frontend chips.

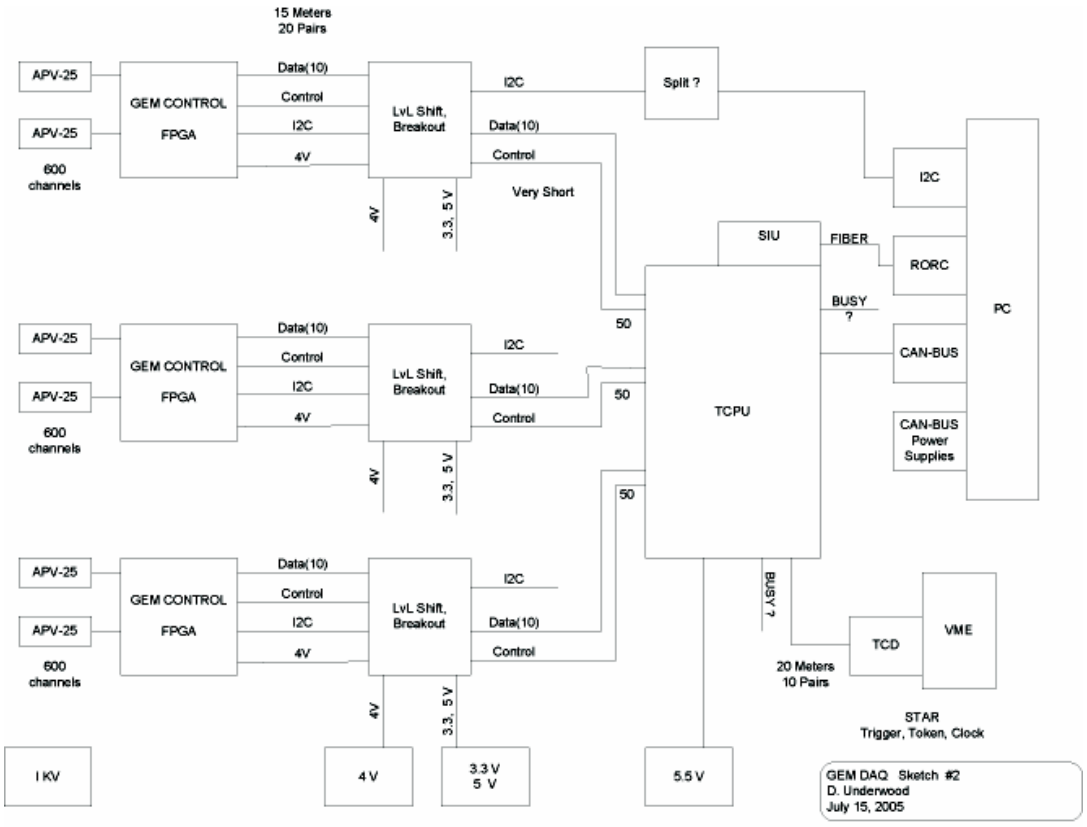

Figure 76: Sketch of the APV25 chip readout system and STAR DAQ integration.

The APV module in the prototype version has an on-board glued APV25-S1 chip which is fabricated in submicron process (0.250 micron) and is connected to 68 sensor channels. There is one set of APV modules for the X-direction and a separate set for the Y-Dimension. In the prototype version of the APV modules, each APV module is connected to 68 channels. In the final version each APV module will be connected to 128 channels and will have ADC and FIFO on board. The length of the data acquisition path will be less then $5\,$mm, which will guarantee minimum pickup noise. In our case, the APV25-S1 chip is operated with a clock frequency of 40MHz and read out with 20MHz. The APV25-S1 chip is set up using the I2C Philips Standard. Calibration pulses can be generated directly onboard to feed each channel.

The GEM Control Unit is the main control system for the 2D GEM readout electronics which controls all ADC, FIFO, and Data formatting and keeps communication between APV25 Modules and DAQ system. A Xilinx CPLD is the heart of each GEM Control Unit. This Xilinx component is fabricated in very deep submicron process (0.095 micron). In radiation tests which were carried out at Bates Linear Accelerator Laboratory, it was found that radiation hardness of the Xilinx CPLD component is beyond 1MRad.

The advantage of the Xilinx CPLD is based on the flexibility in re-programming to any desired configuration. Each GEM Control Unit contains for each APV25-S1 an ADC and a FIFO, where the ADC is continuously running and converting incoming signals from the APV25-S1. Upon a positive trigger decision, the data are then converted and written in parallel into all FIFOs and then in sequence from FIFO by FIFO these data are sent out in LVDS standard to the STAR DAQ system. These actions are controlled by the Xilinx CPLD device which is programmed in VHDL language. The GEM Control Unit is connected with the outside environment only through one twenty wire pairs flat ribbon cable. Each GEM Control Unit has all required voltage regulators on board. The power distribution requires therefore only one +4V power supply using one wire pair. The signal board, APV25 module and GEM control unit form one compact unit without cables and wires. All connections are realized through PC board printed layer connections. This guarantees that this system will have very low noise.

We have already made good progress in integrating the APV25 readout into the STAR environment. We have a prototype system which utilizes the STAR Trigger and Token distribution through the TCD module, and also reads out the data using an ALICE DDL link, as will be used in STAR TOF and future upgrades. This prototype system was constructed by modifying an Altera Stratix FPGA based controller, called a TCPU, developed for the STAR Time of Flight, and by adding some interfacing for the MIT GEM controller, and other systems such as I2C for the APV25, and Canbus for the Stratix TCPU board.

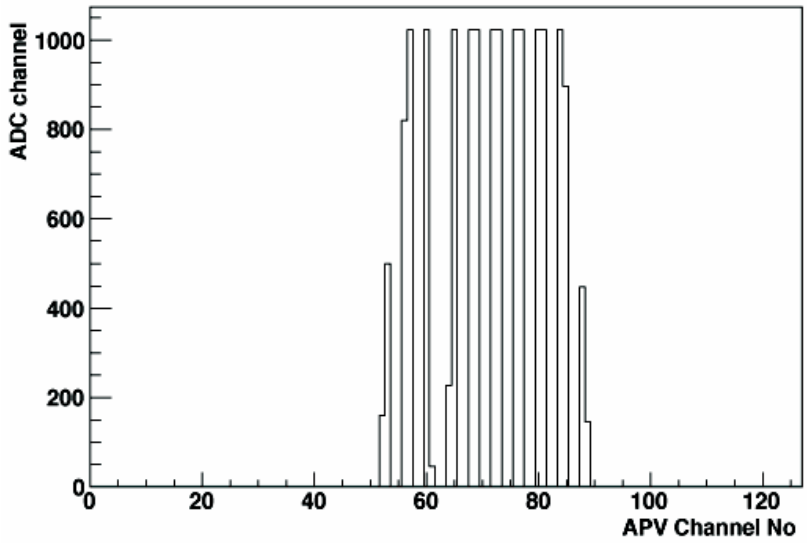

Figure 77: Cosmic muon pulse in a small RPC recorded with the APV25S1 chip and the full DAQ chain. The two on -- two off structure is due to the connection scheme of the APV chip, where only half of the channels are connected to readout strips.

The prototype system, shown schematically in Figure Figure 75, was successfully tested with a small resistive plate chamber with cosmic muons. Figure Figure 77 shows one of the events recorded with that setup. The signals in the RPC are much wider than they will be in GEM detectors since the signal pick-up is inductive compared to direct electron collection in a triple GEM device. RPC signals are also much higher, apparent from the fact that most channels reach saturation. While a the charge of a RPC signal is typically between 0.2 pC and 2 pC, a MIP signal in a triple GEM detector is around 10 fC. Nevertheless, these results demonstrate that the full readout chain from the front-end chip to the data acquisition is working as expected.

For tests with a small number of detectors in a low rate environment a USB based readout system for the APV25 and GEM Control Unit is currently being developed. This system allows to install test setups at several locations at low cost, and will be used for GEM detector tests with cosmic muons. The DAQ software for this system is based on LabView and can be run on a standard PC or laptop computer.

6 Integration with STAR

6.1 Mechanical

The current inner region of STAR is designed to accomodate the SSD and the SVT. The employed structure consists of two symmtric cones supproting the SSD at the large radius, and the thick SVT at closer radia. With the HFT and PIXEL detector a new concept, that minimizes the material in the inner region, and incoorporates means of allowing for precise relative positioning will be implemented.

6.2 Beam Pipe

The vertex detector extends the measurement radius to 25 mm from the interaction axis and will require a new small radius beam pipe for STAR. The design concept for this pipe is shown in Figure 78.

Figure 78: Beam pipe.

The beam pipe is constructed from 60 mm diameter aluminum tubes that taper down to a 40 mm diameter beryllium beam pipe with 1 mm thick walls. The central region where the HFT is located is a 40 mm diameter beryllium pipe with a 0.5 mm thick wall. The beam pipe is supported in the center with the same shell that cares the pixel detector. The shell provides gravitational support as well as isolating the thin central region from handling stresses from the long extended pipe. The central support is shown in Figure 79 (I lost this figure ??). The outer shell has been made transparent in the figure to show the inner structure.

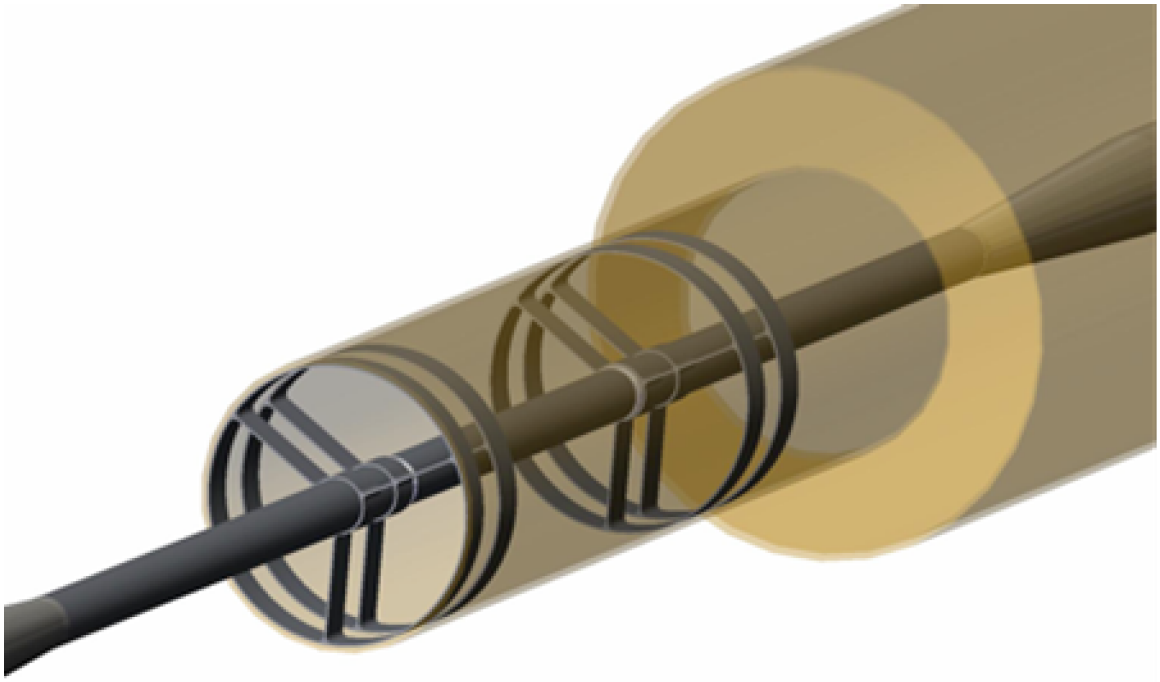

Figure 79: View of the beampipe mid-section with central support.

6.2.1 Minimum Beam Pipe Radius Consistent with Injected Beam and Larger than the Limiting Aperture

We have chosen a minimum radius for the beam pipe which, now that the RHIC optics has stabilized, is reasonable conservative. From the standpoint of beam pipe interaction with beam optics, the beam pipe wall should, according to accelerator physicists at BNL, have a minimum radius of 6 σ while 10 σ is very conservative[146]. σ is the beam envelope at injection. For STAR at injection the beam emittance is 15 π mrad·mm, β^* is 10 m, $\beta\gamma$ is 10.52 which gives σ = 1.5 mm plus a 5 mm beam offset at injection[146,147,148,149]. For protons injection σ is smaller and therefore less of a constraint. We have chosen an inner beam pipe radius of 20 mm or ~ 10 σ. This is satisfactory for RHIC operation, and it is larger than the limiting aperture, leaving the pixel detector clear of uncontrolled beam dumps[149].

6.2.2 Beam Pipe Radius - Vacuum Considerations

The dimensions of the beam pipe sets limits on pumping speed and the expected pressure at the center of the interaction region in STAR. The 1700 mm long central section with a 40 mm diameter joins a larger 80 mm diameter pipe, which extends 4000 mm to the pumping section. A simple analysis was performed[150,151,152] which gives a pressure increase at the center in the interaction region of ~ 10^{-11} torr. This is the pressure increase above the pressure at the pumping station and it is based on a surface out-gassing rate of

5.3×10^{-11} W/m^2 and a conservative estimate of the pipe conductance[151]. This is well within the requirements. The greatest uncertainty in this estimate is the out-gassing rate, but a factor of 10 greater value is still tolerable. If an Active NEG coating is used the inner section will be a pumping surface rather than an out gassing surface.

6.2.3 Supporting Section

The support barrel which carries the pixel detector and supports the beam pipe through the spoke structure shown **in Figureabove**. This support provides mechanical isolation of the central thin section of the beam pipe such that it carries only the load of the vacuum and is not subjected to forces from loads on the rest of the beam pipe. The spokes that couple the beam pipe to the outer support barrel allow insertion of the vertex detector into the center region. The end view in Figure 80 shows how the detector ladders mesh inside the support spokes providing hermetic overlap of the detector elements. The detector modules move to a larger radius during insertion to clear the spokes.

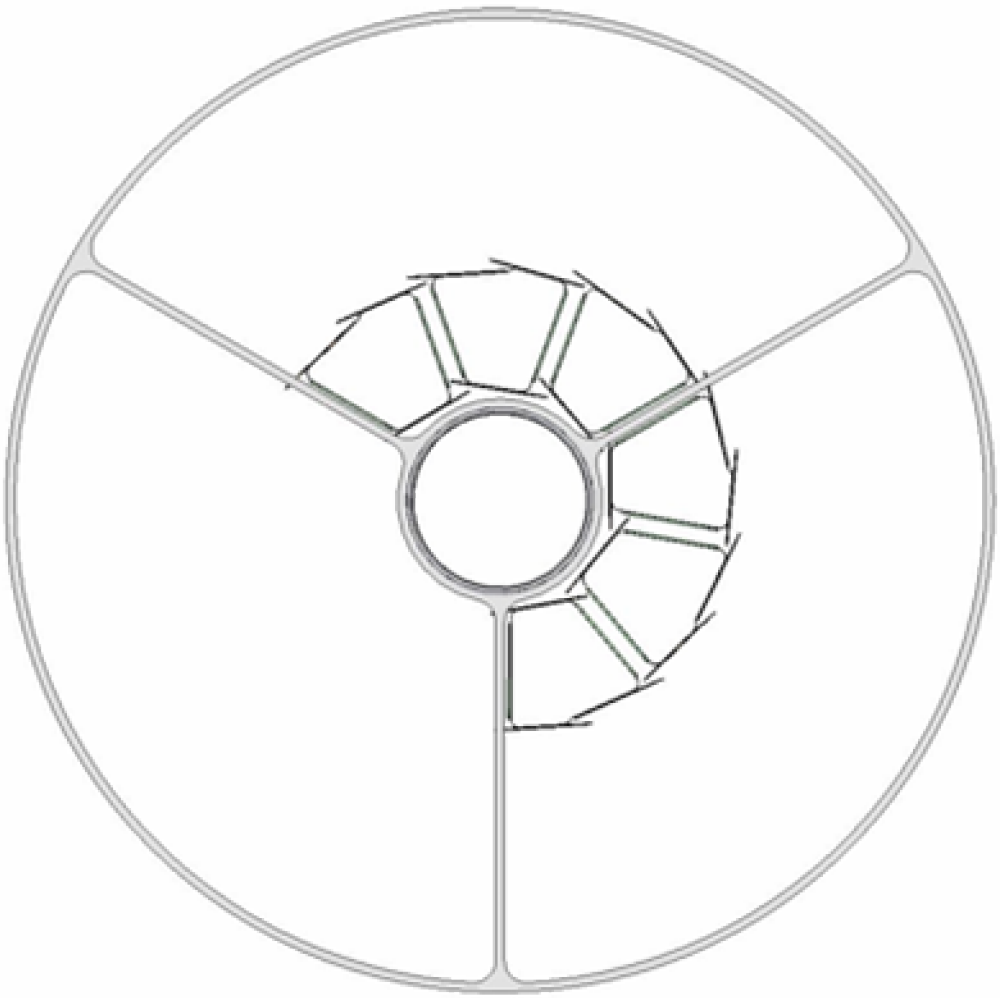

Figure 80: End view showing the pixel ladders between the spokes of the inner beam pipe support. Two out of three of the detector modules are shown.

6.2.4 Central Beam Pipe Thin Window Section

The current plan for the thin central region is to use a beryllium pipe with a 0.5 mm wall thickness. It is believed that this will provide the minimum coulomb scattering while maintaining a reasonable structural safety margin. Preliminary analysis indicates a 50:1 safety margin for buckling[153]. There is a structure failure limit imposed by the degree of roundness of the cylinder. A stress analysis indicates that a 1 mm deviation from a cylinder (1 mm difference between major and minor axis of an ellipse) sets a 20:1 safety margin for material failure.

6.2.5 RF Background from the Wake Field

It is believed that the beam pipe in STAR will be sufficient to suppress wake field signals in the detector to well below the expected signal. The evidence for this belief comes from experience with the gas jet polarimeter and carbon strip polarimeter located at the 12 o'clock intersection region of RHIC. These polarimeters have silicon detectors located inside the beam pipe close to the beam and it has been found that a few microns of conductor are sufficient to shield these detectors from the wake field[154].

The PIXEL will be located outside the beam pipe and will benefit from the RF shielding this pipe provides. The pipe will be constructed from at least 500 microns of beryllium. The maximum beam in RHIC will be 1×10^9 gold ions per bunch. This gives a wake field current of 110 mA (counting both beams), which with a 1 μm skin depth will generate a resistive potential drop of only 7 mV. A more sophisticated calculation should include induction, rise time and skin depth and detector filtering, since our bandwidth cutoff will be closer to the wake field GHz frequency than the polarimeter detector cutoff.

6.2.6 Beam Pipe Insertion and Removal

We are currently investigating the removal and insertion of the beampipe. We anticipate replacing the current center section of the STAR beampipe with the components described above. This will likely entail a period of refit and installation to install the new beampipe after which removal and reinsertion should not be necessary during the normal course of running and detector repair.

6.2.7 Bake Out

Beam pipe bake out is still under discussion. It is expected that the same form of NEG coating will be used and there are two possibilities in how this will be treated. It may either be a minimum bake out to remove primarily water as it is done now with a hot dry nitrogen scrub gas at 150 C to 110 C or it could be a full activation of the NEG coating turning it into a pumping surface[155]. This later case requires baking at 150 C to 200 C with vacuum. This could impose additional constraints on beam pipe materials and would require additional thermal isolation from the other detectors. If it is decided that the less aggressive bake out procedure is adequate then carbon composites can be used in the construction of the beam pipe support spokes. In either case the pixel detector will be withdrawn during bake out from the operating location to isolate it from the heated beam pipe.

6.3 Compatibility with the SSD and other cone mounted detectors

The pixel detector will be supported and installed from one end only. There will be no other detectors requiring support or access at this end. Other detectors requiring cone support will be outside of the pixel space. The FTPC on one end will have to be removed to accommodate the pixel detector and support electronics as shown in Figure 43.

6.4 Compatibility with an Upgraded Inner Si Tracker Barrel

The SVT will be replaced with the new silicon strip barrels and forward disks . The support structure for the new tracker will be installed from one end of STAR and the pixel detector will be supported and installed from the opposite end.

7 Preliminary Cost and Schedule Estimates

7.1 Cost and Schedule

The HFT is a very demanding technical project and it requires a substantial amount of R&D in order to ensure that it will be ready to take data when RHIC is running. The enclosed cost and schedule estimates reflects the need to develop and test the pixel sensors over a period of several years. We envision at least four generations of chips before we have a full sized, production quality, chip design. The cost and schedule also reflects the need for replacement parts so that the detector can be easily repaired during a run.

Synchronizing with the RHIC run schedule is beyond the scope of this document, but it is an important topic none-the-less because a successful HFT program requires several years of running, including (as a minimal set) a high statistics top energy Au-Au run, a p-p run, and a d-Au run. Since the RHIC schedule is hard to predict, it is very important that the HFT be ready on time, and be reliable during each run. The number of opportunities to run top energy Au-Au beams are very limited. Therefore, we have designed the HFT to be easily repaired during a run and even replaced, if necessary.

A schematic overview of the proposed R&D and construction schedule is shown in Figure 81 with particular emphasis on the installation dates. Note, for example, that the figure includes a milestone for the installation of a detector telescope based on MimoSTAR II chips in the summer of '06. The detector telescope will take data in FY07 with the goal of testing the APS chip technology under working conditions at the STAR experiment. Additional installation activities are shown in each year. A more detailed roll-up of the projects activities is shown in **Figure 82**.

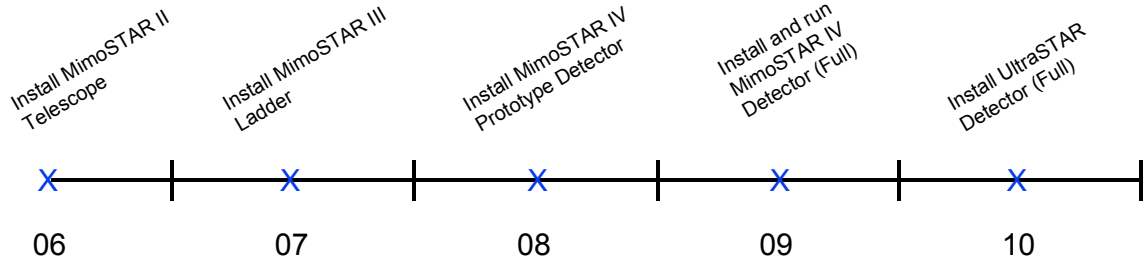

Figure 81: A Schematic view of the installation activities in each year. Installation is typically done in the summer of each year.

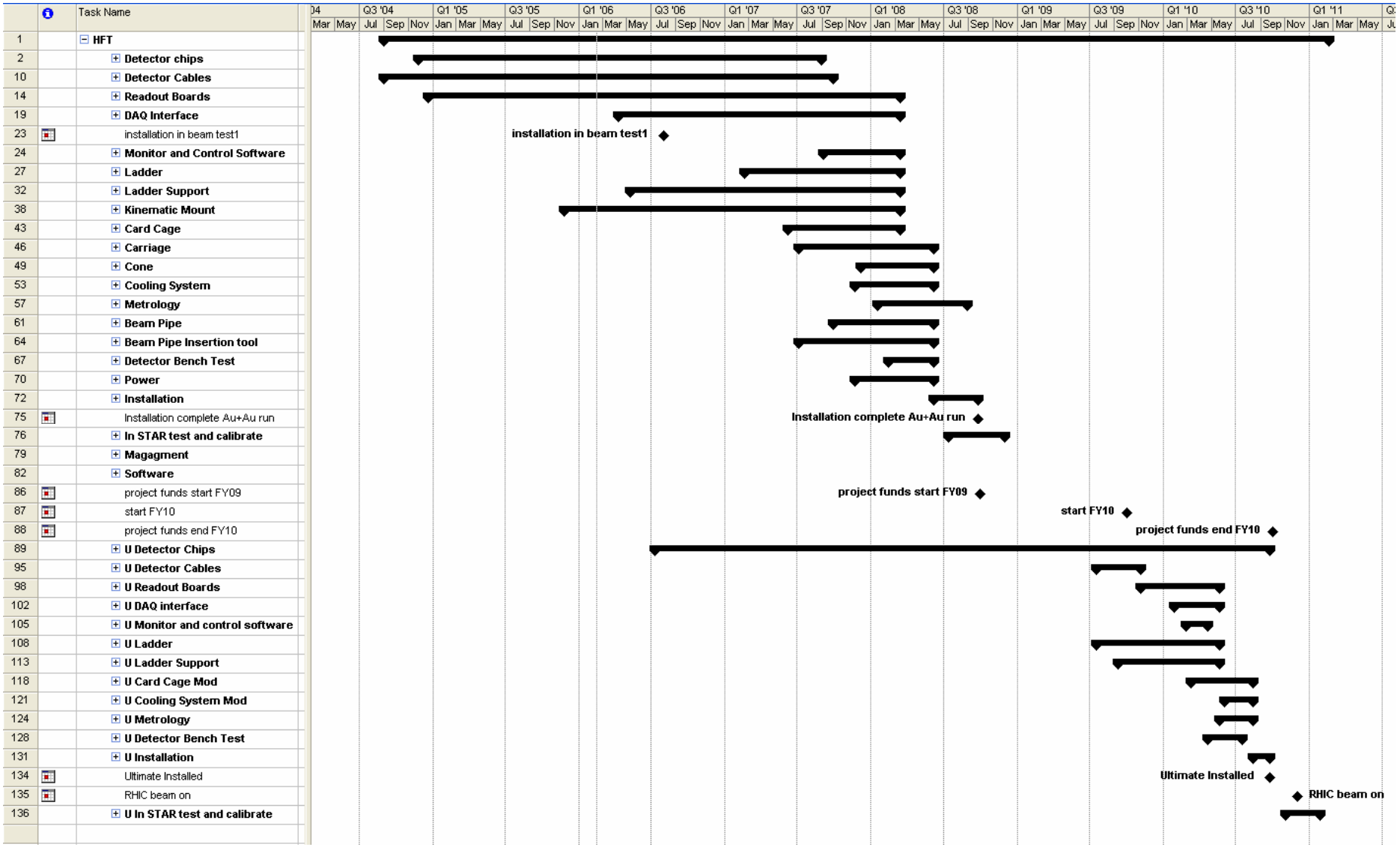

Figure 82: Schedule overview and roll-up of activities.

A full Micro-Softsoft-Project model for the HFT project has been developed and the files are available on the WWW. The files are too complex to be included in this document but an extract of one of these files is shown in Figure 83.

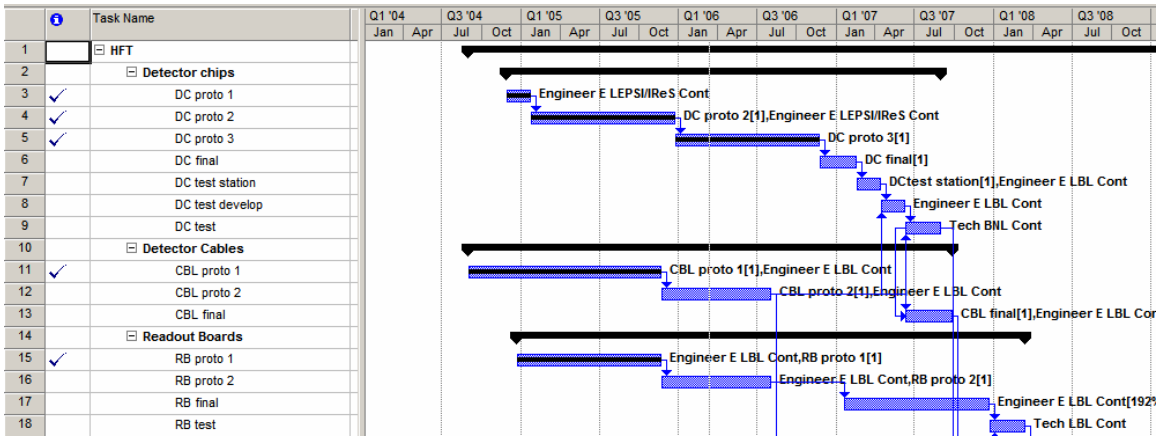

Figure 83: Detail from the Gantt Chart that tracks the full enterprise of HFT activities.

The HFT requires a substantial amount of R&D work due to the innovative new technology that is an integral part of the project. The items needing further development include the Si chips, the readout and DAQ electronics, the mechanical arms to hold and insert the detector, the beam pipe, and the calibration and tracking software. The R&D activities will begin in FY06 but the bulk of the R&D activities will take place in FY07 and FY08. During FY06, the engineering labor will be contributed by the Berkeley Lab, while in FY07 and 08, we anticipate that one mechanical engineer and one electrical engineer will be funded by the R&D dollars associated with the HFT project.

The contributed engineering estimates shown in the tables, below, have not been negotiated with LBNL or BNL management and are subject to further refinement and the availability of funds.

Significant R&D activities to be studied in FY06 include:

- QA and test of MimoSTAR II chips from Strasbourg
- Conceptual design of readout boards for the Strasbourg chips
- Prototype ladders to support the chips
- DAQ interface prototype
- Develop Al clad cable technology
- Conceptual design of the kinematic mounts to hold the ladders
- Live beam tests in STAR using MimoSTAR II chip
- R&D for the MimoSTAR III chip

Estimated expenses in FY06:

- ~150 K Procurements
- ~150 K Engineering
- ~500 K Contributed Engineering

Significant R&D activities to be studied in FY07 include:

- QA and test of MimoSTAR III chips from Strasbourg
- Prototype readout boards for the Strasbourg chips
- Prototype ladders to support the chips
- Conceptual design of the kinematic mounts to hold the ladders
- Live beam tests in STAR using MimoSTAR II chips
- Collaborative design of the beam pipe
- One prototype IST module showing the basic functionality of the combination of a silicon sensor, APV25-S1 readout chip and readout system
- A prototype IST ladder showing the feasibility of a carbon foam design and air-cooling.
- Well defined plan for the FY2008 mechanical integration research established.

Estimated R&D expenses in FY07:

- Pixel ~670 K Procurements, IST ~61 K Procurements: Total 731K
- Pixel ~250 K Engineering, IST ~230K Engineering: Total 480K
- Pixel ~1000 K Contributed Engineering, IST ~ XXXK Contributed Engineering: Total
- Total R&D funds ~1,211K Project and XXXK Contributed

Significant activities to be studied in FY08 include:

- QA and test of the MimoSTAR IV chips from Strasbourg
- Live beam tests in STAR using MimoSTAR III and prototype kinematic mounts
- Integration studies for the support of the HFT and Cone modifications
- Development of alignment and calibration techniques
- Design and test of the thin walled beam pipe and analysis of risk
- Develop and test interface to STAR DAQ
- R&D for the UltraSTAR Chip

- One, possibly two IST ladders equipped with several readout modules to install in STAR.
- Base zero-suppression system showing readout of IST prototype ladders, zero-suppression algorithm and connection to the STAR DAQ system
- Basic designs needed to successfully integrate the three parts of the inner tracking in the construction phase.

Estimated R&D expenses in FY08:

- Pixel ~800 K Procurements, IST ~259K: Total
- Pixel ~900 K Engineering, IST ~473K: Total
- Pixel ~1000 K Contributed Engineering, IST XXXK: Total XXX
- Total R&D funds ~2,432K Project and XXX Contributed

Item	k$	Description	
BP procur	289	Beam Pipe Procurement	$288,750.00
CA fab	4	Detector insertion carriage fabrication	$3,850.00
CBL final	39	Ladder flex cable electronic substrate final fabrication	$38,500.00
CBL proto 1	19	Ladder flex cable electronic substrate prototype 1	$19,250.00
CBL proto 2	19	Ladder flex cable electronic substrate prototype 2	$19,250.00
CC fab	4	Electronic card cage procurement	$3,850.00
CONE procur	4	Support cone alterations for detector support	$3,850.00
COOL procur	8	Cooling system procurement	$7,700.00
DAQ Purch	19	DAQ hardware costs, PCs	$19,250.00
DC final	452	Detector chip final fabrication	$451,687.50
DC proto 1		Detector chip prototype 1	$0.00
DC proto 2	30	Detector chip prototype 2	$29,700.00
DC proto 3	119	Detector chip prototype 3	$118,800.00
DCtest station	19	Detector chip test station	$19,250.00
Insertion parts	4	Beam pipe and detector support insertion parts	$3,850.00
Installation procur	4	Addition installation parts	$3,850.00
KM final	6	Kinematic mount structures, fabrication	$5,775.00
KM proto	2	Kinematic mount structures, prototype	$1,925.00
L final	19	Ladder final fabrication/assembly	$19,250.00
L proto	10	Ladder prototype fabrication	$9,625.00
LS final	19	Ladder support final	$19,250.00
LS proto	10	Ladder support prototype	$9,625.00
M fab	2	Metrology fixture fabrication	$1,925.00
Monitor purch	4	Detector System monitoring computers	$3,850.00
Power	10	Detector power supplies and cabling	$9,625.00
RB final	386	Readout board final	$385,825.44
RB proto 1	3	Readout board prototype 1	$3,080.00
RB proto 2	3	Readout board prototype 2 (for in beam tests)	$3,080.00
slow control Purch	4	Slow control PCs	$3,850.00
Software Purch	30	Software, engineering tools	$30,030.00
Software training	6	Training for software engineering tools	$5,775.00
TT board	106	Trigger timing board	$105,875.00
U CBL final	39	Ultra ladder flex cable electronic substrate final fabrication	$38,500.00
U CBL final		Ultra ladder flex cable electronic substrate prototype 1	$0.00
U CBL proto 1	4	Ultra ladder flex cable electronic substrate prototype 2	$3,850.00
U CC design	2	Ultra card cage modification design	$1,925.00
U CC fab	2	Ultra card cage modification fab	$1,925.00
U COOL mod	2	Ulra cooling system modification	$1,925.00
U DAQ final	2	Ultra DAQ modification final	$1,925.00
U DAQ proto	2	Ultra DAQ modification prototype	$1,925.00
U DC Final	578	Ultra final detector chip production	$577,500.00
U DC Proto 2	43	Ultra detector chip prototype	$42,900.00
U DC test batch 1	2	Ultra detector chip testing parts	$1,925.00
U DT test	2	Ultra detector bench test parts	$1,925.00
U L final	19	Ultra ladder final parts	$19,250.00
U L proto	10	Ultra ladder prototype parts	
U LS final	2	Ultra final ladder support parts cost	
U LS proto	2	Ultra ladder support prototype parts cost	
U M measure	2	Ultra metrology parts	$1,925.00
U RB final	381	Ultra readout board final	$381,363.84

Table 21: Estimated cost of the HFT components. The total cost for the hardware components is $3.75M. This does not include engineering labor but it does include approximately $1M in manufacturing labor to be spent in the Mechanical shops at BNL and LBNL.

The estimated costs for the HFT components and hardware are shown in Table 21. The cost table includes only purchases and manufacturing expenses. The total hardware cost is 3.75 M$; this includes ~1M$ manufacturing labor but does not include the engineering labor or the contributed labor.

The electronic costs shown in Table 21 are primarily for procurements from outside vendors while mechanical fabrication costs are primarily for LBNL and BNL shops. All costs shown include overhead multipliers and contingency multipliers. The contingency multiplier for the detector silicon is 1.5, and for all other items the multiplier is 1.75. The cost for detector silicon and ladders reflect the plan to make 2 copies of the prototype detector (with MimoSTAR IV chips) and 4 copies of the final HFT detector (with UltraSTAR chips). The pricing of the readout electronics includes 100% spares.

The MS-Project files yield a rolled-up labor summary that consumes 13.5 FTEs of engineering labor over the life of the project, 7.5 FTEs of technical labor, and 3 FTEs of management and management support. The labor costed to the project is 3 M$, and the re-directed labor required is estimated to cost 1 M$ at BNL and 2 M$ at LBNL. The activities at BNL include, for example, technicians to install the support cones and beam pipe. The cost for labor at BNL and LBNL includes 75% contingency on wages.

The total estimated cost of the project is 7 M$ for R&D and construction activities. The re-directed labor adds an additional 3 M$ to the total project cost.

Studying the profile of funds for the HFT project is the next step. Currently, the profile of funds shown in the Micro-Soft-Project cost model is not a perfect match to the availability of funds. Refining this cost model is homework for the future and will appear in our Conceptual Design Report. Our goal is to match the profile of funds, and the completion date for the project, which was proposed by Brookhaven National Laboratory in the "Mid-Term Strategic Plan for the Relativistic Heavy Ion Collider"[156]. See Table 22.

	FY 2007	FY 2008	FY 2009	FY 2010	FY 2011	Total
R&D	.775M	1.3 M				2.075 M
PED		0.3 M				0.3 M
Construction			4 M	4.5 M	3 M	11.5 M
Total	.775M	1.6M	4 M	4.5 M	3 M	13.875M

FY 2007	FY 2008	FY 2009	FY 2010
1 M	0.8 M + 0.3 M	2.5 M	2.5 M
R&D	R&D + PED	Construction	Construction

Table 22: Proposed Funding Profile for the HFT that appears in the BNL Mid Term Plan[156]

8 Summary

Probing charm quark flow and thermal equilibration at RHIC may prove to be the final step towards the discovery of a Quark Gluon Plasma. Furthermore, measuring the energy lost by high transverse momentum heavy (c,b) quarks while traversing the medium will help disentangle between energy loss scenarios in cold nuclear matter and in partonic matter. The HFT is designed to tackle both tasks by precisely measuring open charm hadron yields, spectra and elliptic flow (v_2) as well as tagging the electrons produced by high transverse momentum beauty hadrons. The design requirements are fulfilled by having two thin ($\leq 0.28\%$ radiation length) layers of Active Pixel Sensors (APS) with a resolution of 10 μm at the front surface of the detector. APS technology is the only option that fits these requirements without compromising the efficiency or the readout speed. Indeed, an APS can be thinned down to 50 μm and their low power consumption allows us to use air-cooling. The mechanical support will be carefully designed so that the detector can be easily retracted. This feature allows the detector to be externally aligned, repaired and upgraded. By combining cutting edge sensor and readout technologies with a flexible and robust mechanical design, the HFT will provide the high precision data on heavy flavor hadrons that are crucial to understand the nature of the medium formed in Au + Au collisions at RHIC.

9 Appendix I The Silicon Strip Detector (SSD)

9.1 Introduction

The STAR Silicon Strip Detector[157] (SSD) constitutes the fourth layer of the HFT. It is installed between last layer of the IST and the TPC, the SSD will enhance the tracking capabilities of the STAR experiment by measuring accurately the two dimensional hit position and energy loss of charged particles. It aims specifically at improving the extrapolation of TPC tracks to the IST. As a result, the tracking efficiency is significantly improved. The SSD resides at a distance of 230 mm from the beam axis and covers a pseudorapidity range of $|\eta| < 1.2$. It has a total silicon surface of about 1 m^2.

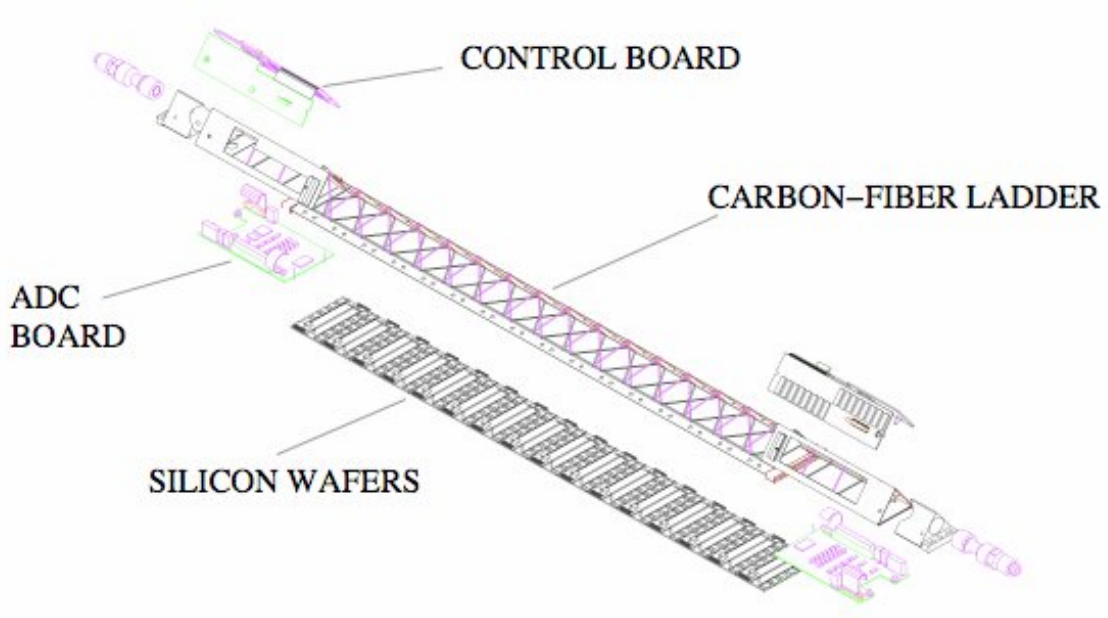

Figure 84. An SSD ladder showing separately its components.

The design of the SSD has two clamshells. Each clamshell supports 10 carbon fiber ladders. Each of these ladders, see Figure 84, supports 16 wafers using double-sided silicon strip technology (768 strips per side). These wafers are connected to the front-end electronics (6 ALICE 128C chips per side) by means of the Tape Automated Bonded (TAB) technology[158]. The ladders are tilted with respect to their long axis, allowing the

overlap of the detectors in the transverse plane for better hermiticity and alignment. A bus cable transports the analog signals along the ladder to a 10-bit ADC board, which is installed at each end. After digitization, the signals are sent to Readout Boards, which are linked to the DAQ system through Giga-link optics fibers.

The whole system is remotely controlled to monitor powers and temperature and also to calibrate and tune the front-end electronics. The cooling system uses airflow through the ladder, which is enclosed in a Mylar sheet. The total radiation length of each ladder is approximately 1%.

9.2 Current Readout

The current readout chain can be viewed in Figure 85. There, 10 ADC boards are daisy chained to one readout board. As each of the 20 ladders has two ADCs, then a total of four RDO boards can digitize the full detector.

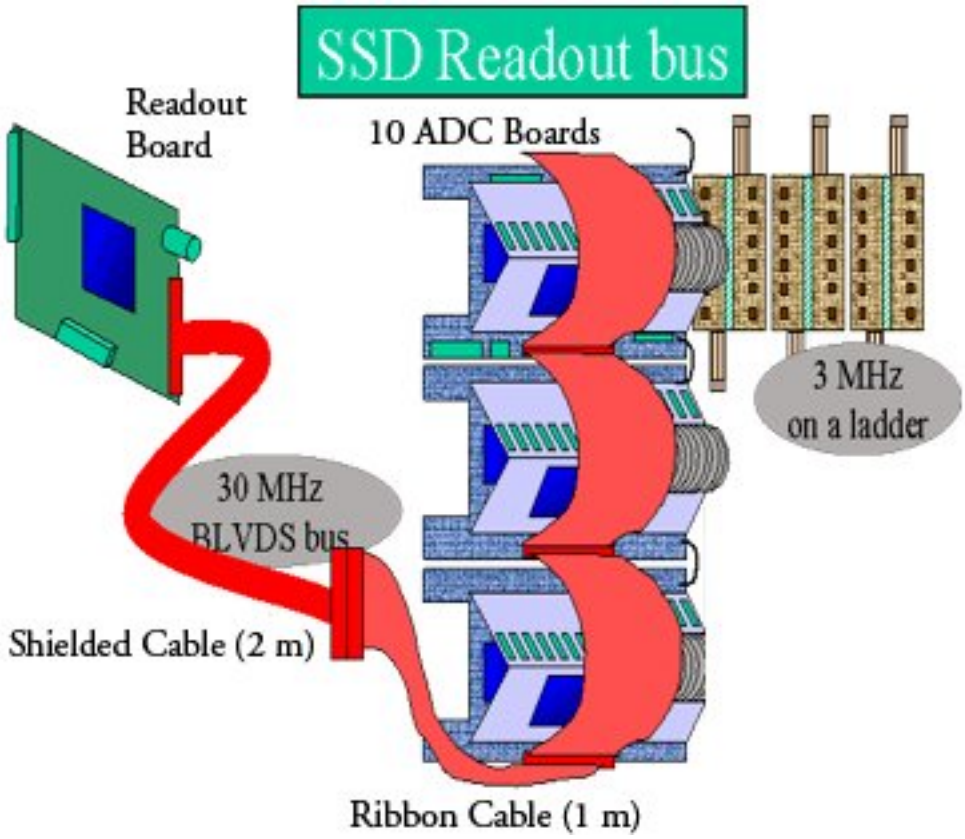

Figure 85. Module layout of the electronics.

The current FEE runs at 3 MHz. As there are 768 strips/wafer and 16 wafers/ADC Board, then it takes 4.1 ms to read out a ladder into the ADC Board. Each RDO, which runs at 30 MHz controls 10 ADC boards. Therefore, it takes a similar time, 4.1 ms, to read out each RDO. Due to a quick fix to match the TPC format, there is an extra 3 ms

needed to readout extra 0s. Nevertheless, that SSD readout time is less than the TPC, so no special effort has been made to eliminate this superfluous data. When needed, this extra data transfer can be eliminated.

9.3 Future Readout

The existing ADC, which is Analog Devices' model AD 9200,[159] can operate at 10 MSPS as its maximum speed is 20 MSPS. However, the fundamental limitation to increasing the readout speed to match DAQ1000 is the custom made Alice128 ASIC.[160] This device has a maximum speed of 10 MHZ. In principle, the ladder should work at 10 MHz. Nevertheless, this maximum speed must be demonstrated in full ladder test.

When the SSD operated at 10 MHz, it would readout out all of the strips in 1.23 ms. This speed is the fastest that a ladder's worth of data can be digitized using the current ladder. If this were done, then 3 ladder sides could be daisy chained together and connected to one RDO board. The total time to read out each board would then be a similar 1.23 ms. To implement this change, we would need to have a total of 14 RDO boards – 10 more than we are using now. We would also need a similar number of receivers in the DAQ Room.

9.4 Cooling

The SSD is cooled by room temperature air, which greatly reduces the material budget. Air-cooling has been shown that it can keep the SSD as a proper operating temperature. However, experience has shown that with the existing SVT, there is a tangle of cables. When the pole tip of the STAR magnet is closed, it is very difficult to maintain an adequate supply of air. Therefore, when the Pixel detector, IST and SSD are integrated in one structure, great care will be taken to provide adequate cooling that can be maintained when STAR is operating.

10 References

[1] F. Karsch,. *Nucl. Phys.* A699, 199c (2002).
[2] K.H. Ackermann et al., *Phys. Rev. Lett.* 86, 402 (2001).
[3] J. Adams et al., *Phys. Rev. Lett.* 91, 172302 (2003).
[4] C. Adler et al., *Phys. Rev. Lett.* 90, 082302 (2003).
[5] J. Adams et al. (STAR Collaboration), Nucl. Phys. A 757, 102 (2005).
[6] J. D. Bjorken, *FERMILAB-Pub-82/59-THY*.
[7] X. N. Wang, M. Gyulassy, I. Vitev, and B. Zhang, *nucl-th/0302077*.
[8] D. Schiff, R. Baier, and B. Zakharov, *Ann. Rev. Nucl. Part. Sci.*, 50, 37 (2000).
[9] J.J. Aubert et al., *Phys. Lett.* B123, 275 (1983).
[10] J. Ashman et al., *Phys. Lett.* B206, 364 (1988).
[11] J. Ashman et al., *Nucl. Phys.* B328, 1 (1989).
[12] B.L. Combridge, *Nucl. Phys.* B151, 429 (1979).
[13] B. Mueller, nucl-th/0404015.
[14] R. Vogt, hep-ph/0203151.
[15] K.J. Eskola, V.J. Kolhinen and R. Vogt, Nucl. Phys. A696, 729 (2001).
[16] P. Levai, B. Mueller, and X.N. Wang, *Phys. Rev.* C51, 3326 (1995) : P. Levai and R. Vogt, Phys. Rev. C56, 2707 (1997).).
[17] K. Adcox et al., *Phys. Rev. Lett.* 88, 192303 (2002).
[18] J. Adams et al. (STAR Collaboration), Phys. Rev. Lett. 94, 062301 (2005); nucl-ex/0407006.
[19] T. Sjostrand et al., Computer Physics Commun. 135, 238 (2001). PYTHIA 6.152 was used with the parameter settings: MSEL=1, CTEQ5M1. Bottom contribution was estimated to be 20-30% in p_T=2-3 GeV/c, 40-50% in 3-4 GeV/c to the total non-photonic electrons, and negligible at lower p_T.
[20] R. Vogt, Private Communication.
[21] S. Batsouli et al., Phys. Lett. B557, 26 (2003).
[22] X. Dong, "Open Charm Production at RHIC" QM2005, nucl-ex/0509038.
[23] J. Adams et al. (STAR Collaboration), Phys. Rev. Lett. 95, 122301 (2005).
[24] J. Adams et al. (STAR Collaboration)., Phys. Rev. Lett. 92, 052302 (2004).
[25] K. Schweda et al., J. Phys. G 30, S693 (2004).
[26] J. Castillo et al., J. Phys., G 30, S1207 (2004).
[27] J. Adams et al., (STAR Collaboration) Phys. Lett. B 616, 8 (2005)
[28] E. Shuryak, Phys. Lett. B78, 150 (1978).
[29] R. Rapp and J. Wambach, Adv. Nucl. Phys. 25, 1 (2000).
[30] R. Rapp, Phys. Rev. C 63**,** 054907 (2001); R. Rapp, hep-ph/0201101; R. Rapp and J. Wambach, hep-ph/9909229.
[31] U. Heinz and P.F. Kolb, Nucl. Phys. A702**,** 269c (2002).
[32] H. Sorge, Phys. Rev. Lett. 78, 239 (1997); H. Sorge, Phys. Rev. Lett. 8**2,** 2048 (1999).
[33] C. Adler et al*.,* (STAR Collaboration), Phys. Rev. Lett. 87, 262301 (2001).
[34] C. Adler et al., (STAR Collaboration), Phys. Rev. Lett. 89, 132301 (2002).
[35] P. Huovinen et al., Phys. Lett. B503, 58 (2001).
[36] M. Kaneta, J. Phys. G: Nucl. Part. Phys. 30, S1217 (2004).
[37] V. Greco, C.M. Ko, and R. Rapp, Phys. Lett. B595, 202 (2004)
[38] J. Stachel, Nucl. Phys. A654, 119c (1999).
[39] P. Braun-Munzinger, D. Magestro, K. Redlich, and J. Stachel, Phys. Lett. B518**,** 41 (2001).
[40] P. Braun-Munzinger, K. Redlich, and J. Stachel, nucl-th/0304013.
[41] E. Schnedermann, J. Sollfrank, and U. Heinz, Phys. Rev. C48**,** 2462 (1993).
[42] P. Braun-Munzinger and J. Stachel, Phys. Lett. B490**,** 196 (2000).
[43] P. Braun-Munzinger and J. Stachel, Nucl. Phys. A690**,** 119c (2001).

[44] A. Andronic, P. Braun-Munzinger, K. Redlich, and J. Stachel,. *Phys. Lett.* B571, 36 (2003).
[45] http://www-h1.desy.de/psfiles/confpap/EPS2003/H1prelim-02-076.ps
[46] http://www-zeus.desy.de/physics/phch/conf/eps03/564/paper.pdf
[47] T.Sjöstrand, *Comp. Phys. Commun.* 82, 74 (1994).
[48] A. Andronic et al., Phys. Lett. B571, 36 (2003).
[49] B.I. Abelev et al. (STAR Collaboration)., *Phys. Rev. Lett.* 98, 192301 (2007).
[50] M. Djordjevic, M. Gyulassy, and S. Wicks, Phys. Rev. Lett. 94, 112301(2005).
[51] Y.L. Dokshitzer and D.E. Kharzeev, Phys. Lett. B519, 199(2001).
[52] N. Armesto, A. Dainese, C.A. Salgado, U. Wiedemann, Phys. Rev. D71, 054027(2005).
[53] S. S. Adler et al. (STAR Collaboration),., *Phys. Rev. Lett.* 91, 072301 (2003).
[54] S. S. Adler et al. (STAR Collaboration)., *Phys. Rev. Lett.* 91, 241803 (2003).
[55] C. Adler et al. (STAR Collaboration)Phys. Rev.., *Lett.* 90, 082302 (2003).
[56] M. Gyulassy and M. Plümer, *Nucl. Phys.* A527, 641c (1991).
[57] Y. L. Dokshitzer and D. E. Kharzeev, *Phys. Lett.* B519, 199 (2001).
[58] H. Buesching, (Phenix Collaboration), QM05 proceedings.
[59] J. Dunlop, (STAR Collaboration), QM05 proceedings.
[60] X. Dong, charm production overview, QM05 proceedings.
[61] J. Adams, et al. (STAR Collaboration), Phys. Rev. Lett. 91 (2003) 072304.
[62] S.S. Adler et al. (Phenix Collaboration), Phys. Rev. Lett. 91, 072301 (2003).
[63] M. Djordjevic, M. Gyulassy, R. Vogt, and S. Wicks, nucl-th/0507019.
[64] H. van Hees, V. Greco, and R. Rapp, nucl-th/0508055.
[65] K. Abe, et al. (Belle Collaboration), Phys. Rev. Lett. 89, 142001(2002).
[66] S. Baek, P. Ko, J. Lee, and H.S. Song, J. Korean Phys. Soc. 33, 97 (1998).
[67] P.L.Cho and A.K. Leibovich, Phys. Rev. D54, 6690(1996).
[68] F. Yuan, D.F. Aiao, and K.T. Chao, Phys. Rev. D56, 321(1997).
[69] B.L. Ioffe and D.E. Kharzeev, Phys. Rev. D69, 014016(2004).
[70] M. Djordjevic, M. Gyulassy, R. Vogt, S. Wicks, nucl-th/0507019.
[71] D.E. Kharzeev and K. Tuchin, Nucl. Phys. A753, 316(2005).
[72] R. Rapp, Phys. Rev. C63, 054907 (2001).
[73] X. Dong, P. Sorensen, N. Xu, in preparation, Sept. 2005.
[74] A. Marín et al., J. Phys. G: Nucl. Part. Phys. 30, S709 (2004).
[75] D. Adamova et al. (CERES Collaboration), Phys. Rev. Lett. 91 (2003) 042301.
[76] R. Rapp, *Phys. Rev.* C63, 054907 (2001).
[77] R. Rapp, *Pramana* 60, 675 (2003).
[78] M. Cacciari, P. Nason, R. Vogt, hep-ph/0502203, PRL 95 122001 2005.
[79] See e.g. M Cacciari, hep-ph/0407187 and M.L. Mangano, hep-ph/0411020.
[80] B.A. Kniehl, G. Kramer, I. Schienbein, and H. Spiesberger, hep-ph/0508129, PRL 96 012001, 2006.
[81] http://www-hera-b.desy.de/general/talks/05/had05_charm_faccioli.pdf
[82] R. Vogt, private communication, 2007.
[83] M. Cacciari, M. Greco, and P. Nason hep-ph/9803400, JHEP 9805, 7, 1998.
[84] See e.g. Z. Xu, nucl-ex/0607015 and A.A.P. Suaide, nucl-ex/0702035.
[85] See e.g. STAR: B.Abelev, PRL 97, 252001, 2006.
[86] B. Lampe and E. Reya, hep-ph/9810270, Phys.Rept. 332, 1, 2000.
[87] M. Karliner and R.W. Robinett, Phys. Lett. B324, 209, 1994.

[88] I. Bojak and M. Stratmann, Phys. Rev. D67, 034010, 2003.

[89] X.-D. Ji, Phys. Lett. B284, 137, 1992; J. Soffer, M. Stratmann, W. Vogelsang, Phys. Rev. D65, 114024, 2002.

[90] http://rhicii-science.bnl.gov/spin/program/talks/sudoh-2.pdf

[91] K.H. Ackerman et al., Nucl. Instr. and Meth. A 499, 624 (2003).

[92] M. Anderson et al., Nucl. Instr. And Meth. A 499, 659 (2003).

[93] Billoir, Nucl. Instr. and Meth. **225**, 352, (1984).

[94] Technical report, http://www-rnc.lbl.gov/~wieman/HitDensityMeasuredLuminosity.htm
[95] Technical report, http://www-rnc.lbl.gov/~wieman/TrackDensityApr2004.htm
[96] Jim Thomas, Private Communication.
[97] Particle Data Group, Phys. Lett. B., Volume 592, Issues 1-4, 15 July 2004, p245.
[98] Karimäki, Nucl. Instrum. Methods A410, 284 (1998).
[99] ALICE Technical Design Report of the Inner Tracking System, CERN/LHCC 99-12, ALICE TDR 4 (1999).
[100] L. Ray and R.S. Longacre, nucl-ex/0008009 (2000).
[101] *GEANT -- Dectector Description and Simulation Tool*, The CERN computing center. CERN Program Library Long Writeup W5013, and Technical Report: http://www.star.bnl.gov/STAR/comp/simu/newsite/gstar/Manual/manual_index.html
[102] L. Arnold, J. Baudot, D. Bonnet, *et. al.*, "The STAR silicon strip detector (SSD)", Nucl. Instr.. and Meth., A 499, 652,(2003).
[103] http://www.star.bnl.gov/protected/spectra/macross/glauber/flow/FlowGlauberCalculations.htm
[104] W. Fischer, RHIC-II workshop, http://www.bnl.gov/panic05%5Fsatellite/
[105] Particle Data Book, Phys. Lett. **B59**2, 1 (2004).
[106] K. Abe, A. Arodzero, C. Baltay, J.E. Brau, M. Breidenbach, P.N. Burrows *et al.,* "Design and performance of the SLD vertex detector: a 307 Mpixel tracking system," *Nucl. Instr. and Meth.,* A 400, 287 (1997).
[107] J. Janesick, *Scientific Charge-Coupled Devices,* SPIE Press, Bellingham, WA, 2001.
[108] K.D. Stefanov, "CCd-based vertex detector for the future linear collider", Nucl. Instru. and Meth. A 549, 93 (2005).
[109] C.J.S. Damerell, "Charge coupled devices as particle tracking detectors," *Rev. Sci. Instr.,* vol. 69, pp. 1549-1573, 1998.
[110] J. Kemmer and G. Lutz, Nucl. Instr. and Meth. A 253, 365 (1987).
[111] G. Lutz, "DEPFET development at the MPI semiconductor laboratory", Nucl. Instr. and Meth. A 549, 103, (2005).
[112] E. R. Fossum, "CMOS Image Sensors: Electronic Camera-On-A-Chip", IEEE Trans. On Electron Devices, 44, 1689 (1977).
[113] http://ireswww.in2p3.fr/ires/recherche/capteurs/
[114] R. Turchetta et al., *Nucl. Instr.* and *Meth*. A 458, 677 (2001).
[115] M. Winter et al., *Proc. of the 8th ICATPP, Como Italy* (2003).*lear Science Symposium, Portland* O
[116] MIMOSA: Standing for Minimum Ionizing particle MOS Active pixel sensor.
[117] M. Devaux et al., *Nucl. Instr.* and *Meth*. A 512, 71 (2003).
[118] W. Dulinski et al., *Proc. IEEE Nuc*R. Trans. Nucl. Sci. (2003).
[119] http://www.lbnl.leog.org/thinned_mimosa_testing.htm
[120] Technical report, http://ireswww.in2p3.fr/ires/recherche/capteurs/index.html
[121] H. S. Matis, F. Bieser, S. Kleinfelder, G. Rai, F. Retiere, H.G. Ritter, K. Singh, S.E. Wurzel, H.H. Wieman, and E. Yamamoto, IEEE Trans. on Nucl. Sci. 50, 1020 (2003).
[122] S. Kleinfelder, H. Bichsel, F. Bieser, H. S. Matis, G. Rai, F. Retiere, H. Weiman, and E. Yamamoto, Proceedings of the SPIE, Hard X-Ray and Gamma Ray Detector Physics IV, July 2002, Vol. 4784, pp 208.
[123] H.S. Matis, F. Bieser, Y. Chen, R. Gareus, S. Kleinfelder, M. Oldenburg, F. Retiere, H.G. Ritter, H.H.

Wieman, S.E. Wurzel, E Yamamoto, Nucl. Instr. and Meth. A549, 130 (2005).

[124] S. Kleinfelder, S. Li, F. Bieser, R. Gareus, L. Greiner, J. King, J. Levesque, H.S. Matis*, M. Oldenbur, H.G. Ritter, F. Retiere, A. Rose, K. Schweda, A. Shabetai, E. Sichtermann, J.H. Thomas, H.H. Wieman, H. Bichsel, LBNL 59121. Submitted to the Proceedings of Pixel 2005, Bonn, Germany (2005).

[125] S. Kleinfelder, F. Bieser, Y. Chen, R. Gareus, H.S. Matis, M. Oldenburg, F. Retiere, H.G. Ritter, H.H. Wieman, E. Yamamoto, IEEE Trans. Nucl. Sci. 51, 2328 (2004).

[126] N.H. Xuong, A.-C. Milazzo, P. LeBlanc, F. Duttweiler, J. Bouwer, S. Peltier, M. Ellisman, P. Denes, F. Bieser, H.S. Matis, H. Wieman, S. Kleinfelder, In "Sensors and Camera Systems for Scientific, Industrial, and Digital Photography Applications V", SPIE 5301 242, (2004).

[127] Technical report, http://www-lepsi.in2p3.fr/~huch/MimoStar181203.pdf

[128] Technical report, http://www-rnc.lbl.gov/~wieman/RadiationLengthsProposal.htm

[129] http://www-rnc.lbl.gov/~wieman/radiationdoseinapsDulinskiValue.htm

[130] http://doc.cern.ch/yellowrep/2001/2001-006/p1.pdf

[131] http://www.lbnl.leog.org/writeup.htm

[132] Technical report, http://www-rnc.lbl.gov/~wieman/StiffnessLadder1.htm

[133] Technical report, http://www-rnc.lbl.gov/~wieman/StiffnessLadder1.htm

[134] TV Holography System at LBNL, courtesy of Eric Andersen and the ATLAS project.

[135] Technical report, http://www.lionprecision.com/modular/probes.html

[136] Technical report, http://www.lbnl.leog.org/writeup.htm

[137] Technical report, http://www.lbnl.leog.org/ir prelim writeup.htm

[138] Technical report, http://www.lbnl.leog.org/cable constraints.htm

[139] Technical report, http://www.lbnl.leog.org/crossing_lines_measurement_first_look.htm

[140] Please see http://direct.xilinx.com/bvdocs/publications/ds100.pdf

[141] MIMOSTAR-2 Manual, http://www.lbnl.leog.org/rdo/MimoStar2_1_1.pdf

[142] User Guide http://www.pg.infn.it/home/imbergam/microtronix_stratix/Getting%20Started%20Guide.pdf

[143] Schematic, http://www.lbnl.leog.org/rdo/mimostar2_mb_prelim_v4.pdf

[144] Schematic, http://www.lbnl.leog.org/rdo/mimostar2_cable_sept_test_final.pdf

[145] Schematic, http://www.lbnl.leog.org/pdf/hft-daughterboard.pdf

[146] Steve Peggs and Steve Tepikian, Private Communication.

[147] S. Tepikian,. Twiss functions and beam sizes of the RHIC intersection. *RHIC/AP25* (1994).

[148] Technical report, http://www-rnc.lbl.gov//~wieman/BeamPipeRadiusLimitsRHICAP25.htm

[149] Technical report, http://www-rnc.lbl.gov/~wieman/WolframFisherApertureNote.htm

[150] Technical report, http://www-rnc.lbl.gov/~wieman/BeamPipeVacuumShortAns.htm

[151] John O'Hanlon, *A User's Guide to Vacuum Technology*. John Wiley and Sons, second edition (1989).

[152] Seth Wieman, Private Communication.

[153] Technical report, http://www-rnc.lbl.gov/~wieman/TopThinPipeAnalysis.htm

[154] Sandro Bravar, Private Communication.

[155] Dan Weiss, Private Communication 30-Nov-2004.

[156] "Mid-Term Strategic Plan: 2006-2011 for the Relativistic Heavy Ion Collider at Brookhaven National Laboratory", Prepared by Brookhaven National Laboratory with the RHIC Scientific Community for the U.S. Department of Energy February 14, 2006.

[157] L. Arnold et al., *The STAR Silicon Strip Detector (SSD*), Nucl. Instrum. Meth. A 499, 652 (2003).

[158] S. Bouvier, *TAB: a packaging technology used for silicon strip detector to front end*

electronics interconnection, Proceedings of the workshop on electronics for LHC

experiments, Rome, Sept. 1998.

[159] http://www.analog.com/en/prod/0,,AD9200,00.html

[160] L. Hebrand et al., *Design and test of a CMOS low-power mixed-analog/digital ASIC forradiation detector readout front ends,* ASIC Conference 1998. Proceedings of the Eleventh Annual IEEE International, (1998), 89.